# Prehnite at the Atomic Scale: Al/Si Ordering, Hydrogen Environment, and High-Pressure Behavior

Theresa A. Detrie

Thesis submitted to the faculty of the Virginia Polytechnic Institute and State University in partial fulfillment of the requirements for the degree of

Master of Science
In
Geosciences

Dr. Nancy L. Ross, Chair
Dr. Ross J. Angel
Dr. Tiziana Boffa Ballaran

November 3, 2008
Blacksburg, VA

Keywords: prehnite, high-pressure, spectroscopy, X-ray diffraction, hydrogen, neutron diffraction

# Prehnite at the Atomic Scale: Al/Si Ordering, Hydrogen Environment, and High-Pressure Behavior

Theresa A. Detrie

## Abstract

The mineral prehnite, $Ca_2(Al,Fe,Mn)(AlSi_3O_{10})(OH)_2$, is a layered structure consisting of double-sheets of $(Al,Si)O_4$ and $SiO_4$ tetrahedra alternating with single sheets of $AlO_4(OH)_2$ octahedra. To understand the ordering in the structure and differences between various samples of prehnite, single-crystal X-ray diffraction data at ambient conditions were collected on four single crystals of prehnite from different localities. The positions of the H atoms have been determined for the first time, from a combination of X-ray and neutron diffraction data.

The equation of state and high-pressure behavior of prehnite have been investigated using single-crystal X-ray diffraction up to 9.75(3) GPa. A second-order Birch–Murnaghan equation of state fit to the isothermal P-V data to 8.7 GPa yields a bulk modulus, K = 109.29(18) GPa. Structural data collected at high pressures indicate that the structure compresses uniformly. Above 8.7 GPa there is additional softening of the volume and the *b*-axis related to polyhedral tilting. However, the average structure is maintained across the transition.

Ambient and high-pressure Raman and synchrotron infrared spectra were collected from 1 bar to 20 GPa. Raman spectra measured at ambient conditions of four prehnite crystals with different compositions confirmed that there are no structural changes with different compositions. High-pressure results showed the majority of modes shift to higher frequencies (in a smooth, linear fashion) with increasing pressure. The greatest change in the spectra is the softening of the modes in the OH-stretching region above 9 GPa, thought to be related to the polyhedral tilting around the H environment.

## Grant Information

This research was supported by National Science Foundation grants EAR-0229472 and EAR-0408460 to Dr. N.L. Ross and Dr. R.J. Angel. Travel grants to conferences were provided by the Geological Society of America, the American Crystallographic Association, and the Graduate Student Assembly Travel Fund Program. This research was partially supported by COMPRES, the Consortium for Materials Properties Research in Earth Sciences, under NSF Cooperative Agreement EAR 06-49658 and use of the National Synchrotron Light Source, Brookhaven National Laboratory, was supported by the U.S. Department of Energy, Office of Science, Office of Basic Energy Sciences, under Contract No. DE-AC02-98CH10886.

# Author Acknowledgements

This research would not have been accomplished without assistance from Dr. Nancy L. Ross and Dr. Ross J. Angel. Special thanks go out to them for their attention to all aspects of this project. Dr. Tiziana Boffa Ballaran is also thanked for her invaluable contributions to the interpretation of the spectroscopy research.

*Samples*

The author would like to thank the Virginia Tech Geosciences museum, the Natural History Museum (of London) and Dr. Pagano (U. of Milano) for providing prehnite research samples used in this study.

*Experiments*

Many thanks to the post-docs of the Crystallography lab, past and present, for their unyielding support, with special thanks to Dr. Jing Zhao, Dr. Elinor Spencer, Dr. Fabrizio Nestola, and Dr. Jens Engel. Added thanks go to Dr. Carla Slebodnick, Dr. G. Diego Gatta, Dr. Mark Welch (of the Natural History Museum, London), Dr. Ron Smith (POLARIS beamline scientist at ISIS, Rutherford Appleton Lab, U.K.), Dr. Zhenxian Liu (U2A beamline scientist at NSLS, Brookhaven National Lab), Mr. Charles Farley & Dr. Robert Bodnar (for use of the Virginia Tech Raman lab), and Mr. Clayton Loehn & Dr. Robert Tracy (for use of the Virginia Tech SEM/Microprobe lab and completion of microprobe analyses).

*Support*

Thanks to the VTX group, fellow graduate students, and my family for their willingness to listen and support me through this degree.

# Table of Contents

# List of Figures

# List of Tables

# Chapter 1: Introduction

## 1.1 Opening remarks

For interpretation of broad-scale geologic processes, the properties of rock-forming minerals play an important role in bulk rock properties. These properties, including structures, mineral stability, relationships between mineral phases, and thermodynamics, contribute to a better understanding of the Earth's interior. Metamorphic minerals tell a history of maximum previous P and T conditions, locked within their structures. The mineral prehnite, best known for being a member of the prehnite-pumpellyite metamorphic facies, tells a story of pressures and temperatures between 2-6 kbars and 200-350 ºC, respectively. The prehnite-pumpellyite facies is bounded at lower P/T conditions by the stability of zeolites, and upper conditions by the greenschist/blueschist facies (Figure 1.1). Prehnite stability is bounded at higher temperatures and pressures by the reaction 5 prehnite ↔ 2 grossular + 2 zoisite + 3 quartz + 4 $H_2O$ or the metastable boundary prehnite ↔ anorthite + wollastonite + $H_2O$. The lower P-T limit of prehnite stability is less-well defined, consisting of a breakdown of the zeolites laumontite and wairakite to transform into prehnite, by the reactions 2 wairakite + *n*H2O ↔ prehnite + Ca-montmorillonite + quartz (where *n* is dependent on the montmorillonite) and 2 laumontite ↔ prehnite + kaolinite + 3 quartz + 5 $H_2O$ (Liou, 1971). Prehnite is commonly found as a mineral phase in the shallow depths of subduction systems (Figure 1.2), where dehydration reactions occur and hydrogen is incorporated into the structures of minerals such as prehnite, either as hydroxyl ($OH^-$) or as $H_2O$. Incorporation of hydrogen plays an important role in the behavior of minerals at depth, both in compression and mineral stability.

The purpose of the thesis is to provide a detailed experimental look at the crystal structure, high-pressure properties, and vibrational spectroscopy of prehnite. In the following three chapters, the experiments are described in three related concepts: crystal chemistry, equation of state and structure at high pressure, and vibrational spectroscopy, including far-infrared, mid-infrared, and Raman spectroscopy. This thesis presents new, original data for prehnite, as neither high-pressure studies (X-ray diffraction or Raman/infrared spectroscopy) nor neutron diffraction studies have been undertaken previously to examine the properties of prehnite.

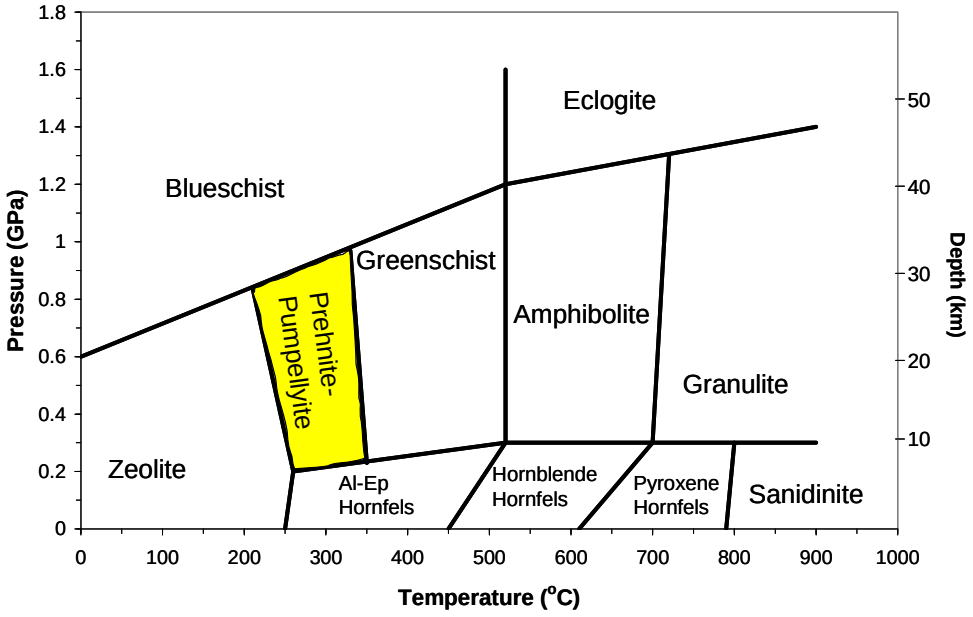


Figure 1.1: Pressure-temperature diagram showing the metamorphic facies. Please note that the boundaries are gradational and approximate. Highlighted in yellow is the prehnite-pumpellyite stability field.

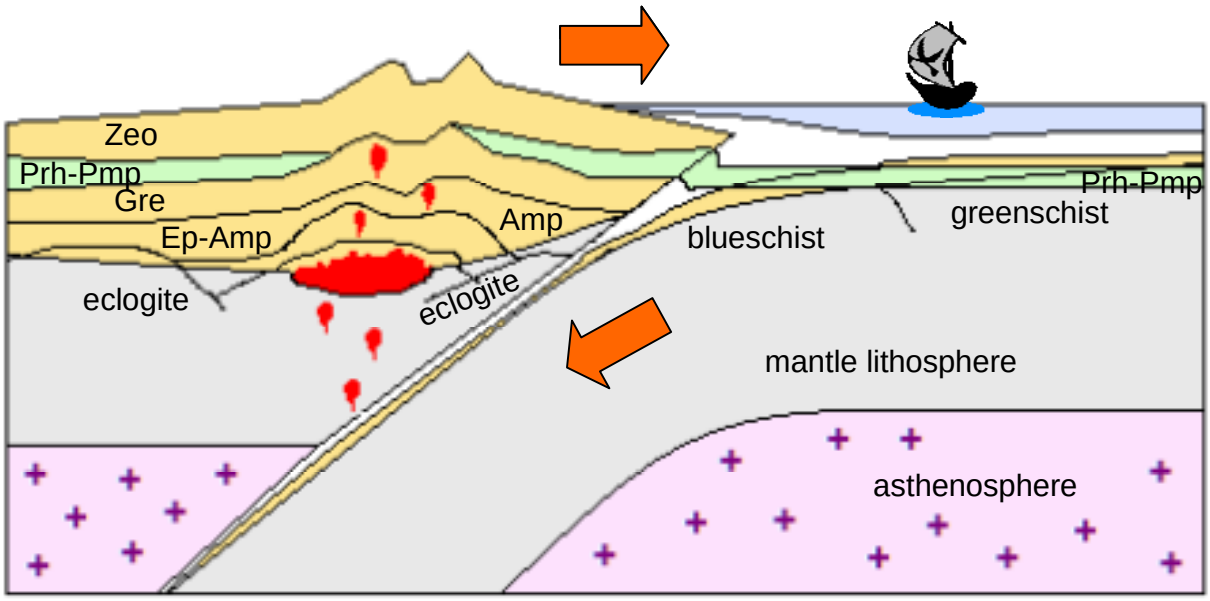


Figure 1.2: Diagram showing the collision of an oceanic plate with a continental plate and subsequent subduction of the oceanic plate. Prehnite-pumpellyite zone is shaded in green. (Figure not to scale.) Abbreviations are: Zeo: zeolites, Prh-Pmp: prehnite-pumpellyite, Gre: greenschist, Ep-Amp: epidote-amphibolite, and Amp: amphibolite.

In Chapter 2, the crystal chemistry of prehnite is discussed, as determined by single-crystal X-ray diffraction experiments of crystals from multiple localities as well as a powder neutron diffraction experiment to assist in locating the hydrogen atoms in the structure. As a result of a detailed analysis from X-ray and neutron diffraction experiments, it is possible to determine

whether compositional changes result in structural changes. This will contribute to a better understanding of whether compositional changes affect the state of ordering of the Al/Si on the tetrahedral sites in prehnite and the location of the hydrogen atom in the structure. In addition, the full structural analysis will determine whether there are contributions to the configurational entropy arising from order/disorder of Al/Si and/or the hydrogen atoms in the structure.

Results from high-pressure single-crystal X-ray diffraction experiments are presented in Chapter 3. The goal of the high pressure study is to determine the equation of state of prehnite and to examine the structure of prehnite *in situ* at high pressure. The equation of state of prehnite has never been determined and thermodynamic databases rely on an estimated value for the bulk modulus of prehnite. The structure was measured at various pressures to clarify the compression mechanisms operative in prehnite by tracking changes in bond lengths and bond angles. The chapter concludes with a comparison of the bulk modulus of prehnite with other minerals that have topologically and chemically similar structures.

Chapter 4 presents newly measured far-infrared, mid-infrared and Raman spectra of prehnite collected at ambient conditions and the first vibrational spectra collected at high pressure to 20.4 GPa. Vibrational spectra provide information about inter-atomic bonding in the structure and therefore provide a powerful method to determine structural changes of prehnite at a local scale (e.g. nanometer length scale) and the effect of changes in composition and pressure. Factor group analysis is discussed and employed as a way to estimate the number and symmetry of the vibrational modes that may be observed in the spectra. Far-infrared, mid-infrared, and Raman spectroscopy undertaken at ambient and high-pressures are described in detail and compared with the results from the high-pressure X-ray diffraction experiments.

The major conclusions from this comprehensive study of prehnite are summarized in Chapter 5.

## 1.2 References

Liou, J.G. (1971): Synthesis and stability relations of prehnite, $Ca_2Al_2Si_3O_{10}(OH)_2$. *American Mineralogist,* 56, 507-531.

# Chapter 2: Crystal chemistry and location of hydrogen atoms in prehnite

## 2.1 Abstract

The mineral prehnite, $Ca_2(Al,Fe,Mn)(AlSi_3O_{10})(OH)_2$**,** is a layered structure described as a mixed tetrahedral-octahedral network consisting of double-sheets of $(Al,Si)O_4$ and $SiO_4$ tetrahedra alternating with single sheets of $AlO_4(OH)_2$ octahedra. The average symmetry is *Pncm*. Different patterns of Al/Si ordering on the tetrahedral T2 site give rise to different space group symmetries *P*2*cm* and *P*2/*n*. To understand the ordering in the structure and the ordering differences between various samples of prehnite, single-crystal X-ray diffraction data at room conditions were collected on four single crystals of prehnite from different localities. Refinements were successful using the average structure, *Pncm*. The positions of the H atom in the structure of prehnite have been determined for the first time, from a combination of X-ray and neutron diffraction data. Because both the H and Al/Si appear to be fully ordered, there will be no configuration contribution to the entropy of prehnite.

## 2.2 Introduction

Prehnite, with an ideal formula $Ca_2(Al,Fe,Mn)(AlSi_3O_{10})(OH)_2$, contains corner-sharing tetrahedra and octahedra, with hydroxyl groups sitting on the apices of the octahedra. The tetrahedra and octahedra form layers as viewed down the *b* axis, consisting of one octahedral layer and three tetrahedral layers, repeating every 9.3 Å (Figure 2.1). The prehnite structure shows similarities with framework silicates in that four tetrahedra (made up of two unique sites) are oriented in a corner-sharing corkscrew pattern, elongate parallel to the [010]. The two unique tetrahedral sites, T1 and T2, contain silicon and aluminum/silicon respectively (Figure 2.1). The octahedron, M1, contains aluminum with any iron in the structure also being accounted for on this site (Artioli *et al.*, 1995; Akasaka *et al.*, 2003). There is a channel in the structure, parallel to the [100], where a calcium atom resides in 7-fold coordination with neighboring oxygen atoms of the polyhedra (Figure 2.2).

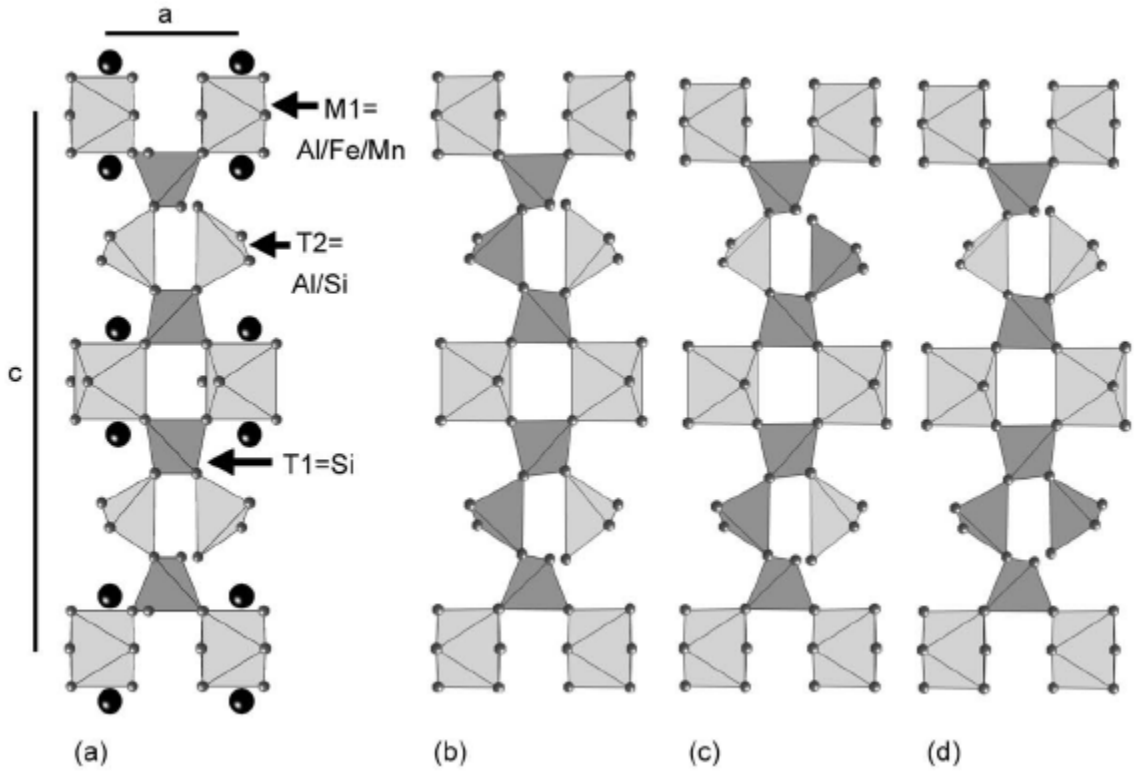


Figure 2.1: The ordering schemes of the prehnite structure, as viewed 6 º from [010]. The light gray polyhedra represent Al, whereas the dark gray polyhedra represent Si (unless noted otherwise). (a) *Pncm* symmetry. The large black spheres represent Ca sites, whereas the small gray spheres represent oxygen sites. (b) *P2cm* symmetry. (c) $P22_12$ symmetry.

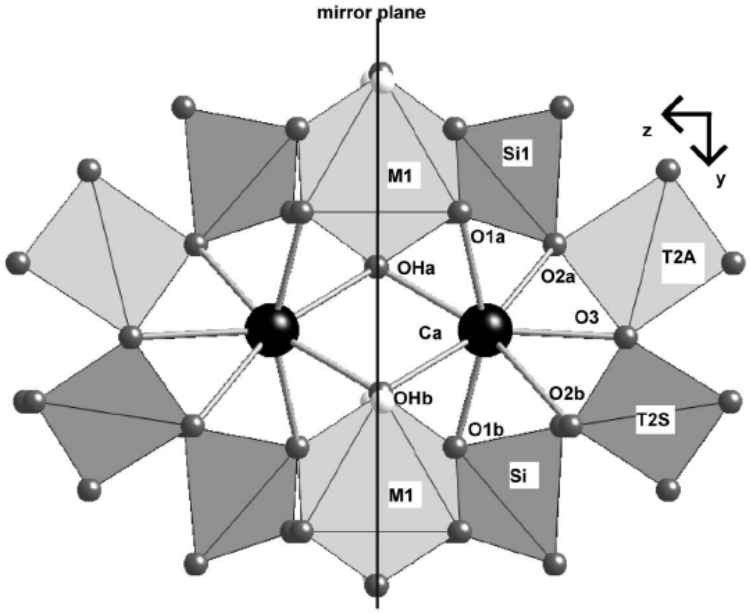


Figure 2.2: The Ca-channel in prehnite as viewed from a direction 2 º from [100] with *P2cm* atom labeling. The large black spheres represent Ca sites, the small gray spheres represent oxygen sites, and the small white spheres represent hydrogen sites with OH-H vectors perpendicular to the viewing plane. In looking at the labeling and comparing it to Pncm labeling, the O1a & O1b become one site, the O2a & O2b become one site, the OHa & OHb become one site (OH), and T2A and T2S become one site (Al/Si disordered T2 site).

The average structure of prehnite has *Pncm* symmetry, with one tetrahedral site solely silicon while the other, T2, contains disordered aluminum and silicon. Papike and Zoltai (1967) showed that there are three possible ordering schemes of the T2 site (Figure 2.1). The first is *P2cm*, where there is a distinct aluminum-rich T2 site on the same side, when comparing the two tetrahedral corkscrews within the unit cell. In *P2/n*, the aluminum-rich T2 tetrahedron is on opposite sides of the two tetrahedral corkscrews. The last possible scheme, $P22_12$, can be described as having two aluminum-rich T2 tetrahedra in the top corkscrew, and two silicon-rich T2 tetrahedra in the bottom corkscrew. In agreement with the conclusion of Papike and Zoltai (1967), this is unlikely due to Al-O-Al linkages that are unstable in silicates (Lowenstein, 1954). Successful refinements in *P2cm* symmetry were performed by Balić-Žunić *et al.* (1990), Baur *et al*. (1990), Aumento (1968), Preisinger (1965), and Nuffield (1943). Space group *P2cm* is in agreement with the pyroelectric studies performed by Traube (1894), suggesting that *a*-axis of prehnite is a polar axis. The presence of twin lamellae or domains produced during growth with symmetry *P2/n* was considered a valid possibility by Akasaka *et al.* (2003) and Akizuki (1987).

The location of the hydrogen in prehnite has not previously been reported, although it can be inferred that it is attached to an otherwise under-bonded oxygen atom that forms the apex of the octahedron, and which is not bonded to either of the tetrahedral sites. This site has consistently been labeled "OH" (e.g. Papike & Zoltai 1967; Balić-Žunić *et al.*, 1990) in previous structural studies. A definitive location of the hydrogen atoms will contribute to the understanding of the thermodynamic properties of prehnite, including the potential for hydrogen disorder and the existence and strength of H-bonding, all of which would contribute to the entropy of prehnite. Experimentally, locating hydrogen using X-rays is not impossible in the presence of heavier atoms, but not as practical as other methods, such as neutron diffraction. The single electron of hydrogen is a weak scatterer of X-rays and is not as visible in lower-quality datasets, whereas the proton is a much stronger scatterer of neutrons. Previous neutron diffraction studies have had success in locating hydrogen atoms in mineral structures, including leucophoenicite (Welch *et al.*, 2002) and chondrodite (Berry & James, 2002). These were performed on undeuterated samples, to eliminate the possibility of incomplete H/D exchange and contrast-matched ratios, resulting in hydrogen invisibility.

The purpose of this study was thus twofold; to determine whether there are significant differences in the structures of prehnite from different localities, in particular in the state of Al,Si order, and to locate the H atom in the structure.

### 2.3 Experimental Methods

Prehnite samples from four different localities were used in this study (Table 2.1). Electron microprobe analyses were performed on grain mounts with a Cameca SX50, using CaO, $SiO_2$, $Al_2O_3$, $Fe_2O_3$, and $Mn_2O_3$ as standards. Microprobe analyses were done on two samples using a wider range of elements (including Na, K, Mg, F, Ba, and Sr), however results revealed that these elements individually contributed to less than 0.05 weight percent and therefore were not used in the remaining analyses. Chemical compositions were calculated assuming that all Fe and Mn were in the +3 valence state, and hydrogen was calculated by difference.

Single crystals of each of the four samples were selected for intensity data collection on the basis of diffraction quality. Rejected crystals typically exhibited split rows of diffraction spots due to misalignment of {001} plates as described by Balić-Žunić *et al.* (1990). Intensity datasets were collected from selected crystals at room conditions with Oxford Diffraction Xcalibur or Gemini diffractometers equipped with CCD detectors, operated at 50 kV, 40 mA, with MoKα radiation and a graphite monochromator. Full spheres of diffraction data were collected out to $2\theta=60^{o}$. Data were absorption-corrected within the CrysAlis program (Oxford Diffraction, 2006). Structure refinements (using neutral atom scattering factors) were performed in Shelxl-97 (Sheldrick, 2008), driven by WinGX (Farrugia, 1999) using a starting model based on the structure refined in space group *Pncm* by Papike and Zoltai (1967). Unit cell parameters were measured using the CCD detector. All sites were assumed to be fully occupied. The Al/Si occupancies of the tetrahedral sites were assigned on the basis of bond lengths. The Fe or Mn were assigned (Artioli *et al.*, 1995; Akasaka *et al.*, 2003) to the octahedral sites, M1, and the Al/(Fe+Mn) ratio on these sites was refined. All non-H atoms were refined anisotropically. The hydrogen atoms were located in the difference-Fourier map and subsequently refined, with the O-H distance constrained to 0.98 +/- 0.03 Å. Further details of the data collections and subsequent refinements are given in Table 2.1. The coordinates of the atoms, bond lengths, and

bond angles are listed in Tables 2.2, 2.3, and 2.4 respectively for *Pncm*. The refinement results in *P2cm* symmetry can be found in Table 2.5, and the coordinates, bond lengths, and bond angles can be found in Tables 2.6, 2.7, and 2.8.

Neutron diffraction data were collected at room temperature from a powdered sample of prehnite tad4, loaded in a vanadium can and mounted on the POLARIS neutron time-of-flight diffractometer at ISIS, Rutherford-Appleton Laboratory, U.K. The diffraction pattern was measured using two detector banks-the 90˚ detector bank ($\Delta d/d = 0.007$) and the 145˚ detector bank ($\Delta d/d = 0.005$). Refinements were performed using data from both detector banks simultaneously. The refined X-ray structure in *Pncm* was used as a starting model. The site occupancies were assigned to be the same as the X-ray refinement, and all of the temperature factors were set as isotropic (including hydrogen). Also included in the refinement was a preferred orientation parameter to allow for the dominant {001} cleavage. The overall final Rwp was 0.0197 for 8216 data points. $R_{Bragg}$ was 0.0461 calculated for 4652 reflections in the 145˚ detector bank, and RBragg was 0.0340 calculated for 1901 reflections in the 90˚ detector bank. The total weighted Chi squared was 19.1 for 72 variables, 46 experimental parameters and 26 structural parameters.

## 2.4 Results and Discussion

Results of the microprobe show that only two of the four samples contain iron on the octahedral site (7%, tad1; 26% tad4). A third sample, tad5 shows trace amounts of manganese- 2% (+/- 1%). The last sample, tad2, did not show trace amounts of either iron or manganese within error. The sample with the most iron, tad4, also showed the most color- a seafoam green, when comparing the color of similar crystal sizes of the various samples.

Table 2.1: Details of prehnite structure refinements in *Pncm*.

| tad1x2 | tad2x1 | tad5x1 | tad4x1 | tad4 N |
|---|---|---|---|---|
| Tyrol | Norway | South Africa | Mali | Mali |
| Nat Hist Museum | Nat Hist Museum | Dr. Pagano collection | purchased | purchased |
| London | London | | | |
| bm 1916.641 | OH-bm 34555 | #8789 | | |
| Ca 2.06 | Ca 2.05 | Ca 2.07 | Ca 1.92 | Ca 1.92 |
| (Al 0.93, Fe 0.07) | (Al 0.997, Mn 0.003) | (Al 0.98, Mn 0.02) | (Al 0.74, Fe 0.26) | (Al 0.74, Fe 0.26) |
| (Al Si 3.09 O 10) | (Al Si 3.09 O 10) | (Al Si 3.09 O 10) | (Al Si 2.95 O 10) | (Al Si 2.95 O 10) |
| (OH) 2 | (OH) 2 | (OH) 2 | (OH) 2 | (OH) 2 |
| | | | | |
| 412.895 | 412.55 | 412.86 | 419.07 | |
| 293(2) K | 293(2) K | 293(2) K | 293(2) K | 293(2) K |
| X-ray | X-ray | X-ray | X-ray | neutrons ToF |
| 0.71073 Å | 0.71073 Å | 0.71073 Å | 0.71073 Å | |
| Orthorhombic | Orthorhombic | Orthorhombic | Orthorhombic | Orthorhombic |
| P n c m | P n c m | P n c m | P n c m | P n c m |
| a = 4.6291(5) Å | a = 4.6254(8) Å | a = 4.6284(3) Å | a = 4.6857(6) Å | a = 4.64542(17) Å |
| b = 5.4876(6) Å | b = 5.4798(10) Å | b = 5.4903(4) Å | b = 5.5344(7) Å | b = 5.48972(18) Å |
| c = 18.5034(15) Å | c = 18.472(4) Å | c = 18.5131(13) Å | c = 18.673(2) Å | c =18.5494(8) Å |
| 470.03(7) | 468.19(17) | 470.44(8) | 484.23(11) | |
| 2 | 2 | 2 | 2 | 2 |
| 2.917 | 2.926 | 2.915 | 2.874 | |
| 1.878 | 1.869 | 1.872 | 2.112 | |
| 412 | 412 | 412 | 418 | |
| 0.15 x 0.11 x 0.02 | 0.15 x 0.09 x 0.02 | 0.35 x 0.11 x 0.09 | 0.19 x 0.19 x 0.02 | powder |
| 4.40 to 30.02°. | 3.88 to 30.21°. | 3.87 to 30.02°. | 3.84 to 29.91°. | |
| -6<=h<=6, -7<=k<=7, -26<=l<=26 | -6<=h<=6, -7<=k<=7, -26<=l<=26 | -6<=h<=6, -7<=k<=7, -26<=l<=26 | -6<=h<=6, -7<=k<=7, -26<=l<=26 | |
| 8621 | 8160 | 7568 | 8656 | |
| 149 | 52 | 7 | 422 | |
| 3 | 14 | 25 | 188 | |
| 710 [R(int) = 0.0563] | 721 [R(int) = 0.0668] | 712 [R(int) = 0.0274] | 730 [R(int) = 0.0735] | |
| 99.70% | 99.90% | 99.90% | 99.50% | |
| Gaussian | Gaussian | Gaussian | Gaussian | |
| 0.94812 and 0.78365 | 0.96947 and 0.77504 | 0.856 and 0.563 | 0.94751 and 0.71170 | |
| Full-matrix least-squares on $F^2$ | Full-matrix least-squares on $F^2$ | Full-matrix least-squares on $F^2$ | Full-matrix least-squares on $F^2$ | Rietveld |
| 710 / 1 / 53 | 721 / 1 / 53 | 712 / 1 / 53 | 730 / 1 / 53 | 8216 (powder) /1/ 72 |
| 1.354 | 1.448 | 1.41 | 1.269 | 19.07 |
| $R_1$ = 0.0638, $wR_2$ = 0.1286 | $R_1$ = 0.0767, $wR_2$ = 0.1384 | $R_1$ = 0.0512, $wR_2$ = 0.1268 | $R_1$ = 0.0443, $wR_2$ = 0.0913 | |
| $R_1$ = 0.0640, $wR_2$ = 0.1287 | $R_1$ = 0.0848, $wR_2$ = 0.1408 | $R_1$ = 0.0512, $wR_2$ = 0.1268 | $R_1$ = 0.0528, $wR_2$ = 0.0942 | $R_1$ = 0.0224, $wR_2$ = 0.0197 |
| 0.948 and -0.746 e.Å$^{-3}$ | 0.997 and -1.000 e.Å$^{-3}$ | 1.174 and -1.882 e.Å$^{-3}$ | 0.688 and -0.724 e.Å$^{-3}$ | |

Table 2.2: Positional and displacement parameters for prehnite in *Pncm*.

| sample ID | | tad1x2 | tad2x1 | tad5x1 | tad4x1 | tad4 N |
|---|---|---|---|---|---|---|
| locality | | Tyrol | Norway | S. Africa | Mali | Mali |
| M1 | $U_{iso}$ | 0.010(1) | 0.014(1) | 0.008(1) | 0.010(1) | 0.0047(4) |
| | $U_{11}$ | 0.007(1) | 0.010(2) | 0.005(1) | 0.007(1) | |
| | $U_{22}$ | 0.016(2) | 0.016(2) | 0.012(1) | 0.012(1) | |
| | $U_{33}$ | 0.008(1) | 0.016(2) | 0.006(1) | 0.012(1) | |
| | $U_{12}$ | 0.001(1) | 0.000(2) | 0.001(1) | 0.000(1) | |
| | $U_{13}$ | 0 | 0 | 0 | 0 | |
| | $U_{23}$ | 0 | 0 | 0 | 0 | |
| T2 | *x* | 0.1913(4) | 0.1916(5) | 0.1914(4) | 0.1901(3) | 0.1904(4) |
| | $U_{iso}$ | 0.009(1) | 0.012(1) | 0.005(1) | 0.010(1) | 0.0018(4) |
| | $U_{11}$ | 0.011(1) | 0.012(1) | 0.005(1) | 0.008(1) | |
| | $U_{22}$ | 0.008(1) | 0.008(1) | 0.004(1) | 0.009(1) | |
| | $U_{33}$ | 0.008(1) | 0.016(1) | 0.005(1) | 0.012(1) | |
| | $U_{12}$ | 0 | 0 | 0 | 0 | |
| | $U_{13}$ | 0 | 0 | 0 | 0 | |
| | $U_{23}$ | 0.000(1) | 0.000(1) | 0.000(1) | -0.001(1) | |
| Si1 | *z* | 0.1196(1) | 0.1195(1) | 0.1196(1) | 0.1203(1) | 0.12036(12) |
| | $U_{iso}$ | 0.009(1) | 0.013(1) | 0.006(1) | 0.011(1) | 0.0016(3) |
| | $U_{11}$ | 0.009(1) | 0.011(1) | 0.005(1) | 0.008(1) | |
| | $U_{22}$ | 0.010(1) | 0.012(1) | 0.008(1) | 0.011(1) | |
| | $U_{33}$ | 0.007(1) | 0.015(1) | 0.005(1) | 0.013(1) | |
| | $U_{12}$ | -0.001(1) | -0.001(1) | -0.001(1) | 0.000(1) | |
| | $U_{13}$ | 0 | 0 | 0 | 0 | |
| | $U_{23}$ | 0 | 0 | 0 | 0 | |
| Ca1 | *z* | 0.0992(1) | 0.0993(1) | 0.0993(1) | 0.0995(1) | 0.10004(14) |
| | $U_{iso}$ | 0.013(1) | 0.017(1) | 0.010(1) | 0.015(1) | 0.0114(5) |
| | $U_{11}$ | 0.015(1) | 0.018(1) | 0.012(1) | 0.017(1) | |
| | $U_{22}$ | 0.016(1) | 0.016(1) | 0.012(1) | 0.014(1) | |
| | $U_{33}$ | 0.009(1) | 0.016(1) | 0.006(1) | 0.013(1) | |
| | $U_{12}$ | 0.002(1) | 0.001(1) | 0.001(1) | 0.001(1) | |
| | $U_{13}$ | 0 | 0 | 0 | 0 | |
| | $U_{23}$ | 0 | 0 | 0 | 0 | |

| sample ID | | tad1x2 | tad2x1 | tad5x1 | tad4x1 | tad4 N |
|---|---|---|---|---|---|---|
| locality | | Tyrol | Norway | S. Africa | Mali | Mali |
| OH | *x* | -0.2048(10) | -0.2051(12) | -0.2056(10) | -0.2076(7) | -0.2068(4) |
| | *y* | 0.3021(9) | 0.3020(11) | 0.3021(9) | 0.3053(6) | 0.3077(4) |
| | $U_{iso}$ | 0.011(1) | 0.014(1) | 0.007(1) | 0.014(1) | 0.0087(4) |
| | $U_{11}$ | 0.006(2) | 0.007(2) | 0.004(2) | 0.009(1) | |
| | $U_{22}$ | 0.015(2) | 0.014(3) | 0.010(2) | 0.015(2) | |
| | $U_{33}$ | 0.011(2) | 0.020(3) | 0.008(2) | 0.017(2) | |
| | $U_{12}$ | 0.000(2) | 0.002(2) | 0.001(2) | 0.000(1) | |
| | $U_{13}$ | 0 | 0 | 0 | 0 | |
| | $U_{23}$ | 0 | 0 | 0 | 0 | |
| O1 | *x* | -0.7504(8) | -0.7512(8) | -0.7502(7) | -0.7487(5) | -0.7489(3) |
| | *y* | 0.1322(7) | 0.1315(8) | 0.1319(6) | 0.1331(4) | 0.13236(17) |
| | *z* | 0.0735(2) | 0.0734(2) | 0.0734(2) | 0.0742(1) | 0.07436(8) |
| | $U_{iso}$ | 0.013(1) | 0.015(1) | 0.009(1) | 0.014(1) | 0.0065(2) |
| | $U_{11}$ | 0.012(2) | 0.010(2) | 0.006(1) | 0.008(1) | |
| | $U_{22}$ | 0.018(2) | 0.016(2) | 0.013(2) | 0.016(1) | |
| | $U_{33}$ | 0.010(2) | 0.018(2) | 0.009(1) | 0.018(1) | |
| | $U_{12}$ | 0.001(1) | 0.001(2) | 0.000(1) | 0.001(1) | |
| | $U_{13}$ | -0.002(1) | -0.002(2) | -0.002(1) | -0.002(1) | |
| | $U_{23}$ | 0.000(1) | 0.000(2) | -0.001(1) | 0.000(1) | |
| O2 | *x* | -0.3686(8) | -0.3688(9) | -0.3683(8) | -0.3666(5) | -0.3668(3) |
| | *y* | 0.2143(7) | 0.2142(7) | 0.2143(6) | 0.2138(5) | 0.2147(3) |
| | *z* | 0.1717(2) | 0.1716(2) | 0.1716(2) | 0.1718(1) | 0.17203(8) |
| | $U_{iso}$ | 0.015(1) | 0.018(1) | 0.012(1) | 0.018(1) | 0.0114(3) |
| | $U_{11}$ | 0.016(2) | 0.017(2) | 0.012(2) | 0.017(1) | |
| | $U_{22}$ | 0.012(2) | 0.012(2) | 0.008(2) | 0.013(1) | |
| | $U_{33}$ | 0.017(2) | 0.026(2) | 0.016(2) | 0.025(1) | |
| | $U_{12}$ | 0.001(1) | 0.002(2) | 0.001(1) | 0.002(1) | |
| | $U_{13}$ | -0.008(1) | -0.009(2) | -0.009(1) | -0.010(1) | |
| | $U_{23}$ | -0.005(1) | -0.005(2) | -0.005(1) | -0.006(1) | |
| O3 | *z* | 0.2304(3) | 0.2305(3) | 0.2303(3) | 0.2303(2) | 0.23069(12) |
| | $U_{iso}$ | 0.016(1) | 0.019(1) | 0.014(1) | 0.018(1) | 0.0126(4) |
| | $U_{11}$ | 0.018(2) | 0.022(3) | 0.017(2) | 0.020(2) | |
| | $U_{22}$ | 0.019(3) | 0.017(3) | 0.015(2) | 0.019(2) | |
| | $U_{33}$ | 0.012(2) | 0.019(3) | 0.009(2) | 0.015(2) | |
| | $U_{12}$ | -0.004(2) | -0.004(3) | -0.004(2) | 0.001(2) | |
| | $U_{13}$ | 0 | 0 | 0 | 0 | |
| | $U_{23}$ | 0 | 0 | 0 | 0 | |
| H | *x* | -0.403(12) | -0.41(1) | -0.407(11) | -0.402(8) | -0.4125(7) |
| | *y* | 0.25(3) | 0.26(3) | 0.25(3) | 0.259(15) | 0.2866(6) |
| | $U_{iso}$ | 0.06(4) | 0.06(4) | 0.06(4) | 0.05(3) | 0.0159(7) |

Note: General fractional coordinates for atoms: M1 (0 0 0), T2 (x 0.75 0.25), Si1 (-0.5 0 z), Ca (0 0.5 z), O3 (0 0.5 z), OH & H (x y 0), O1 & O2 (x y z)

Table 2.3: Selected bond lengths and distances (Å) in *Pncm*.

| sample ID | | tad1x2 | tad2x1 | tad5x1 | tad4x1 | tad4 N |
|---|---|---|---|---|---|---|
| locality | | Tyrol | Norway | S. Africa | Mali | Mali |
| bond lengths | | | | | | |
| M1-O1 | (x4) | 1.926(4) | 1.919(4) | 1.925(3) | 1.962(2) | 1.9471(14) |
| M1-OH | (x2) | 1.910(5) | 1.907(6) | 1.912(5) | 1.949(4) | 1.9434(17) |
| Poly. Vol. | | 9.443 | 9.357 | 9.442 | 10.003 | |
| | | | | | | |
| T2-O2 | (x2) | 1.677(4) | 1.675(4) | 1.678(4) | 1.689(3) | 1.6736(18) |
| T2-O3 | (x2) | 1.6728(19) | 1.671(2) | 1.6735(18) | 1.6860(15) | 1.6715(12) |
| Poly. Vol. | | 2.343 | 2.336 | 2.345 | 2.397 | |
| | | | | | | |
| Si1-O1 | (x2) | 1.611(4) | 1.611(4) | 1.611(3) | 1.625(3) | 1.6103(16) |
| Si1-O2 | (x2) | 1.638(4) | 1.634(4) | 1.638(4) | 1.649(3) | 1.6403(19) |
| Poly. Vol. | | 2.185 | 2.178 | 2.186 | 2.235 | |
| | | | | | | |
| Ca-O1 | (x2) | 2.374(4) | 2.373(4) | 2.377(4) | 2.394(3) | 2.3793(12) |
| Ca-O2 | (x2) | 2.677(4) | 2.674(5) | 2.675(4) | 2.699(3) | 2.6718(19) |
| Ca-O3 | | 2.428(5) | 2.425(6) | 2.426(5) | 2.443(4) | 2.423(4) |
| Ca-OH | (x2) | 2.334(3) | 2.332(4) | 2.338(3) | 2.357(2) | 2.341(3) |
| | | | | | | |
| OH-H | | 0.97(3) * | 0.97(3) * | 0.97(3) * | 0.95(3) * | 0.963(4) |
| | | | | | | |
| distances | | | | | | |
| Ca…Ca | | 3.671(3) | 3.667(4) | 3.677(3) | 3.715(3) | 3.711(5) |
| O3…O3 | | 8.526(11) | 8.517(12) | 8.53(1) | 8.601(8) | |
| OH...OH | | 5.392(8) | 5.391(9) | 5.393(8) | 5.441(6) | |
| O1…O1 | | 2.883(11) | 2.883(12) | 2.89(1) | 2.904(8) | |
| | | | | | | |
| ellipticity ratio | | | | | | |
| O1…O1/O3…O3 | | 0.338 | 0.338 | 0.339 | 0.338 | |
| OH…OH/O3…O3 | | 0.632 | 0.633 | 0.632 | 0.633 | |

* Note: OH-H distance was constrained to 0.98 +/- 0.03 Å in X-ray refinement

Table 2.4: Selected bond angles (º) and distortion parameters in *Pncm*.

| sample ID | | tad1x2 | tad2x1 | tad5x1 | tad4x1 | tad4 N |
|---|---|---|---|---|---|---|
| locality | | Tyrol | Norway | S. Africa | Mali | Mali |
| **M1** | | | | | | |
| OH-M1-O1 | (x4) | 91.67(16) | 91.59(18) | 91.58(15) | 91.49(11) | 91.62(4) |
| OH-M1-O1 | (x4) | 88.33(16) | 88.41(18) | 88.42(15) | 88.51(11) | 88.38(4) |
| O1-M1-O1 | (x2) | 89.8(2) | 89.9(2) | 89.8(2) | 89.89(15) | 89.79(8) |
| O1-M1-O1 | (x2) | 90.2(2) | 90.1(2) | 90.2(2) | 90.11(15) | 90.21(8) |
| OH-M1-OH | | 180.0 | 180.0 | 180.0 | 180.0 | 180.0 |
| O1-M1-O1 | | 180.0 | 180.0 | 180.0 | 180.0 | 180.0 |
| AV | | 2.050 | 1.823 | 1.830 | 1.601 | |
| QE | | 1.0006 | 1.0005 | 1.0005 | 1.0005 | |
| | | | | | | |
| **T2** | | | | | | |
| O3-T2-O3 | | 116.07(14) | 115.94(17) | 116.09(14) | 116.22(11) | 116.12(12) |
| O3-T2-O2 | (x2) | 110.53(19) | 110.4(2) | 110.52(18) | 110.48(14) | 110.44(8) |
| O3-T2-O2 | (x2) | 99.6(2) | 99.8(2) | 99.6(2) | 99.64(15) | 99.73(9) |
| O2-T2-O2 | | 121.4(3) | 121.4(3) | 121.6(3) | 121.4(2) | 121.37(16) |
| AV | | 76.25 | 75.32 | 78.153 | 76.41 | |
| QE | | 1.0194 | 1.0192 | 1.0199 | 1.0195 | |
| | | | | | | |
| **Si1** | | | | | | |
| O1-Si1-O1 | | 116.1(3) | 116.1(3) | 115.9(3) | 116.14(19) | 116.01(16) |
| O1-Si1-O2 | (x2) | 111.56(19) | 111.4(2) | 111.55(18) | 111.26(13) | 111.28(6) |
| O1-Si1-O2 | (x2) | 104.79(19) | 104.9(2) | 104.87(18) | 104.80(13) | 104.85(6) |
| O2-Si1-O2 | | 107.9(3) | 107.9(3) | 108.0(3) | 108.5(2) | 108.50(16) |
| AV | | 19.77 | 19.03 | 18.943 | 18.995 | |
| QE | | 1.0047 | 1.0045 | 1.0045 | 1.0045 | |
| | | | | | | |
| **Ca** | | | | | | |
| OH-Ca-OH | | 76.3(2) | 76.3(2) | 76.32(19) | 76.03(14) | 75.12(11) |
| O1-Ca-OH | (x2) | 69.18(15) | 69.07(18) | 69.15(15) | 70.13(11) | 70.12(7) |
| O1-Ca-OH | (x2) | 92.33(16) | 92.32(18) | 92.21(15) | 91.70(11) | 91.29(8) |
| O3-Ca-OH | (x2) | 141.85(10) | 141.83(12) | 141.84(9) | 141.99(7) | 142.44(5) |
| O2-Ca-OH | (x2) | 157.72(13) | 157.67(15) | 157.71(12) | 157.72(9) | 157.23(10) |
| O2-Ca-OH | | 82.10(13) | 82.01(15) | 82.05(12) | 82.17(9) | 82.54(4) |
| O1-Ca-O1 | | 156.91(17) | 156.8(2) | 156.71(17) | 157.30(13) | 156.90(14) |
| O3-Ca-O1 | (x2) | 101.55(9) | 101.62(11) | 101.64(8) | 101.35(6) | 101.55(7) |
| O2-Ca-O1 | (x2) | 106.74(13) | 106.85(15) | 106.83(13) | 106.44(10) | 106.54(5) |
| O2-Ca-O1 | (x2) | 84.98(13) | 84.92(15) | 84.97(13) | 85.07(10) | 85.15(4) |
| O2-Ca-O3 | (x2) | 59.94(8) | 60.01(10) | 59.97(8) | 59.95(6) | 60.02(6) |
| O2-Ca-O2 | | 119.88(16) | 120.01(19) | 119.95(15) | 119.90(12) | 120.03(11) |
| | | | | | | |
| T2-O3-T2 | | 155.0(3) | 155.2(4) | 154.9(3) | 154.8(2) | 155.25(15) |
| T2-O2-Si1 | | 140.7(2) | 140.8(3) | 140.7(2) | 140.83(17) | 140.61(10) |
| M1-O1-Si1 | | 129.5(2) | 129.7(3) | 129.5(2) | 129.33(15) | 129.58(6) |
| | | | | | | |
| Ca-O3-T2 | | 102.52(16) | 102.42(19) | 102.56(16) | 102.60(12) | 102.37(7) |
| Ca-OH-M1 | | 101.68(16) | 101.62(19) | 101.57(15) | 100.97(11) | 100.90(5) |
| Ca-OH-Ca | | 103.7(2) | 103.7(2) | 103.68(19) | 103.97(14) | 104.88(11) |
| Ca-O2-Si1 | | 111.26(19) | 111.3(2) | 111.33(18) | 111.69(13) | 111.71(11) |
| Ca-O2-T2 | | 93.02(17) | 92.94(19) | 93.07(16) | 92.94(12) | 92.97(9) |
| Ca-O1-Si1 | | 128.8(2) | 128.6(2) | 128.65(19) | 129.30(14) | 128.96(10) |
| Ca-O1-M1 | | 99.76(16) | 99.86(17) | 99.80(14) | 99.34(10) | 99.48(7) |
| | | | | | | |
| M1-OH-H | | | | | | 112.7(3) |

Table 2.5: Detailed results of single-crystal structure refinements of prehnite in *P2cm*.

| Sample ID | tad1x2* | tad5x1* |
|---|---|---|
| Crystal system | Orthorhombic | Orthorhombic |
| Space group | P 2 c m | P 2 c m |
| Theta range for data collection | 4.32 to 30.02°. | 3.87 to 30.02°. |
| Index ranges | -6<=h<=6, -7<=k<=7, -26<=l<=26 | -6<=h<=6, -7<=k<=7, -26<=l<=26 |
| Reflections collected | 9160 | 8069 |
| Independent reflections | 1407 [R(int) = 0.0553] | 1410 [R(int) = 0.0268] |
| Completeness to theta = 30.00° | 99.60% | 99.70% |
| Absorption correction | Gaussian | Gaussian |
| Max. and min. transmission | 0.94812 and 0.78365 | 0.856 and 0.563 |
| Refinement method | Full-matrix least-squares on $F^2$ | Full-matrix least-squares on $F^2$ |
| Data / restraints / parameters | 1407 / 3 / 82 | 1410 / 3 / 82 |
| Goodness-of-fit on F2 | 1.198 | 1.219 |
| Final R indices [I>2sigma(I)] | $R_1$ = 0.0442, $wR_2$ = 0.1011 | $R_1$ = 0.0226, $wR_2$ = 0.0600 |
| R indices (all data) | $R_1$ = 0.0460, $wR_2$ = 0.1021 | $R_1$ = 0.0227, $wR_2$ = 0.0601 |
| Absolute structure parameter | 0.83(11) | 0.19(6) |
| Largest diff. peak and hole | 0.801 and -0.677 e.Å$^{-3}$ | 0.628 and -0.456 e.Å$^{-3}$ |

Note: See table 2.1 for crystal-specific values (sample info., crystal size, microprobe results, unit cell parameters, density, absorption, etc)

Table 2.6: Positional and displacement parameters for prehnite in *P2cm*.

| sample ID | | tad1x2 | tad5x1 | | | tad1x2 | tad5x1 | | | tad1x2 | tad5x1 | | | tad1x2 | tad5x1 |
|---|---|---|---|---|---|---|---|---|---|---|---|---|---|---|---|
| locality | | Tyrol | S. Africa | | | Tyrol | S. Africa | | | Tyrol | S. Africa | | | Tyrol | S. Africa |
| Ca1 | *x* | 0.0052(5) | 0.0069(2) | O1a | *x* | -0.2436(8) | -0.2445(4) | Si | *x* | 0.4973(5) | 0.4985(3) | OHa | *x* | 0.2118(11) | 0.2118(6) |
| | *y* | 0.5112(2) | 0.5108(1) | | *y* | 0.8803(5) | 0.8799(3) | | *y* | 0.0008(2) | 0.0010(1) | | *y* | 0.7125(9) | 0.7101(5) |
| | *z* | 0.9008(1) | 0.9007(1) | | *z* | 0.9264(2) | 0.9265(1) | | *z* | 0.8805(1) | 0.8805(1) | | *Uiso* | 0.012(1) | 0.008(1) |
| | *Uiso* | 0.013(1) | 0.009(1) | | *Uiso* | 0.013(1) | 0.009(1) | | *Uiso* | 0.009(1) | 0.006(1) | | *U11* | 0.008(1) | 0.005(1) |
| | *U11* | 0.017(1) | 0.012(1) | | *U11* | 0.014(1) | 0.007(1) | | *U11* | 0.009(1) | 0.005(1) | | *U22* | 0.016(1) | 0.010(1) |
| | *U22* | 0.013(1) | 0.009(1) | | *U22* | 0.015(1) | 0.011(1) | | *U22* | 0.011(1) | 0.007(1) | | *U33* | 0.011(1) | 0.010(1) |
| | *U33* | 0.009(1) | 0.007(1) | | *U33* | 0.011(1) | 0.009(1) | | *U33* | 0.008(1) | 0.005(1) | | *U12* | -0.002(1) | 0.000(1) |
| | *U12* | 0.001(1) | 0.000(1) | | *U12* | 0.001(1) | 0.001(1) | | *U12* | 0.000(1) | 0.000(1) | | *U13* | 0 | 0 |
| | *U13* | 0.001(1) | 0.001(1) | | *U13* | 0.000(1) | 0.002(1) | | *U13* | -0.002(1) | -0.001(1) | | *U23* | 0 | 0 |
| | *U23* | 0.000(1) | 0.000(1) | | *U23* | 0.000(1) | 0.000(1) | | *U23* | 0.000(1) | 0.000(1) | | | | |
| | | | | | | | | | | | | OHb | *x* | -0.1988(11) | -0.2006(6) |
| M1 | *x* | 0.0030(7) | 0.0042(4) | O1b | *x* | 0.2565(8) | 0.2550(4) | O2a | *x* | 0.3581(7) | 0.3574(4) | | *y* | 0.3152(8) | 0.3137(5) |
| | *y* | 0.0128(3) | 0.0123(2) | | *y* | 0.1449(5) | 0.1439(3) | | *y* | 0.7789(5) | 0.7797(3) | | *Uiso* | 0.012(1) | 0.008(1) |
| | *Uiso* | 0.009(1) | 0.006(1) | | *z* | 0.9266(2) | 0.9268(1) | | *z* | 0.8332(2) | 0.8329(1) | | *U11* | 0.008(1) | 0.005(1) |
| | *U11* | 0.008(1) | 0.005(1) | | *Uiso* | 0.013(1) | 0.009(1) | | *Uiso* | 0.014(1) | 0.010(1) | | *U22* | 0.016(1) | 0.010(1) |
| | *U22* | 0.012(1) | 0.008(1) | | *U11* | 0.014(1) | 0.007(1) | | *U11* | 0.015(1) | 0.010(1) | | *U33* | 0.011(1) | 0.010(1) |
| | *U33* | 0.008(1) | 0.006(1) | | *U22* | 0.015(1) | 0.011(1) | | *U22* | 0.017(1) | 0.011(1) | | *U12* | -0.002(1) | 0.000(1) |
| | *U12* | 0.001(1) | 0.001(1) | | *U33* | 0.011(1) | 0.009(1) | | *U33* | 0.009(1) | 0.009(1) | | *U13* | 0 | 0 |
| | *U13* | 0 | 0 | | *U12* | 0.001(1) | 0.001(1) | | *U12* | -0.002(1) | 0.000(1) | | *U23* | 0 | 0 |
| | *U23* | 0 | 0 | | *U13* | 0.000(1) | 0.002(1) | | *U13* | 0.001(1) | 0.001(1) | | | | |
| | | | | | *U23* | 0.000(1) | 0.000(1) | | *U23* | 0.001(1) | 0.001(1) | Ha | *x* | 0.416(7) | 0.406(7) |
| T2A | *x* | 0.1909(4) | 0.1906(3) | | | | | | | | | | *y* | 0.708(18) | 0.743(12) |
| | *Uiso* | 0.011(1) | 0.006(1) | T2B | *x* | -0.1917(4) | -0.1922(2) | O2b | *x* | -0.3794(7) | -0.3794(4) | | *Uiso* | 0.046(16) | 0.039(10) |
| | *U11* | 0.012(1) | 0.006(1) | | *Uiso* | 0.011(1) | 0.006(1) | | *y* | 0.2098(5) | 0.2105(3) | | | | |
| | *U22* | 0.011(1) | 0.008(1) | | *U11* | 0.012(1) | 0.006(1) | | *z* | 0.8235(2) | 0.8240(1) | Hb | *x* | -0.399(8) | -0.394(6) |
| | *U33* | 0.009(1) | 0.005(1) | | *U22* | 0.011(1) | 0.008(1) | | *Uiso* | 0.014(1) | 0.010(1) | | *y* | 0.282(17) | 0.289(11) |
| | *U12* | 0 | 0 | | *U33* | 0.009(1) | 0.005(1) | | *U11* | 0.015(1) | 0.010(1) | | *Uiso* | 0.046(16) | 0.039(10) |
| | *U13* | 0 | 0 | | *U12* | 0 | 0 | | *U22* | 0.017(1) | 0.011(1) | | | | |
| | *U23* | 0.000(1) | 0.000(1) | | *U13* | 0 | 0 | | *U33* | 0.009(1) | 0.009(1) | O3 | *x* | -0.0095(12) | -0.0079(7) |
| | | | | | *U23* | 0.000(1) | 0.000(1) | | *U12* | -0.002(1) | 0.000(1) | | *y* | 0.4903(6) | 0.4898(3) |
| | | | | | | | | | *U13* | 0.001(1) | 0.001(1) | | *z* | 0.7695(1) | 0.7697(1) |
| | | | | | | | | | *U23* | 0.001(1) | 0.001(1) | | *Uiso* | 0.015(1) | 0.012(1) |
| | | | | | | | | | | | | | *U11* | 0.016(1) | 0.013(1) |
| | | | | | | | | | | | | | *U22* | 0.016(1) | 0.012(1) |
| | | | | | | | | | | | | | *U33* | 0.013(1) | 0.010(1) |
| | | | | | | | | | | | | | *U12* | -0.005(1) | -0.004(1) |
| | | | | | | | | | | | | | *U13* | 0.002(2) | 0.000(1) |
| | | | | | | | | | | | | | *U23* | -0.001(1) | -0.001(1) |

Note: General fractional coordinates for atoms: M1 (*x y* 0), T2A (*x* 0.75 0.75), T2S (*x* 0.25 0.75), OHa, OHb, Ha & Hb (*x y* 0), Ca, O1a, O1b, O2a, O2b, O3, & Si1 (*x y z*)

Note: Displacement parameters for split sites (i.e. T2A & T2B, O1a & O1b, O2a & O2b, OHa & OHb, Ha & Hb) were constrained to be equal

Table 2.7: Selected bond lengths and distances (Å) in *P2cm*.

| sample ID | | tad1x2 | tad5x1 |
|---|---|---|---|
| locality | | Tyrol | S. Africa |
| bond lengths | | | |
| M1-O1a | (x2) | 1.920(4) | 1.925(2) |
| M1-O1b | (x2) | 1.936(4) | 1.926(2) |
| M1-OHa | | 1.911(6) | 1.917(3) |
| M1-OHb | | 1.905(6) | 1.907(3) |
| Poly. Vol. | | 9.444 | 9.442 |
| | | | |
| T2A-O2a | (x2) | 1.730(3) | 1.726(2) |
| T2A-O3 | (x2) | 1.738(5) | 1.737(3) |
| Poly. Vol. | | 2.553 | 2.538 |
| | | | |
| T2S-O2b | (x2) | 1.629(3) | 1.635(2) |
| T2S-O3 | (x2) | 1.606(4) | 1.611(3) |
| Poly. Vol. | | 2.138 | 2.158 |
| | | | |
| Si1-O1a | | 1.612(4) | 1.607(2) |
| Si1-O1b | | 1.611(4) | 1.618(2) |
| Si1-O2a | | 1.632(4) | 1.637(2) |
| Si1-O2b | | 1.659(3) | 1.654(2) |
| Poly. Vol. | | 2.201 | 2.203 |
| | | | |
| Ca-O1a | | 2.378(4) | 2.385(3) |
| Ca-O1b | | 2.371(4) | 2.368(3) |
| Ca-O2a | | 2.528(4) | 2.527(2) |
| Ca-O2b | | 2.820(4) | 2.816(2) |
| Ca-O3 | | 2.434(3) | 2.4289(17) |
| Ca-OHa | | 2.346(3) | 2.340(2) |
| Ca-OHb | | 2.328(3) | 2.340(2) |
| | | | |
| OHa-Ha | | 0.94(3)* | 0.91(3)* |
| OHb-Hb | | 0.95(3)* | 0.91(3)* |
| | | | |
| distances | | | |
| Ca…Ca | | 3.617(16) | 3.6775(13) |
| O3…O3 | | 8.532(6) | 8.528(4) |
| OH...OH | | 5.389(5) | 5.390(4) |
| O1…O1 | | 2.892(5) | 2.895(4) |
| | | | |
| ellipticity ratio | | | |
| O1…O1/O3…O3 | | 0.339 | 0.339 |
| OH…OH/O3…O3 | | 0.632 | 0.632 |

* Note: OH-H distance was constrained to 0.98 $^{+}$/- 0.03 Å in refinement

Table 2.8: Selected bond angles (º) and distortion parameters in *P2cm*.

| | sample ID<br>locality | tad1x2<br>Tyrol | tad5x1<br>S. Africa |
|---|---|---|---|
| **Ca** | | | |
| | OHb-Ca-OHa | 76.45(10) | 76.42(7) |
| | OHb-Ca-O1b | 69.42(15) | 69.23(9) |
| | OHa-Ca-O1b | 92.38(16) | 92.36(10) |
| | OHb-Ca-O1a | 92.28(16) | 92.02(10) |
| | OHa-Ca-O1a | 68.91(16) | 69.09(9) |
| | O1b-Ca-O1a | 156.87(8) | 156.68(5) |
| | OHb-Ca-O3 | 138.97(16) | 138.67(9) |
| | OHa-Ca-O3 | 144.57(15) | 144.90(9) |
| | O1b-Ca-O3 | 100.07(12) | 100.19(7) |
| | O1a-Ca-O3 | 103.05(12) | 103.09(7) |
| | OHb-Ca-O2a | 157.04(15) | 157.52(9) |
| | OHa-Ca-O2a | 81.38(14) | 81.78(9) |
| | O1b-Ca-O2a | 105.97(16) | 106.68(10) |
| | O1a-Ca-O2a | 85.22(13) | 85.21(9) |
| | O3-Ca-O2a | 63.35(13) | 63.26(7) |
| | OHb-Ca-O2b | 82.70(14) | 82.22(9) |
| | OHa-Ca-O2b | 158.49(14) | 157.97(8) |
| | O1b-Ca-O2b | 85.10(13) | 84.98(9) |
| | O1a-Ca-O2b | 107.16(16) | 106.77(10) |
| | O3-Ca-O2b | 56.51(12) | 56.69(7) |
| | O2a-Ca-O2b | 119.87(8) | 119.95(6) |
| **M1** | | | |
| | OHb-M1-O1a (x2) | 92.2(2) | 91.74(12) |
| | OHa-M1-O1a (x2) | 88.51(17) | 88.45(10) |
| | OHb-M1-O1b (x2) | 88.34(16) | 88.51(10) |
| | OHa-M1-O1b (x2) | 90.9(2) | 91.29(12) |
| | O1a-M1-O1a | 90.3(2) | 89.98(14) |
| | O1a-M1-O1b (x2) | 90.27(11) | 90.25(7) |
| | O1b-M1-O1b | 89.1(2) | 89.52(14) |
| | O1a-M1-O1b | 179.2(3) | 179.65(14) |
| | OHb-M1-OHa | 179.0(3) | 179.7(2) |
| | AV | 2.039 | 1.733 |
| | QE | 1.0006 | 1.0005 |
| **T2A** | | | |
| | O2a-T2A-O2a | 126.9(3) | 126.84(16) |
| | O2a-T2A-O3 (x2) | 97.45(15) | 97.35(9) |
| | O2a-T2A-O3 (x2) | 110.36(15) | 110.21(9) |
| | O3-T2A-O3 | 115.5(4) | 116.1(2) |
| | AV | 125.773 | 128.365 |
| | QE | 1.0319 | 1.0327 |
| **T2S** | | | |
| | O3-T2S-O3 | 116.7(4) | 116.0(2) |
| | O3-T2S-O2b (x2) | 110.86(17) | 111.19(10) |
| | O3-T2S-O2b (x2) | 101.78(16) | 101.51(10) |
| | O2b-T2S-O2b | 115.5(3) | 116.03(16) |
| | AV | 42.013 | 43.784 |
| | QE | 1.0106 | 1.0111 |

| | sample ID<br>locality | tad1x2<br>Tyrol | tad5x1<br>S. Africa |
|---|---|---|---|
| **Si1** | | | |
| | O1a-Si1-O1b | 115.89(13) | 115.81(9) |
| | O1a-Si1-O2a | 105.68(18) | 105.85(11) |
| | O1b-Si1-O2a | 112.2(3) | 111.53(15) |
| | O1a-Si1-O2b | 111.3(2) | 111.72(15) |
| | O1b-Si1-O2b | 103.61(18) | 103.64(11) |
| | O2a-Si1-O2b | 108.13(14) | 108.18(9) |
| | AV | 20.447 | 19.629 |
| | QE | 1.0049 | 1.0047 |
| **O-central angles** | | | |
| | Si1-O1a-M1 | 131.4(2) | 131.37(12) |
| | Si1-O1a-Ca | 127.19(17) | 127.35(10) |
| | M1-O1a-Ca | 100.15(19) | 99.82(11) |
| | Si1-O1b-M1 | 127.40(19) | 127.64(12) |
| | Si1-O1b-Ca | 130.45(17) | 129.93(10) |
| | M1-O1b-Ca | 99.28(18) | 99.82(11) |
| | Si1-O2a-T2A | 136.20(19) | 136.66(11) |
| | Si1-O2a-Ca | 115.06(15) | 114.99(10) |
| | T2A-O2a-Ca | 95.62(16) | 95.69(10) |
| | T2S-O2b-Si1 | 143.9(2) | 143.42(12) |
| | T2S-O2b-Ca | 90.41(14) | 90.48(9) |
| | Si1-O2b-Ca | 107.49(15) | 107.78(9) |
| | T2S-O3-T2A | 155.10(17) | 154.82(10) |
| | T2S-O3-Ca | 106.09(15) | 106.24(9) |
| | T2A-O3-Ca | 98.81(14) | 98.94(8) |
| | M1-OHa-Ca | 101.53(19) | 101.63(11) |
| | Ca-OHa-Ca | 103.0(2) | 103.57(12) |
| | M1-OHa-Ha | 122(6) | 109(4) |
| | M1-OHb-Ca | 101.75(19) | 101.38(11) |
| | Ca-OHb-Ca | 104.1(2) | 103.58(12) |
| | M1-OHb-Hb | 108(6) | 111(4) |

*2.4.1 Pncm*

The unit-cell parameters for each sample (Table 2.1) are in general agreement with previously published studies (Papike & Zoltai, 1967; Peng *et al.*, 1959). Crystal tad4x1 has a larger unit cell, by approximately 2% in all directions, than the other samples, presumably due to the expansion of the octahedral site upon substitution of Fe for Al. The substitution of Fe for Al on the octahedral site results in a significant expansion of the M1-O bond lengths. In tad4x1, with 26% Fe, the M1-O1 bond length is 1.962(2) Å and the M1-OH bond length is 1.949(4) Å, whereas in the other samples, with 7% or less iron, the octahedral bond lengths are all less than 1.93 Å (Table 2.3). Although the iron was experimentally found to be only on the octahedral site (Artioli *et al.*, 1995; Akasaka *et al.*, 2003), the tetrahedral bond lengths also show a general lengthening with the the higher iron content in sample tad4x1. For example, the Si-O2 bond lengthens to 1.649(3) Å, whereas the other samples have an average Si-O2 bond length of 1.637 Å. Other bond lengths that follow the same trend include T2-O2, T2-O3, and Si-O1. The distortion parameters, angular variance and quadratic elongation of the framework polyhedra do not vary among the samples (Table 2.4). The unit-cell parameters and bond lengths in the remaining samples with less than 7% Fe show no significant variation with Mn or Fe content.

Higher Fe content in the prehnite structure therefore seems to produce a fairly uniform expansion of the tetrahedral/octahedral framework. This is reflected in the geometry of the Ca site. Thus, within the area of the calcium channel, the distance between the calcium atoms is larger in tad4x1. The presence of iron in the structure spreads the calcium atoms apart, pushing the oxygen atoms as well and increasing the Ca-O bond lengths (Figure 2.2, Table 2.3). The three oxygen atoms surrounding the channel, OH & O1 & O3, are separated further from each other on opposite sides of the channel in tad4x1, with distances of 5.441(6) Å, 2.904(8) Å, and 8.601(8) Å respectively, as compared to values of ~5.39 Å, ~2.88 Å, and ~8.52 Å in the samples with lower iron contents. However, the ellipticity ratio of the calcium cavity remains constant. Oxygen-central angles Ca-O1-M1 & Ca-OH-M1 become smaller at angles of 99.34(10) º and 100.97(11) º, while the Ca-OH-Ca, Ca-O2-Si and Ca-O1-Si1 become larger, with angles of 103.97(14) º, 111.69(13) º, and 129.30(14) º respectively. The Ca-central angles O1-Ca-OH and OH-Ca-OH become smaller than the other localities, at angles of 99.34(10) º and 76.03(14) º. The bond

angles do not change between the other localities with the addition of lower percentages of iron or manganese in the structure.

The hydrogen atom in the structure was located in the X-ray difference-Fourier maps on the oxygen atom OH pointing away from the direction of the calcium channel, within the mirror plane in the *c* plane. The OH oxygen is the under-bonded oxygen, coordinated only to the M1 octahedron (Figure 2.1). This position was confirmed by the observation that the addition of the hydrogen atom into the structure dropped the weighted-Chi-squared of the refinement to the neutron powder diffraction data from 128 to 19.07. The coordinates of the H-atom refined to the neutron diffraction data are (-0.4125(7), 0.2866(6), 0), and the OH-H distance is 0.963(4) Å. The next closest oxygen atoms are the two O1 atoms that are connected to a neighboring octahedron, each with a O1…H distance of 2.25 Å. That makes the total distance from OH-H…O1 to be 3.03 Å, with an OH-H-O angle of 137.3 º (Figure 2.3). If this represents a hydrogen bond, then the environment is bifurcated as a result of mirror symmetry in the average *Pncm* structure, which is maintained in the lower symmetry *P2cm* structure.

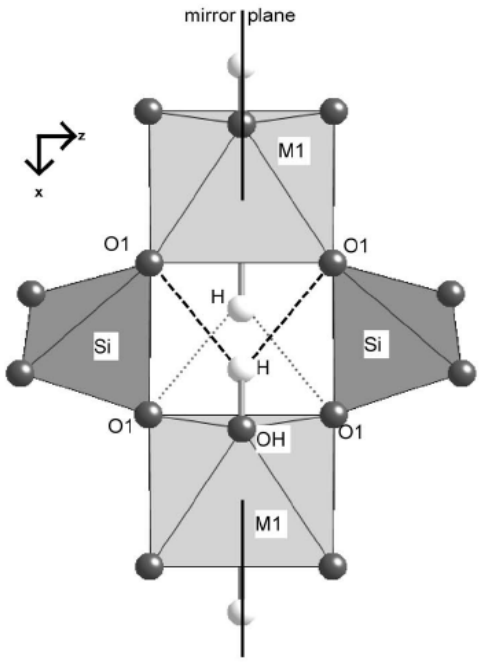


Figure 2.3: The hydrogen environment of prehnite as viewed from [010]. The small gray spheres represent oxygen sites, whereas the small white spheres represent hydrogen sites. The heavy dash shows the bifurcated environment of the H and the next nearest oxygen, O1. The light dash shows the bifurcated environment of the H and O1 on the lower apex of the octahedron.

*2.4.2 P2cm*

In the average space group, *Pncm*, the tetrahedral sites are a fully-occupied Si-tetrahedron and a disordered T2 site containing $Al_{0.5}Si_{0.5}$. Papike and Zoltai (1967) showed that there are only three ordering patterns for Al/Si on the T2 site- with space group symmetries *P2cm*, *P2/n*, and $P22_12$. One of the potential space groups, $P22_12$, leads to Al-O-Al linkages and is thus considered unlikely to occur (*cf.* Lowenstein, 1954), and no evidence for this space group has ever been found. The other two space groups, *P2cm* and *P2/n*, can be distinguished by the presence of systematic absence violations of the *n*-glide and the *c*-glide in *Pncm*, respectively. It was found that the diffraction pattern from crystal tad1x2 had 149 systematic absence violations of the *n*-glide condition and just 3 of the *c*-glide. Crystal tad5x1 had 422 violations of the *n*-glide condition and 188 of the *c*-glide. The violations therefore suggest that the dominant ordering pattern has *P2cm* symmetry. The remaining crystals, tad2x1 and tad4x1, show <60 systematic absence violations so the limited data did not allow refinement of an ordered structure model. Therefore refinements to datasets tad1x2 and tad5x1 were performed in *P2cm*, and the results from tad5x1 are discussed here. Results from tad1x2 are the same within the (larger) esd's.

In the transition from *Pncm* to *P2cm*, the atom sites T2, O1, O2, OH, and H split to become two unique sites each. The octahedral M1 site, sitting on Wyckoff position a in *Pncm* sits on Wyckoff position c in *P2cm*. The disordered T2 site splits into an aluminum-rich site (T22), sitting on Wyckoff position b in *P2cm*, and a silicon-rich site (T21) sitting on Wyckoff position a. OH and H positions, sitting on Wyckoff position h in *Pncm* splits into two unique sites each (OHa, OHb, Ha, and Hb) and all sit on Wyckoff position c in *P2cm*. The calcium atom, previously located on Wyckoff position e, sits on a GEP in *P2cm*, along with O1a, O1b, O2a, O2b, and O3. In the refinements, it was found necessary to constrain the oxygen anisotropic displacement parameters of the pairs of split oxygen sites to be equal in order for the refinement to remain stable.

The largest change in the structure upon reducing the symmetry from *Pncm* to *P2cm* is the development of a clear distinction between the T2A and T2S sites. This was clearly apparent in both refinements, with a T2S-O average bond length of 1.623 Å and a T2A-O average bond length of 1.732 Å (Table 2.7), which are in agreement with those previously published (Balić-

Žunić *et al.,* 1990). The bond lengths suggest full Al,Si ordering on the T2 site.

In *P2cm*, the silicon tetrahedron remains a single site, occupied only by Si, but the site symmetry is reduced from 2 to 1. Nonetheless, there are significant changes in the geometry of the $SiO_4$ tetrahedron as a consequence of the ordering of Al and Si on T2. The Si-O2b bond becomes longer at 1.654(2) Å, because the O2b atom is bonded to the T2S site, containing silicon. Conversely, the Si-O2a bond is shorter because the O2a atom is bonded to the Al-containing T2A site. The same patterns of tetrahedral distortions due to neighbouring tetrahedral sites is seen in feldspars (Phillips & Ribbe, 1973; Angel *et al.*, 1990), and reflect the need for local charge balance on the bridging oxygen atom. For the same reason (e.g. Geisinger *et al.*, 1985), the Si-O2a-T2A is reduced from an average of 140.7(2) º in *Pncm* to 136.66(11) º and the Si-O2b-T2S angle is increased to 143.42(12) º. Note that the Si-O1a & Si-O1b bonds remain unchanged, because the O1 oxygen forms the bridge to the octahedral site (Table 2.7).

The calcium atom, previously sitting on a site with two-fold symmetry becomes a GEP in *P2cm*, so all of the Ca-O bonds become unique. The biggest changes occur in the length of Ca-O2 bonds and angles, which again can be interpreted as a consequence of ordering of Al and Si on the T2 site, and the need to maintain local charge balance at the oxygen positions. The Ca-O2b bond length increases from 2.675(4) Å in *Pncm* to 2.816(2) Å in *P2cm*, because the O2b atom is bonded to the Si-containing T2S site, while the Ca-O2a bond decreases to 2.527(2) Å, because the O2a atom is bonded to T2A (Figure 2.2, Table 2.7). These changes also contribute to small changes in bond angles- especially those involving O2 sites.

The octahedral M1 site, containing aluminum and iron, which previously sat on a site with 2/m symmetry, sits only on a mirror. So, instead of Al-O1 and Al-OH being symmetry unique bond lengths, the M1 site is now coordinated to two O1a, two O1b, OHa and OHb. However, because the symmetry-breaking process (Al, Si ordering on T2) is not directly associated with changes on the octahedral site, there are only small changes in its geometry. The bond length M1-O1a decreases to 1.920(4) Å and M1-O1b increases to 1.936(4) Å in sample tad1x2 while in sample tad5x1 both bond lengths remain the same as *Pncm* values (1.925(3) Å). This small difference may reflect the different octahedral site occupancies (Table 2.1). The M1-OHa and M1-OHb

bond lengths change from an average *Pncm* value of 1.912(5) Å to 1.917(3) Å and 1.907(3) Å in *P2cm*.

The hydrogen atoms were located in difference-Fourier maps using only X-ray data (not the powder neutron data). The splitting of the hydrogen site in *P2cm* maintains the site symmetry of the hydrogen that sits on a mirror plane; however it splits into two unique sites that are nonequivalent on opposite apices of the octahedron. Each of the two non-equivalent H positions (Ha and Hb) thus retains mirror symmetry and each, as a result, has a pair of symmetry-equivalent O1 atoms on the adjacent octahedron as the next nearest oxygen atoms. Therefore, if there is bifurcated hydrogen bonding in prehnite, it is not an artifact of averaging in space group *Pncm*, but must be present in the true local *P2cm* symmetry of the structure.

## 2.5 Conclusions

Hydrogen was located for the first time using difference-Fourier maps and its position was refined using powder neutron diffraction data. It has been established that the hydrogen atom is located on the apex of the octahedron, attached to the OH atom in agreement with bond valance calculations. The O-H vector points away from the adjacent calcium atoms. Symmetry requires that, if the H participates in a hydrogen bond, it must be bifurcated, and involve two oxygen atoms on one adjacent octahedron.

All four prehnite crystals studied have an average structure with symmetry *Pncm* symmetry, but all show evidence of Al,Si ordering in the form of violations of both the *c*- and *n*-glides. Given that the number of *n*-glide violations always exceeds those of the *c*-glide, it appears that the ordering pattern with *P2cm* symmetry is the dominant one in all of the prehnite samples examined. This suggests that the *P2/n* ordering scheme, if present, is present in either very small domains, perhaps restricted to the walls between the adjacent *P2cm* anti-phase domains. The fact that both of the two samples could be refined in the ordered *P2cm* symmetry appear to have fully-ordered distributions of Al and Si, perhaps suggests that all natural prehnites contain completely ordered Al/Si distributions, at least on a local length scale. The fact only a small number of *Pncm* violations are observed in the diffraction patterns of the other samples could

then be attributed to domains being small. If this is correct, then there will be no contributions to the configurational entropy of prehnite from disorder of either aluminum or silicon or from hydrogen.

## 2.6 References


Akasaka, M., Hashimoto, H., Makino, K., and Hino, R. (2003): $^{57}$Fe Mossbauer and X-ray Rietveld studies of ferrian prehnite from Kouragahana, Shimane Peninsula, Japan. *Journal of Mineralogical and Petrological Sciences*, 98, 31-40.

Akizuki, M. (1987): Al,Si order and the internal texture of prehnite. *Canadian Mineralogist*, 25, 707-716.

Angel, R.J., Carpenter, M.A., and Finger, L.W. (1990): Structural variation associated with the compositional variation and order-disorder behavior in anorthite-rich feldspars. *American Mineralogist*, 75, 150-162.

Artioli, G., Quartieri, S., and Deriu, A. (1995): Spectroscopic data on coexisting prehnite-pumpellyite and epidote-pumpellyite. *Canadian Mineralogist*, 33, 67-75.

Aumento, F. (1968): The space group of prehnite. *Canadian Mineralogist*, 9, 485-492.

Balić-Žunić, T., Šćavničar, S., and Molin, G. (1990): Crystal structure of prehnite from Komiža. *European Journal of Mineralogy*, 2, 731-734.

Baur, W.H., and Hofmeister, W. (1990): Prehnite: structural similarity of the monoclinic and orthorhombic polymorphs and their Si/Al ordering. *Journal of Solid State Chemistry*, 86, 330-333.

Berry, A.J., and James, M. (2002): Refinement of hydrogen positions in natural chondrodite by powder neutron diffraction: implications for the stability of humite minerals. *Mineralogical Magazine*, 66, 441-449.

Farrugia, L.J. (1999): WinGX suite for small-molecule single-crystal crystallography. *Journal of Applied Crystallography*, 32, 837-838.

Geisinger, K.L., Gibbs, G.V., and Navrotsky, A. (1985): A molecular orbital study of bond length and angle variations in framework silicates. *Physics and Chemistry of Minerals*, 11, 266-283.

Lowenstein, W. (1954): The distribution of aluminum in the tetrahedra of silicates and aluminates. *American Mineralogist*, 39, 92-96.

Nuffield, E.W. (1943): Prehnite from Ashcroft, British Columbia. *University of Toronto Studies*, 48, 49-64.

Papike, J.J., and Zoltai, T. (1967): Ordering of tetrahedral aluminum in prehnite $Ca_2(AlFe^{+3})[Si_3AlO_{10}](OH)_2$. *American Mineralogist*, 52, 974-984.

Peng, S.-T., Chou, K.-D., and Tang, Y.-C. (1959): The structure of prehnite. *Acta Chemistry Sinica*, 25, 56-63.

Phillips, M.W., and Ribbe, P.H. (1973): The variation of tetrahedral bond lengths in sodic plagioclase feldspars. *Contributions to Mineralogy & Petrology*, 39, 327-339.

Preisinger, A. (1965): Prehnit- ein neuer Schichtsilikattyp. *Tschermaks Mineralogische und Petrograpische Mitteilungen*, 10, 491-504.

Sheldrick, G.M. (2008): A short history of SHELX. *Acta Cryst.*, A64, 112-122.

Traube, H. (1894): Üeber die pyroelecktrischen Eigenschaften und die Krystallformen des Prehnits. *Neues Jahrbuch für Mineralogie*, 9, 134-146.

Welch, M.D., Marshall, W.G., Ross, N.L., and Knight, K.S. (2002): H positions in leucophoenicite, $Mn_7Si_3O_{12}(OH)_2$: A close relative of the hydrous B phases. *American Mineralogist*, 87, 154-159.

# Chapter 3: Equation of state and structure of prehnite to 9.8 GPa

## 3.1 Abstract

The equation of state and high-pressure behavior of a natural sample of prehnite from Kuruman, South Africa, $Ca_{2.07}(Al_{0.98}, Mn_{0.02})(AlSi_{3.09}O_{10})(OH)_2$, have been investigated using single crystal X-ray diffraction up to 9.75(3) GPa. A second-order Birch–Murnaghan equation-of-state fit to the isothermal P-V data below 8.7 GPa yields values of K = 109.29(18) GPa and K'=4. A third-order Birch-Murnaghan equation fit to the P-V data results in K' values equal to 4, within an estimated standard deviation. The compressibility of *a*, *b*, and *c* unit-cell parameters is non-linear and strongly anisotropic, with room-pressure moduli of $K_{a0}$= 83.5(7) GPa, $K_{b0}$= 113(1) GPa, and $K_{c0}$ = 146(3) GPa and $K'_{a0}$=4.5(3), $K'_{b0}$=1.3(3), and $K'_{c0}$=8.8(8). Intensity data were collected over the entire pressure range. Bond lengths and angles, refined in the average space group *Pncm*, suggest that the structure compresses uniformly. Above 8.7 GPa there is an additional softening of the volume and the *b*-axis, but the average structure is maintained across the transition.

## 3.2 Introduction

As described in Chapter 2, the prehnite structure contains $SiO_4$ and $AlO_4$ tetrahedra, and $AlO_4(OH)_2$ octahedra, which are linked together by sharing oxygen atoms so as to form 3-dimensional corner-linked polyhedral framework (Figure 3.1). The T1 and T2 tetrahedra form spirals with an axis parallel to [010], with the T1 tetrahedra also forming 4-rings containing two T1 tetrahedra and two octahedra each. This topology makes prehnite very different from the tetrahedral frameworks that have been studied previously at high pressures, such as feldspars, because the octahedra in prehnite form an essential element of the framework. In this sense, prehnite is more similar to the titanite structure, in which the high-pressure behavior (Rath *et al.*, 2003; Angel *et al.*, 1999) has been shown to depend on the properties of the octahedral-tetrahedral framework modified by the interaction between the framework and the extra-framework cation.

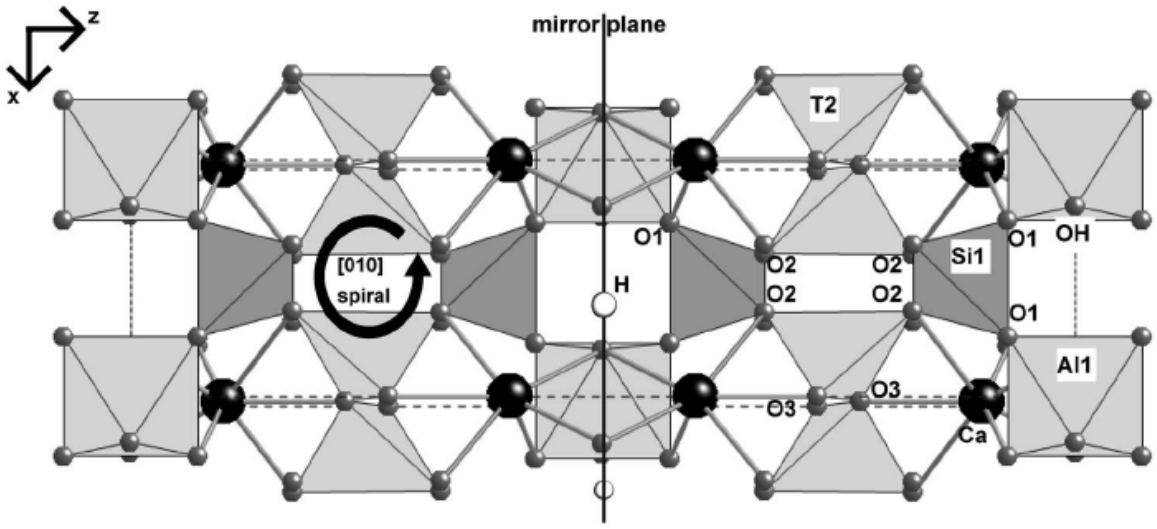


Figure 3.1: The prehnite structure as viewed from a direction 2º from [010]. All of the polyhedra are connected by corner-sharing. The large black spheres represent Ca sites, whereas the small gray spheres represent oxygen sites. Hydrogen sites, the small white spheres, are located on the apices of the octahedron that are not connected to neighboring tetrahedra (Chapter 2). The corner-connected tetrahedra form a spiral parallel to [010].

The tetrahedral sites, T1 and T2, are occupied by silicon and aluminum as described below. The octahedron contains aluminum, along with any iron in the structure (Artioli *et al.*, 1995; Akasaka *et al.*, 2003). There is a channel in the structure, parallel to [100], where a calcium atom resides in 7-fold coordination by oxygen atoms (Figure 3.2). Recent structure refinements to X-ray and neutron diffraction data have confirmed that the hydrogen is bonded to an oxygen atom of the octahedron which does not participate in any links between the octahedra and tetrahedra (Chapter 2). As noted by Papike & Zoltai (1967), prehnite has an "average structure" with symmetry described in space group *Pncm*. In single-crystal X-ray diffraction studies, however, weak reflections violating the *n*-glide are observed that indicate that the true space group symmetry is *P2cm* (Papike & Zoltai, 1967; Aumento, 1968; Balić-Žunić *et al.*, 1990; Preisinger, 1965; Chapter 2). These reflections arise because of ordering of Al and Si in the tetrahedral sites. Thus in *Pncm*, T1 is occupied solely by Si and T2 with disordered Al and Si. In *P2cm*, T1 remains a single site and contains Si, and T2 splits into two distinct sites, with one fully occupied by Al and the second by Si. This arrangement results in complete “Al-avoidance” (Lowenstein, 1954) in the structure, in that there are neither any $Al^{VI}$-O-$Al^{IV}$ nor any $Al^{IV}$-O-$Al^{IV}$ linkages. Other sites also split due to the lower symmetry, shifting from special positions in *Pncm* to general equivalent positions in *P2cm*.

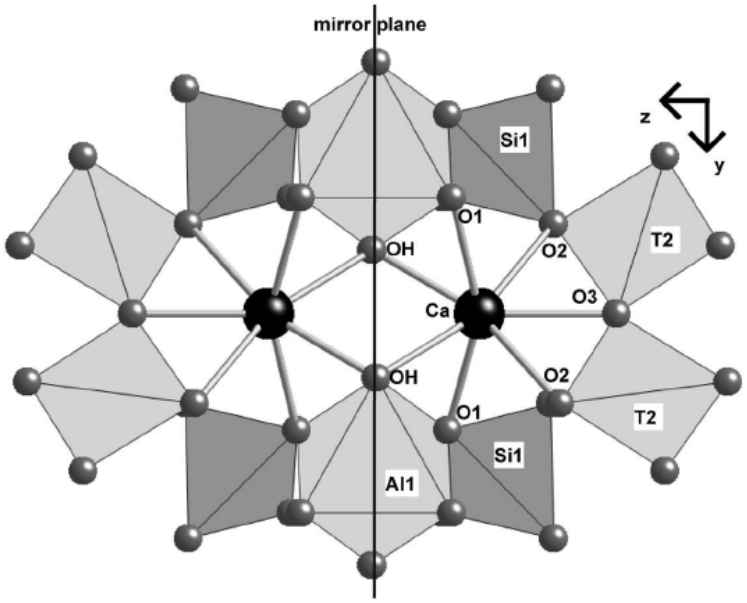


Figure 3.2: The Ca-channel in prehnite as viewed from a direction 2º from [100]. The large black spheres represent the Ca sites, whereas the small gray spheres represent the oxygen sites.

High pressure is commonly used as a probe to gain understanding of the crystal chemistry, elastic properties and stabilities of minerals. The equation of state of prehnite has not been determined, even though it is an important metamorphic mineral, and its bulk modulus has only been "estimated" in commonly-used thermodynamic databases (e.g. Holland & Powell, 1998). Similarly, there have not been any high-pressure structural studies of prehnite even though it has a unique crystal structure that has some aspects in common with layer structures as well as framework structures. In this study I have determined the equation of state and axial moduli of prehnite, and report the results of structure refinements completed to 9.8 GPa that shed light on the compression mechanisms of prehnite at high pressure.

### 3.3 Experimental Methods

A prehnite sample was provided by Dr. R. Pagano (Milano, Italy) from N'Chwaning II mine, Kuruman, South Africa (#8789). Quantitative chemical analyses in EMPA-WDS were obtained on polished single-crystals of four prehnite crystals from this sample, optically free of defects, using a JEOL JXA-8200 electron microprobe at the Dipartimento di Scienze della Terra - Milano. The system was operated using a defocused electron beam (∅ 5 μm) at an accelerating

voltage of 15 kV, a beam current of 15 nA and a counting time of 20 s on the peaks and 5 s on the backgrounds. Natural minerals (K-feldspar for Si, K, Al, forsterite for Mg, rhodonite for Mn, wollastonite for Ca, omphacite for Na, ilmenite for Ti, fayalite for Fe) were used as standards. The results were corrected for matrix effects using a conventional ZAF routine in the JEOL suite of programs. The resulting chemical formula, $Ca_{2.07}(Al_{0.98}, Mn_{0.02})(AlSi_{3.09}O_{10})(OH)_2$, represents an average of 11 analyses and was calculated on a 12-oxygen basis.

Three single crystals cut from the same original single crystal were loaded consecutively into diamond anvil cells for high-pressure studies. Prehnite crystal tad5x1, measuring 135 x 80 x 60, crystal tad5x4, measuring 110 x 120 x 60 μm, and crystal tad5x6, measuring 100 x 60 x 40 μm were chosen based on optical and diffraction quality. Two larger crystals (tad5x1 and tad5x4) were used in measurements up to 6-7 GPa. A smaller crystal was used for measurements at higher pressures, with a consequent decrease in data quality. Each crystal was loaded into an ETH-type diamond anvil cell (Miletich *et al.*, 2000) with 600 μm culets and T301 steel gaskets (tad5x1 gasket diameter= 280 μm thickness: 113 μm; tad5x4 gasket diameter= 300μm thickness: 120 μm; tad5x6 gasket diameter= 240 μm, thickness: 80 μm) along with a quartz crystal and ruby sphere for pressure calibration. In each loading, the crystals were oriented with (001) cleavage faces parallel to the diamond culets. Although this direction is not ideal, the dominant cleavage of prehnite prevents preparation of crystals in other orientations.

A Huber four-circle diffractometer, powered to 50 kV, 40 mA with MoKα radiation was used to collect unit cell parameters. Room pressure (no fluid) unit cell parameters were collected and 4:1 methanol:ethanol fluid was subsequently loaded into the diamond anvil cell (as pressure medium) and the cell was taken to higher pressures. The experiment with crystal tad5x1 reached 6.8 GPa and that with crystal tad5x4 reached 6.4 GPa before the crystals bridged the diamonds. Data from bridged samples were not used in any of the subsequent analyses. The thinner crystal tad5x6 reached 9.75(3) GPa and was subsequently also measured at several pressures during decompression. Unit-cell parameters were determined based on 8-position centering of 10-18 reflections, $10^\circ \leq 2\theta \leq 24^\circ$, following the procedure outlined by King & Finger (1979), using the vector least-squares method (Ralph & Finger, 1982). The pressure in the cell was determined using the volume of the quartz crystal, as in Angel *et al.* (1997). The P-V data of the prehnite

crystals were used to obtain the Equation of State parameters in program EOSfit5.2 (Angel, 2000), using a Birch-Murnaghan EoS. Weights in the refinement of the EoS's were calculated from the esd's of the unit-cell volumes combined with the uncertainty in pressure corresponding to the esd's of the unit-cell volumes of the quartz pressure standard. Unit cell parameters are reported in Table 3.1.

Table 3.1: Unit-cell parameters of prehnite, *Pncm*, from 1 bar to 9.75(3) GPa.

| | Pressure (GPa) | $V$ (Å$^3$) | $a$ (Å) | $b$ (Å) | $c$ (Å) |
|---|---|---|---|---|---|
| Tad5x1 | 0.0001 | 468.44(6) | 4.6248(4) | 5.4825(4) | 18.475(1) |
| | 0.659(6) | 465.56(5) | 4.6125(4) | 5.4717(4) | 18.4460(11) |
| | 1.460(5) | 462.28(5) | 4.5987(4) | 5.4586(4) | 18.416(1) |
| | 1.952(6) | 460.32(5) | 4.5905(3) | 5.4508(4) | 18.3970(9) |
| | 3.012(7) | 456.24(6) | 4.5732(3) | 5.4341(4) | 18.3593(9) |
| | 4.279(8) | 451.66(5) | 4.5539(3) | 5.4148(3) | 18.317(1) |
| | 3.878(7) | 453.05(7) | 4.5596(5) | 5.4205(5) | 18.3306(14) |
| | 2.482(6) | 458.30(9) | 4.5822(6) | 5.4418(6) | 18.3795(17) |
| | 4.976(7) | 449.24(5) | 4.5439(4) | 5.4042(4) | 18.2943(9) |
| Tad5x4 | 0.0001 | 468.42(3) | 4.62458(16) | 5.48166(17) | 18.4778(5) |
| | 0.020(6) | 468.30(4) | 4.6236(3) | 5.4816(3) | 18.4769(7) |
| | 2.439(5) | 458.48(3) | 4.58221(19) | 5.4428(2) | 18.3833(6) |
| | 5.111(5) | 448.8(1) | 4.5414(7) | 5.4023(7) | 18.2913(18) |
| | 5.272(6) | 448.10(4) | 4.5391(3) | 5.3992(3) | 18.2841(8) |
| | 5.905(8) | 445.96(4) | 4.5303(3) | 5.3899(3) | 18.2640(8) |
| | 6.408(14) | 444.34(4) | 4.5236(3) | 5.3828(3) | 18.2482(8) |
| | 6.79(1) | 443.07(3) | 4.51851(18) | 5.37697(19) | 18.2362(5) |
| Tad5x6 | 0.0001 | 468.54(6) | 4.6248(4) | 5.4824(4) | 18.4795(12) |
| | 2.792(3) | 457.29(17) | 4.5771(7) | 5.4376(7) | 18.374(6) |
| | 5.560(7) | 447.35(16) | 4.536(1) | 5.3958(11) | 18.278(4) |
| | 5.919(14) | 446.10(14) | 4.5310(9) | 5.3903(9) | 18.265(4) |
| | 6.873(9) | 442.90(16) | 4.518(1) | 5.376(1) | 18.235(4) |
| | 6.975(15) | 442.64(14) | 4.5168(9) | 5.3747(9) | 18.234(4) |
| | 7.818(15) | 439.90(14) | 4.5058(9) | 5.3618(9) | 18.208(4) |
| | 8.207(9) | 438.62(15) | 4.5008(9) | 5.356(1) | 18.196(4) |
| | 8.574(13) | 437.51(14) | 4.4963(9) | 5.350(1) | 18.188(4) |
| | 8.68(1) | 437.11(15) | 4.495(1) | 5.348(1) | 18.185(4) |
| | 9.03(1) | 435.97(15) | 4.4904(9) | 5.342(1) | 18.174(4) |
| | 9.345(11) | 434.84(15) | 4.4868(9) | 5.335(1) | 18.168(4) |
| | 9.75(3) | 432.10(16) | 4.482(1) | 5.3201(11) | 18.161(4) |

Note: the figures in parentheses represent 1 e.s.d. of last decimal place shown.

Intensity X-ray data were collected at varying pressures on an Oxford Diffraction Xcalibur-2$^{TM}$ single-crystal diffractometer with a point detector, with the tube powered to 50 kV and 40 mA. The data were collected over a 2θ range of 2º to 80º with an omega step scans of 0.02º step size, with a scan width of 1.2º. Scan times were adjusted in a "constant precision" mode. Following

the data collection, peaks were integrated with the program Win-IntegrStp v.3.5 (Angel, 2003), corrected for absorption by the crystal, the diamond anvil cell, and the gasket using Absorb6.0 (Angel, 2004a), and subsequently averaged with the Average program (Angel, unpub) which implements the statistical methods of Blessing (1987).

Structure refinements (using neutral atom scattering factors) were performed in Shelxl-97 (Sheldrick, 2008), driven by WinGX (Farrugia, 1999), using a starting model based on the structure refined in space group *Pncm* at room pressure (Chapter 2). I was not able to refine the structure in *P2cm* because insufficient *n*-glide violations were observed in the data collected in the DAC. Tables 3.2, 3.3, 3.4, and 3.5 show details of the refinements, refined atomic positions, and selected bond lengths and angles, respectively.

Table 3.2: Structure refinement results for prehnite.

| sample ID | tad5x1 | tad5x1 | tad5x1 | tad5x4 | tad5x4 | tad5x6 | tad5x6 | tad5x6 | tad5x6 | tad5x6 |
|---|---|---|---|---|---|---|---|---|---|---|
| Pressure (GPa) | 0.0001 | 1.952(6) | 4.279(8) | 5.111(5) | 6.408(14) | 7.818(15) | 8.207(9) | 9.03(1) | 9.345(11) | 9.75(3) |
| F(000) | 408 | 408 | 408 | 408 | 408 | 408 | 408 | 408 | 408 | 408 |
| $\mu$ ($mm^{-1}$) | 1.85 | 1.89 | 1.93 | 1.94 | 1.96 | 1.98 | 1.99 | 2 | 2 | 2.01 |
| $D_x$ ($g/cm^3$) | 2.9 | 2.961 | 3.018 | 3.037 | 3.066 | 3.099 | 3.107 | 3.126 | 3.134 | 3.148 |
| sys abs violations | 8 | 13 | 13 | 0 | 12 | 3 | 1 | 2 | 3 | 3 |
| unique reflections | 329 | 469 | 469 | 329 | 326 | 296 | 305 | 311 | 303 | 307 |
| F(o)>4sigF(o) | 261 | 354 | 354 | 281 | 272 | 162 | 154 | 179 | 169 | 182 |
| R(int) | 0.077 | 0.057 | 0.057 | 0.064 | 0.059 | 0.255 | 0.213 | 0.141 | 0.113 | 0.103 |
| R(sigma) | 0.1061 | 0.0976 | 0.0976 | 0.075 | 0.0575 | 0.3317 | 0.2984 | 0.223 | 0.1906 | 0.1699 |
| Goof | 1.206 | 1.121 | 1.123 | 1.324 | 1.318 | 1.242 | 1.211 | 1.22 | 1.121 | 1.204 |
| # parameters | 21 | 21 | 21 | 21 | 21 | 21 | 21 | 21 | 21 | 21 |
| R1 | 0.1149 | 0.119 | 0.1193 | 0.0913 | 0.0912 | 0.2068 | 0.2056 | 0.0948 | 0.0832 | 0.1095 |
| wR2 | 0.2172 | 0.2488 | 0.251 | 0.2026 | 0.2041 | 0.2325 | 0.2908 | 0.2139 | 0.2169 | 0.2221 |

Table 3.3: Positional and isotropic displacement parameters from 1 bar to 9.75(3) GPa.

| sample ID | | tad5x1 | tad5x1 | tad5x1 | tad5x4 | tad5x4 | tad5x6 | tad5x6 | tad5x6 | tad5x6 | tad5x6 |
|---|---|---|---|---|---|---|---|---|---|---|---|
| Pressure (GPa) | | 0.0001 | 1.952(6) | 4.279(8) | 5.111(5) | 6.408(14) | 7.818(15) | 8.207(9) | 9.03(1) | 9.345(11) | 9.75(3) |
| Al1 | $U_{iso}$ | 0.008(1) | 0.008(1) | 0.007(1) | 0.008(1) | 0.009(1) | 0.006(2) | 0.010(2) | 0.008(2) | 0.007(1) | 0.011(2) |
| T2 | $x$ | 0.1918(8) | 0.1933(7) | 0.1934(7) | 0.1963(8) | 0.1974(8) | 0.1965(13) | 0.2004(13) | 0.2004(12) | 0.2000(8) | 0.1981(12) |
| | $U_{iso}$ | 0.006(1) | 0.006(1) | 0.006(1) | 0.005(1) | 0.05(1) | 0.008(1) | 0.009(1) | 0.007(1) | 0.006(1) | 0.007(1) |
| Si | $z$ | 0.1201(7) | 0.1192(4) | 0.1192(4) | 0.1187(7) | 0.1188(7) | 0.1197(10) | 0.1200(11) | 0.1193(8) | 0.1186(7) | 0.1199(9) |
| | $U_{iso}$ | 0.007(1) | 0.006(1) | 0.007(1) | 0.006(1) | 0.006(1) | 0.010(1) | 0.011(1) | 0.009(1) | 0.007(1) | 0.008(1) |
| Ca | $z$ | 0.0986(8) | 0.0996(3) | 0.0996(3) | 0.0996(8) | 0.0998(8) | 0.0995(9) | 0.1002(9) | 0.0998(7) | 0.1006(5) | 0.1005(8) |
| | $U_{iso}$ | 0.013(1) | 0.013(1) | 0.013(1) | 0.012(1) | 0.012(1) | 0.014(1) | 0.015(1) | 0.011(1) | 0.013(1) | 0.010(1) |
| OH | $x$ | -0.2060(2) | -0.2081(8) | -0.2081(18) | -0.214(2) | -0.215(2) | -0.217(3) | -0.217(3) | -0.217(3) | -0.217(2) | -0.218(3) |
| | $y$ | 0.2985(17) | 0.3028(14) | 0.3028(14) | 0.3045(17) | 0.3045(18) | 0.307(1) | 0.304(2) | 0.307(2) | 0.306(2) | 0.309(2) |
| | $U_{iso}$ | 0.009(2) | 0.009(2) | 0.009(2) | 0.009(2) | 0.010(2) | 0.010(4) | 0.006(3) | 0.006(3) | 0.010(3) | 0.005(3) |
| O1 | $x$ | -0.7514(14) | -0.7506(12) | -0.7506(12) | -0.7537(14) | -0.7546(15) | -0.757(2) | -0.7551(18) | -0.7562(17) | -0.7534(14) | -0.757(2) |
| | $y$ | 0.1323(12) | 0.1348(11) | 0.1348(11) | 0.1355(13) | 0.1355(13) | 0.1346(19) | 0.1351(15) | 0.1341(16) | 0.1359(16) | 0.1362(17) |
| | $z$ | 0.0708(11) | 0.0717(8) | 0.0717(9) | 0.0712(12) | 0.0730(12) | 0.0724(15) | 0.0716(15) | 0.0713(14) | 0.0727(11) | 0.0722(15) |
| | $U_{iso}$ | 0.008(1) | 0.011(1) | 0.011(1) | 0.010(1) | 0.009(2) | 0.012(3) | 0.007(2) | 0.011(2) | 0.012(2) | 0.009(2) |
| O2 | $x$ | -0.3688(14) | -0.3709(13) | -0.3709(13) | -0.3732(15) | -0.3738(15) | -0.379(2) | -0.377(2) | -0.3783(18) | -0.3766(14) | -0.375(2) |
| | $y$ | 0.2148(12) | 0.2160(11) | 0.2160(11) | 0.2192(13) | 0.2199(13) | 0.223(2) | 0.227(2) | 0.224(2) | 0.2224(15) | 0.223(2) |
| | $z$ | 0.1714(13) | 0.1717(8) | 0.1717(8) | 0.1718(12) | 0.1704(13) | 0.1693(17) | 0.1683(16) | 0.1692(15) | 0.1718(13) | 0.1699(16) |
| | $U_{iso}$ | 0.011(1) | 0.012(1) | 0.011(1) | 0.012(2) | 0.012(2) | 0.015(3) | 0.021(3) | 0.017(2) | 0.011(2) | 0.014(3) |
| O3 | $z$ | 0.227(2) | 0.2302(14) | 0.2302(14) | 0.232(3) | 0.233(3) | 0.224(3) | 0.219(4) | 0.230(3) | 0.228(3) | 0.230(4) |
| | $U_{iso}$ | 0.018(2) | 0.019(2) | 0.018(2) | 0.019(2) | 0.020(3) | 0.025(5) | 0.027(5) | 0.038(5) | 0.044(5) | 0.053(7) |

Note: General fractional coordinates for atoms: Al1 (0 0 0), T2 ($x$ 0.75 0.25), Si1 (-0.5 0 $z$), Ca (0 0.5 $z$), OH ($x$ $y$ 0), O3 (0 0.5 $z$), O1 & O2 ($x$ $y$ $z$)

Table 3.4: Selected bond lengths and distances (Å).

| sample ID | | tad5x1 | tad5x1 | tad5x1 | tad5x4 | tad5x4 | tad5x6 | tad5x6 | tad5x6 | tad5x6 | tad5x6 |
|---|---|---|---|---|---|---|---|---|---|---|---|
| Pressure (GPa) | | 0.0001 | 1.952(6) | 4.279(8) | 5.111(5) | 6.408(14) | 7.818(15) | 8.207(9) | 9.03(1) | 9.345(11) | 9.75(3) |
| bond lengths | | | | | | | | | | | |
| Al1-O1 | (x4) | 1.888(16) | 1.895(12) | 1.884(12) | 1.866(16) | 1.882(16) | 1.86(2) | 1.85(2) | 1.842(18) | 1.869(15) | 1.85(2) |
| Al1-OH | (x2) | 1.895(9) | 1.907(8) | 1.894(8) | 1.912(9 | 1.905(10) | 1.913(14) | 1.900(12) | 1.906(12) | 1.900(11) | 1.914(13) |
| Poly Vol. | | 8.976 | 9.13 | 8.944 | 8.835 | 8.989 | 8.835 | 8.709 | 8.626 | 8.855 | 8.727 |
| | | | | | | | | | | | |
| T2-O2 | (x2) | 1.68(2) | 1.666(13) | 1.657(13) | 1.65(2) | 1.67(2) | 1.69(3) | 1.69(3) | 1.68(2) | 1.63(2) | 1.66(3) |
| T2-O3 | (x2) | 1.687(11) | 1.667(6) | 1.655(6) | 1.651(10) | 1.646(9) | 1.676(17) | 1.71(2) | 1.653(13) | 1.657(13) | 1.641(16) |
| Poly Vol. | | 2.367 | 2.304 | 2.26 | 2.243 | 2.257 | 2.282 | 2.325 | 2.268 | 2.197 | 2.218 |
| | | | | | | | | | | | |
| Si1-O2 | (x2) | 1.631(18) | 1.634(11) | 1.624(11) | 1.618(16) | 1.617(17) | 1.59(2) | 1.60(2) | 1.60(2) | 1.627(18) | 1.59(2) |
| Si1-O1 | (x2) | 1.648(15) | 1.620(11) | 1.610(11) | 1.636(17) | 1.599(15) | 1.61(2) | 1.62(2) | 1.612(17) | 1.585(14) | 1.612(19) |
| Poly Vol. | | 2.25 | 2.194 | 2.155 | 2.197 | 2.113 | 2.118 | 2.106 | 2.113 | 2.106 | 2.106 |
| | | | | | | | | | | | |
| Ca-OH | (x2) | 2.336(13) | 2.329(7) | 2.317(7) | 2.320(13) | 2.317(13) | 2.305(15) | 2.318(15) | 2.304(12) | 2.314(10) | 2.305(14) |
| Ca-O1 | (x2) | 2.379(9) | 2.353(7) | 2.337(7) | 2.324(9) | 2.307(9) | 2.298(12) | 2.304(11) | 2.299(10) | 2.292(9) | 2.280(11) |
| Ca-O2 | (x2) | 2.680(15) | 2.656(10) | 2.638(10) | 2.630(14) | 2.607(14) | 2.597(18) | 2.562(18) | 2.578(16) | 2.593(13) | 2.568(18) |
| Ca-O3 | | 2.38(4) | 2.40(3) | 2.39(3) | 2.42(4) | 2.43(4) | 2.26(5) | 2.17(6) | 2.36(5) | 2.31(5) | 2.35(7) |
| | | | | | | | | | | | |
| distances | | | | | | | | | | | |
| Ca…Ca | | 3.65(3) | 3.67(2) | 3.65(2) | 3.65(3) | 3.64(3) | 3.62(4) | 3.65(4) | 3.63(3) | 3.65(2) | 3.65(3) |
| O3…O3 | | 8.4(1) | 8.47(6) | 8.43(6) | 8.5(1) | 8.5(1) | 8.1(2) | 8.0(2) | 8.3(2) | 8.3(2) | 8.3(2) |
| OH…OH | | 2.92(2) | 2.88(2) | 2.86(2) | 2.87(2) | 2.86(3) | 2.85(3) | 2.86(3) | 2.84(3) | 2.84(3) | 2.82(3) |
| O1…O1 | | 5.35(3) | 5.30(2) | 5.27(2) | 5.25(3) | 5.27(3) | 5.26(4) | 5.23(4) | 5.23(3) | 5.22(3) | 5.22(4) |
| | | | | | | | | | | | |
| ellipticity ratio | | | | | | | | | | | |
| O1…O1/O3…O3 | | 0.637 | 0.626 | 0.625 | 0.618 | 0.620 | 0.649 | 0.654 | 0.630 | 0.629 | 0.629 |
| OH…OH/O3…O3 | | 0.348 | 0.340 | 0.339 | 0.338 | 0.336 | 0.352 | 0.358 | 0.342 | 0.342 | 0.340 |

Table 3.5: Selected bond angles (º) and distortion parameters.

| sample ID | | tad5x1 | tad5x1 | tad5x1 | tad5x4 | tad5x4 | tad5x6 | tad5x6 | tad5x6 | tad5x6 | tad5x6 |
|---|---|---|---|---|---|---|---|---|---|---|---|
| Pressure (GPa) | | 0.0001 | 1.952(6) | 4.279(8) | 5.111(5) | 6.408(14) | 7.818(15) | 8.207(9) | 9.03(1) | 9.345(11) | 9.75(3) |
| **Al1** | | | | | | | | | | | |
| OH-Al1-O1 | (x4) | 91.5(3) | 91.9(3) | 91.9(3) | 91.9(3) | 91.9(3) | 89.7(12) | 89.3(12) | 89.5(11) | 89.9(9) | 89.9(13) |
| OH-Al1-O1 | (x4) | 88.5(3) | 88.1(3) | 88.1(3) | 88.1(3) | 88.1(3) | 90.3(12) | 90.7(12) | 90.5(11) | 90.1(9) | 90.1(13) |
| O1-Al1-O1 | (x2) | 87.8(10) | 88.3(7) | 88.5(7) | 88.5(10) | 89.8(10) | 88.1(4) | 88.3(4) | 88.3(4) | 88.3(3) | 87.9(4) |
| O1-Al1-O1 | (x2) | 92.2(10) | 91.7(7) | 91.5(7) | 91.5(10) | 90.2(10) | 91.9(4) | 91.7(4) | 91.7(4) | 91.7(3) | 92.1(4) |
| OH-Al1-OH | | 180.0 | 180.0 | 180.0 | 180.0 | 180.0 | 180.0 | 180.0 | 180.0 | 180.0 | 180.0 |
| O1-Al1-O1 | | 180.0 | 180.0 | 180.0 | 180.0 | 180.0 | 180.0 | 180.0 | 180.0 | 180.0 | 180.0 |
| AV | | 3.36 | 3.64 | 3.67 | 3.66 | 2.47 | 2.56 | 2.14 | 2.53 | 2.28 | 3.17 |
| QE | | 1.00 | 1.00 | 1.00 | 1.00 | 1.00 | 1.00 | 1.00 | 1.00 | 1.00 | 1.00 |
| | | | | | | | | | | | |
| **T2** | | | | | | | | | | | |
| O3-T2-O3 | | 116.5(5) | 115.6(3) | 115.7(3) | 114.6(5) | 114.3(5) | 116.2(8) | 116.2(9) | 114.0(6) | 114.4(6) | 114.5(8) |
| O3-T2-O2 | (x2) | 112.2(13) | 111.0(8) | 111.0(8) | 110.6(14) | 110.4(14) | 115.9(17) | 118.5(19) | 112.9(16) | 113.7(16) | 112(2) |
| O3-T2-O2 | (x2) | 97.8(15) | 99.3(8) | 99.2(8) | 100.0(15) | 99.9(16) | 94.5(18) | 91(2) | 97.4(18) | 97.1(17) | 98(2) |
| O2-T2-O2 | | 121.6(9) | 121.4(6) | 121.6(6) | 121.7(9) | 122.7(9) | 121.7(12) | 123.8(12) | 123.1(11) | 122.0(9) | 123.0(12) |
| AV | | 93.93 | 78.28 | 80.13 | 72.55 | 75.26 | 121.78 | 211.19 | 109.29 | 103.02 | 99.06 |
| QE | | 1.02 | 1.02 | 1.02 | 1.02 | 1.02 | 1.03 | 1.05 | 1.03 | 1.03 | 1.02 |
| | | | | | | | | | | | |
| **Si1** | | | | | | | | | | | |
| O1-Si1-O1 | | 112.7(15) | 114.8(11) | 114.6(11) | 115.1(17) | 117.0(16) | 115(2) | 114(2) | 114.5(18) | 116.6(15) | 115(2) |
| O1-Si1-O2 | (x2) | 112.2(5) | 112.8(4) | 112.9(4) | 113.3(5) | 112.6(5) | 113.1(7) | 113.2(7) | 113.3(6) | 113.7(5) | 112.9(7) |
| O1-Si1-O2 | (x2) | 105.5(5) | 104.4(4) | 104.5(4) | 104.0(6) | 103.0(6) | 102.2(8) | 101.8(7) | 102.6(7) | 102.9(6) | 102.9(7) |
| O2-Si1-O2 | | 108.8(16) | 107.6(10) | 107.4(10) | 107.2(15) | 108.7(16) | 111(2) | 113(2) | 110.9(18) | 107.1(15) | 110.5(19) |
| AV | | 11.51 | 21.16 | 20.81 | 24.59 | 32.14 | 30.42 | 36.32 | 30.90 | 36.44 | 28.49 |
| QE | | 1.00 | 1.01 | 1.01 | 1.01 | 1.01 | 1.01 | 1.01 | 1.01 | 1.01 | 1.01 |
| | | | | | | | | | | | |
| **Ca** | | | | | | | | | | | |
| OH-Ca-OH | | 77.3(6) | 76.2(4) | 76.1(4) | 76.5(6) | 76.3(6) | 76.4(8) | 76.2(7) | 76.1(6) | 75.8(5) | 75.3(7) |
| O1-Ca-OH | (x2) | 68.1(5) | 68.8(4) | 68.7(4) | 68.9(6) | 69.4(6) | 69.5(7) | 68.9(6) | 69.1(6) | 69.5(5) | 69.6(7) |
| O1-Ca-OH | (x2) | 92.0(6) | 91.1(4) | 91.1(4) | 90.4(6) | 91.0(6) | 90.7(8) | 90.2(8) | 90.2(6) | 90.1(5) | 89.6(8) |
| O3-Ca-OH | (x2) | 141.3(3) | 141.88(18) | 141.96(18) | 141.8(3) | 141.8(3) | 141.8(4) | 141.9(4) | 141.9(3) | 142.1(3) | 142.3(3) |
| O2-Ca-OH | (x2) | 158.3(7) | 157.6(4) | 157.6(4) | 158.0(7) | 157.4(7) | 157.1(9) | 156.6(8) | 157.0(7) | 157.4(6) | 156.8(8) |
| O2-Ca-OH | | 81.7(5) | 82.0(3) | 82.1(3) | 82.0(5) | 81.6(5) | 81.3(7) | 81.0(6) | 81.4(6) | 82.2(5) | 81.9(6) |
| O1-Ca-O1 | | 155.0(12) | 154.8(8) | 154.8(8) | 154.1(13) | 155.6(13) | 155.2(16) | 153.9(16) | 154.0(13) | 154.5(11) | 154.0(16) |
| O3-Ca-O1 | (x2) | 102.5(6) | 102.6(4) | 102.6(4) | 102.9(7) | 102.2(6) | 102.4(8) | 103.1(8) | 103.0(7) | 102.8(5) | 103.0(8) |
| O2-Ca-O1 | (x2) | 107.2(3) | 106.9(3) | 106.9(3) | 106.9(4) | 106.5(4) | 106.2(5) | 106.1(4) | 106.4(4) | 106.2(3) | 106.6(4) |
| O2-Ca-O1 | (x2) | 85.5(4) | 85.8(3) | 85.8(3) | 86.2(4) | 85.7(4) | 86.0(5) | 86.7(5) | 86.5(5) | 86.6(4) | 86.3(5) |
| O2-Ca-O3 | (x2) | 59.8(5) | 60.1(3) | 60.0(3) | 59.9(5) | 60.3(5) | 60.7(7) | 61.1(7) | 60.7(6) | 60.1(5) | 60.6(7) |
| O2-Ca-O2 | | 119.6(11) | 120.1(6) | 120.0(6) | 119.8(10) | 120.7(10) | 121.4(14) | 122.2(13) | 121.4(11) | 120.1(10) | 121.2(13) |
| | | | | | | | | | | | |
| T2-O3-T2 | | 151(3) | 154.7(17) | 154.6(17) | 157(3) | 158(3) | 147(4) | 142(4) | 154(4) | 152(4) | 154(5) |
| T2-O2-Si1 | | 140.2(8) | 140.2(6) | 140.3(6) | 139.4(7) | 138.5(8) | 136.3(11) | 134.6(11) | 136.1(10) | 138.4(8) | 137.0(10) |
| Al1-O1-Si1 | | 130.2(5) | 128.9(4) | 128.9(4) | 128.6(6) | 128.2(6) | 128.9(8) | 129.1(7) | 129.2(7) | 128.2(6) | 128.6(7) |
| | | | | | | | | | | | |
| Ca-O3-T2 | | 104.3(15) | 102.6(9) | 102.7(9) | 101.4(16) | 101.1(16) | 106.6(19) | 109(2) | 103.0(18) | 104.1(18) | 103(2) |
| Ca-OH-Al1 | | 101.8(3) | 101.2(3) | 101.2(3) | 100.3(3) | 100.2(3) | 99.8(5) | 99.9(4) | 99.7(4) | 99.7(3) | 99.3(4) |
| Ca-OH-Ca | | 102.7(6) | 103.8(4) | 103.9(4) | 103.5(6) | 103.7(6) | 103.6(8) | 103.8(7) | 103.9(6) | 104.2(5) | 104.7(7) |
| Ca-O2-Si1 | | 111.5(12) | 111.0(7) | 110.8(7) | 110.3(11) | 111.3(11) | 112.1(15) | 113.4(14) | 112.1(13) | 110.0(11) | 112.1(14) |
| Ca-O2-T2 | | 93.3(4) | 93.0(3) | 93.2(3) | 93.6(4) | 93.7(4) | 93.2(5) | 94.0(6) | 93.9(5) | 93.8(4) | 93.8(5) |
| Ca-O1-Si1 | | 126.5(11) | 127.7(8) | 127.6(8) | 127.3(12) | 128.6(11) | 127.5(14) | 126.6(15) | 126.6(12) | 128.1(10) | 127.0(14) |
| Ca-O1-Al1 | | 100.4(5) | 100.7(3) | 100.8(3) | 101.5(5) | 101.3(5) | 101.7(6) | 101.8(6) | 101.9(5) | 101.5(4) | 102.1(6) |

### 3.4 Results and Discussion

Values of the unit-cell parameters of prehnite at 1 bar, $a$ = 4.6248(4) Å, $b$=5.4825(4) Å, and $c$=18.476(1) Å, are in reasonable agreement with previous studies (Papike & Zoltai, 1967; Peng *et al.*, 1959). The variation of $V/V_0$ with pressure from the three different crystals of prehnite that were measured are consistent with one another (Figure 3.3), with a smooth variation of decreasing volume with increasing pressure up to at least 8.68(1) GPa. The two highest pressure data points, at 9.345(11) GPa and 9.75(3) GPa, fall significantly below the extrapolation of an EoS calculated using the PV data up to and including that at 8.68(1) GPa. The data point at 9.03(1) GPa lies close to the EoS from lower pressures. These deviations cannot be fit by a 4$^{th}$-order EoS with softening as for some feldspars (Benusa *et al.*, 2005; Nestola *et al.*, 2009).

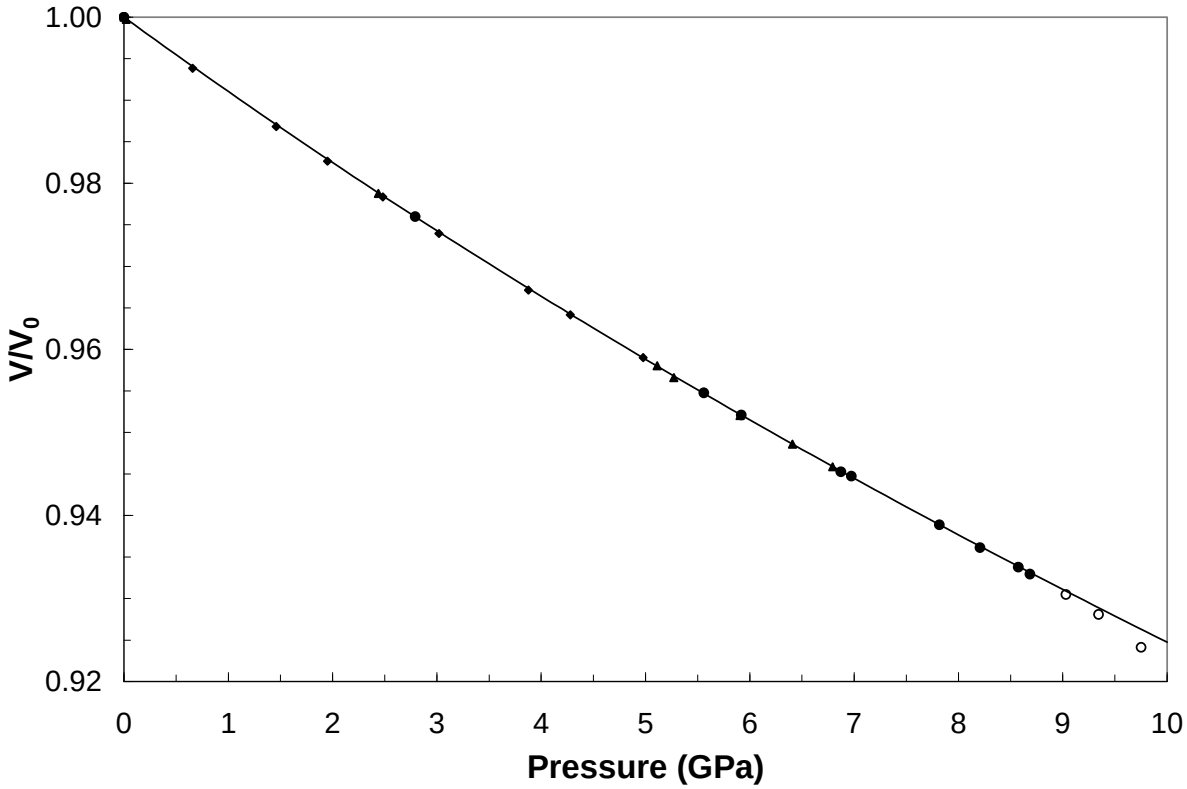


Figure 3.3: Variation of the unit-cell volume with pressure for each of the 3 prehnite crystals between 1 bar and 9.75(3) GPa. The e.s.d.'s are slightly smaller than the size of the symbols shown. (♦) represent tad5x1, (▲) represent tad5x4, (●) represent tad5x6, and the solid line is the EoS fit to data at pressures less than 8.7 GPa. (○) represents data from tad5x6 above the phase transition.

These deviations from the EoS are not due to the onset of non-hydrostatic stresses in the experiment because the methanol:ethanol pressure medium remains hydrostatic to over 9.8 GPa (Angel *et al.*, 2007). This is confirmed by the fact that the reflections of both the quartz and the sample remain as sharp as at lower pressures, which also confirms that the sample did not bridge the diamond anvils. No attempt was made to measure the sample at pressures higher than 9.8 GPa due to limitations of the pressure medium. The sample was measured on decompression to determine the reversibility of the transition. Further, the orientation of the sample with (001) lying parallel to the culet face of the diamond anvils would mean that were non-hydrostatic stresses present, they would lead to an apparent softening of the *c*-axis, and stiffening of the *a*- and *b*- axes (Zhao & Angel, 2009, in prep). However, the opposite is observed (Figure 3.4); the *b*-axis is shows significant softening above 9 GPa, while the *c*-axis becomes slightly stiffer. Further, the pressure evolution of the Raman and infra-red spectra show significant changes between 8.4 and 9.4 GPa, especially in the range of 3400-3550 $cm^{-1}$ which is associated with O-H vibrations (Chapter 4). It therefore appears that prehnite undergoes a phase transition at approximately 9 GPa, that is either very-weakly first order, or continuous in character. Decompression of the diamond-anvil cell from 9.75(3) GPa to 8.68(1) GPa and then to 6.873(9) GPa resulted in unit-cell parameters that were consistent with those measured upon compression, and no peak broadening occurred. This indicates that the transition is fully reversible and, if hysteresis occurs, the loop is less than 0.35 GPa.

Figure 3.5 shows the compression data plotted as normalized pressure, *F* (Birch, 1978), against the Eulerian strain measure, *f* (*e.g.* Angel, 2000). *F-f* plots provide a visual indication of whether higher order terms such as $K_0$'and $K_0$'' are significant in the EoS. If all data points lie on a horizontal line of constant *F*, then $K_0' = 4$ and the data can be fit with a second-order Birch-Murnaghan EoS. If the data lie on a straight line that is not horizontal, the data will be adequately described by a third-order truncation of the Birch-Murnaghan EoS with the slope of each line equal to $3K_{T0}(K' - 4)/2$. A positive slope indicates that $K' > 4$ and a negative slope indicates that $K' < 4$. As shown in Figure 3.5, the data up to 8.7 GPa lie, within the uncertainties, on a horizontal line. A second-order Birch-Murnaghan equation-of-state was fitted to all 27 P-V data between 1 bar and 8.68(1) GPa with data for each crystal scaled by its own $V_0$. The bulk modulus is $K_{0T}$ = 109.29(18) GPa, and $K_0' = 4$ with $\chi_w^2 = 0.32$. A third-order Birch-Murnaghan equation-of-state

fitted to P-V data between 1 bar and 8.68(1) GPa yields K' = 4.11(18) with the same $\chi_w^2 = 0.32$, confirming that the EoS of prehnite is adequately described by the 2nd-order fit.

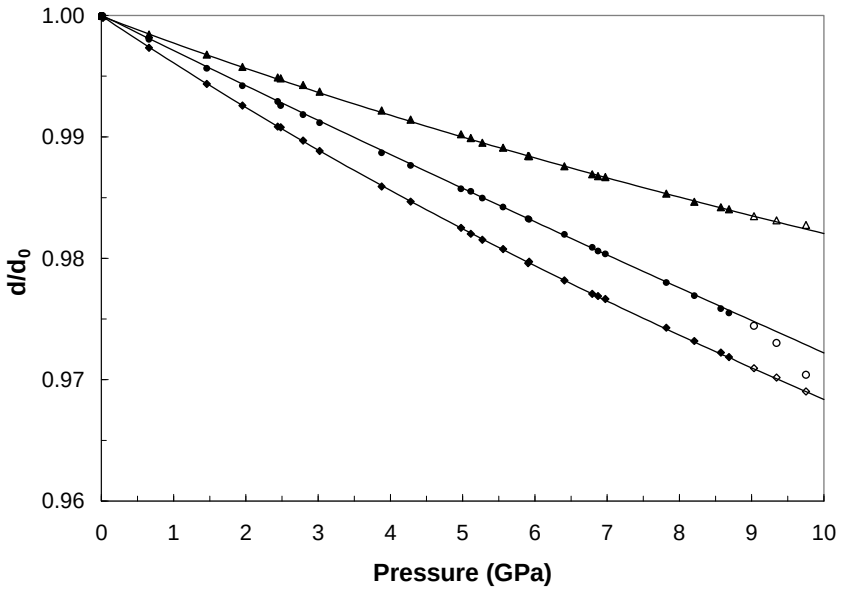


Figure 3.4: Variation of the unit-cell parameters as a function of pressure. (♦) represent a-axis, (●) represent b-axis, (▲) represent c-axis. Open symbols represent data above the phase transition. The e.s.d.'s are slightly smaller than the size of the symbols shown. The solid lines are the equations of state fit to data at pressures less than 8.7 GPa.

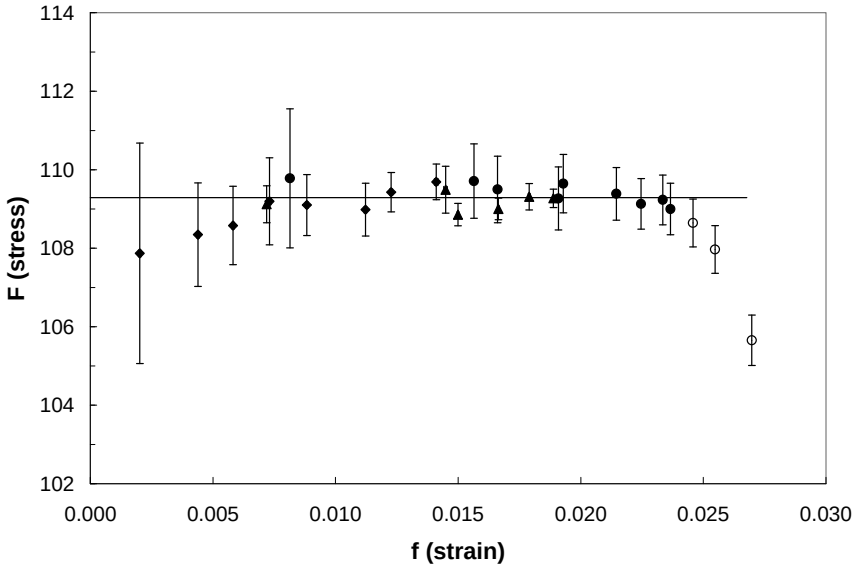


Figure 3.5: Plot of the volume finite strain versus the normalized stress for prehnite calculated from the P-V data. Symbols as for figure 3.3. Error bars include the contributions from uncertainties in pressure and volume measurements (Angel, 2000). The f and F values for the experimental data have been calculated with the $V_o$ from the fitted EoS. The line is the 2nd-order Birch-Murnaghan EoS fit to the P-V data.

The axial compressibilities, $a/a_0$, $b/b_0$, and $c/c_0$, provide further insight into the high-pressure behavior of prehnite and are plotted as a function of pressure in Figure 3.4. The compressibility along the unit cell directions is notably anisotropic with *a* being most compressible, *b* intermediate, and *c* least compressible. Since the variation of the unit cell parameters display significant curvature with pressure, I determined the axial moduli by fitting a parameterized form of the third-order Birch-Murnaghan equation to the cube of the unit cell edges (Angel, 2000). Because of the phase transition at P ~ 9 GPa, I excluded the three highest pressure data points in the analyses and obtained values of $K_{a0}$= 83.5(7) GPa, $K_{b0}$= 113(1) GPa, and $K_{c0}$ = 146(3) GPa with $K'_{a0}$=4.5(3), $K'_{b0}$=1.3(3), and $K'_{c0}$=8.8(8) (Figure 3.6). These fitted EoS are compared with the data in Figure 3.4. Between 1 bar and 8.7 GPa, *a* is almost twice as compressible as *c* and $K_{b0}$ is approximately 30 GPa greater than $K_{a0}$ and 33 GPa less than $K_{c0}$. In addition, *c* has the highest $K'_0$ value and *b* the lowest; the latter may be related to the subsequent softening in this direction above 9 GPa.

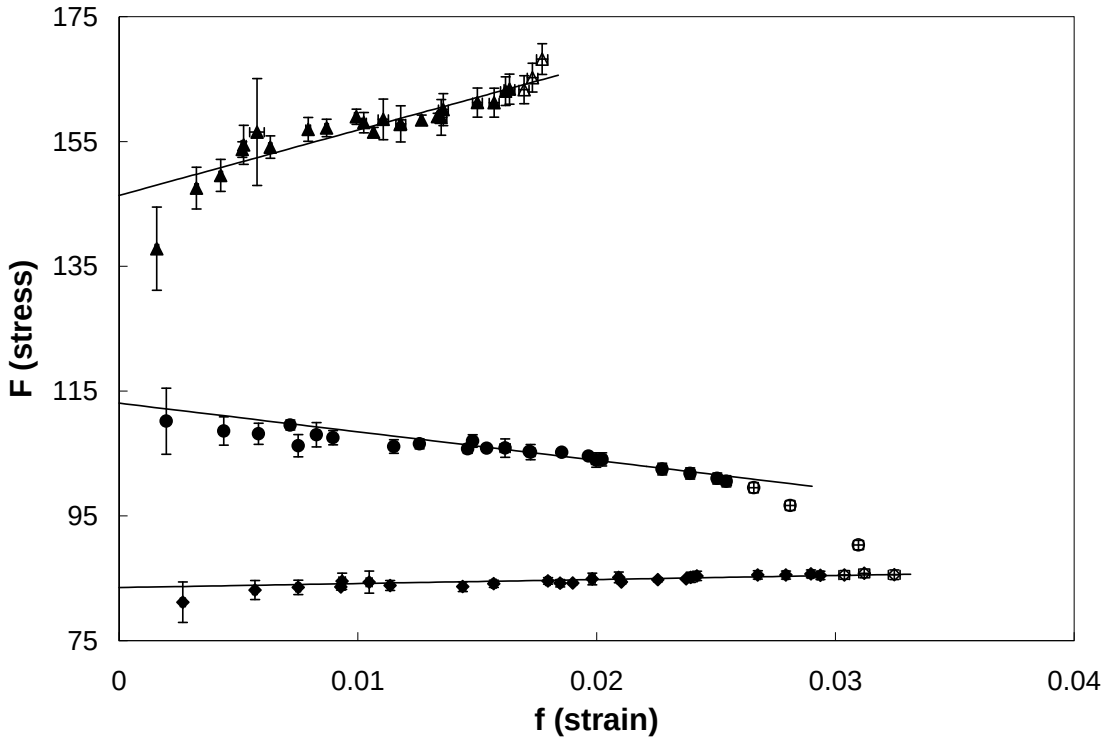


Figure 3.6: Plot of the cell-parameter finite strain versus the normalized stress for prehnite calculated from the P-$a^3$, P-$b^3$, and P-$c^3$ data. Symbols as for figure 3.4. Error bars include contributions from uncertainties in pressure and cell parameter measurements (Angel, 2000). The lines are the 3rd-order Birch-Murnaghan EoS fit to the P-$a^3$, P-$b^3$, or P-$c^3$ data.

*3.4.1 Structural changes in prehnite with pressure*

The structure refinements of prehnite crystals loaded in the DACs at 1 bar (without a pressure-transmitting fluid) are in good agreement with previous refinements completed in air (Papike & Zoltai 1967; Chapter 2). However, because of the limited access to reciprocal space in the DAC, the esd's on the refined parameters tend to be larger. In addition, the positional parameters of the H atom could not be refined and it was therefore omitted from the refinements. As noted above, all refinements were performed in space group *Pncm*, which represents an average structure. Uncertainties, especially on oxygen positions, are therefore larger than would normally be expected due to this averaging, the isotropic displacement parameters of the oxygen atoms are greater than for a normal structure, and care must be taken in interpreting bond lengths and angles between these "averaged" atom positions.

As shown in Figure 3.1, prehnite is a complex layered structure in which double-sheets of corner-sharing $SiO_4$ and $(Al,Si)O_4$ tetrahedra alternate with single sheets of $AlO_6$ octahedra stacked perpendicular to [001]. H atoms are bonded to apical oxygen atoms (OH) of the $AlO_6$ octahedra (Chapter 2) and Ca atoms occupy positions between the layers. The $SiO_4$ tetrahedron is distorted, with O-Si1-O angles ranging from 105º to 113º at 1 bar (Table 3.5). The angular variance (AV), a measure of the angular distortion of the tetrahedron (Robinson *et al.*, 1971), is 11.5. The average Si-O bond length is 1.639(12) Å and the tetrahedral quadratic elongation (QE), a measure of the deviation of the bond lengths from a mean value (Robinson *et al.*, 1971), is 1.003. The $T2O_4$ tetrahedron, with mixed occupancy of Al and Si, also shows large angular distortion with O-T2-O angles ranging from 98º to 122º at 1 bar with an AV of 93.9. The symmetrically-distinct T2-O2 and T2-O3 of the $T2O_4$ are equal within ±1 esd, with an average T2-O of 1.6840(8) Å and QE=1.024. The $AlO_6$ is close to being a regular octahedron with O-Al1-O angles ranging from 87.8$^o$ to 92.2$^o$ with an overall octahedral AV of 3.4. There are four symmetrically-equivalent Al1-O1 bond lengths of 1.888(16) Å and two slighter longer Al1-OH bond lengths of 1.895(9) Å where OH is bonded to hydrogen. The mean octahedral QE is 1.0009. The Ca site is irregular with Ca surrounded by seven O atoms. The Ca-O distances range from 2.336(13) Å (Ca-OH) to 2.680(15) Å (Ca-O2).

No significant change in the bond lengths of the $T2O_4$ or $AlO_6$ is observed up to 8.3 GPa (Table 3.4). The data suggest a marginal, but barely significant decrease in the bond lengths of the $SiO_4$ tetrahedron with Si1-O1 decreasing from 1.648(15) Å to 1.62(2) Å and Si1-O2 decreasing from 1.631(18) Å to 1.60(2) Å between 1 bar and 8.207(9) GPa. Although the bond lengths do not change, there appear to be significant distortions of both the $SiO_4$ and $T2O_4$ tetrahedra at higher pressures, as indicated by significant changes in the O-T-O bond angles and a corresponding increase in the angular variances. These changes correspond to a relative rotation of opposite edges of the tetrahedra, or shearing deformation (Figure 3.7).

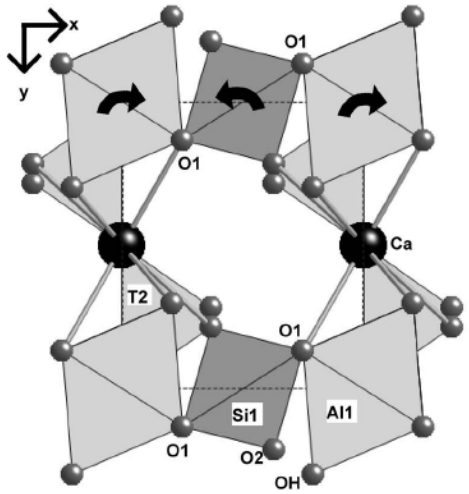


Figure 3.7: View of prehnite structure as viewed along [001]. Arrows represent direction of shearing of the structure with increasing pressure, which is drastically reduced at the phase transition.

This distortion means that the tetrahedra are not behaving as rigid units. Nonetheless, the corner-sharing linkages between the tetrahedra, Si1-O2-T2 and T2-O3-T2, and between the $AlO_6$ octahedron and $SiO_4$, Al1-O1-Si1, may provide insights into the compression mechanisms operative in prehnite. Unfortunately, due to the average nature of the structure, and the orientation of crystal in the DAC, the uncertainties in the *z*-coordinates of the O3 and consequently the T2-O3-T2 angles are large. However, it appears that there is a significant decrease in this angle at higher pressures, so that it reaches 142(4)$^o$ at 8.207(9) GPa, compared to 151(3)$^o$ at room pressure. There is no significant change in the Al1-O1-Si1 angle over the pressure range studied and all are within 129$^o$ ± 0.7$^o$. The Si1-O2-T2 angle, however, shows a decrease from 140.2(8)$^o$ at room pressure to 134.6(11)$^o$ at 8.207(9) GPa, which represents a

flexing of the framework so as to push the O2 towards the Ca atom. As a consequence the Ca-O2 bond, which is the longest Ca-O bond at room pressure, shows the greatest decrease in length, from 2.680(15) Å to 2.562(18) Å between room pressure and 8.207(9) GPa. The shorter Ca-O1 bonds decrease by about 0.8 Å over the same pressure range.

The overall picture, therefore, is one of fairly small and uniform compression of the polyhedral framework of prehnite, with most of the linear compression of 1.5 – 3% (Figure 3.4) being accounted for by small changes in the O-T-O and the T-O-T angles. This can be understood in terms of the topology of the polyhedral framework, shown in Figure 3.1. First, the 4-ring formed by two Al1 octahedra and Si1 tetrahedra cannot undergo shear, because it is constrained by the mirror symmetry of the structure. The only significant degree of freedom in the framework is therefore the spiral of Si1 and T2 tetrahedra whose axis is parallel to [010] (Figure 3.1). Compression of this spiral is accommodated by the decrease in the Si1-O2-T2 angle and the distortion of the tetrahedra.

It is therefore the Ca atom within the cavities in the polyhedral framework that results in the significant stiffening of the c-axis of prehnite (Figure 3.4). Adjacent Ca atoms along [001] are both bonded to the same two OH oxygen atoms, which thus form a common edge to the adjacent $CaO_7$ coordination polyhedra (Figure 3.2). The short Ca-Ca distance across this edge shows absolutely no decrease with pressure, presumably due to mutual repulsion. Further, the Ca-O3 bonds that are in line with the Ca-Ca vector are short at room pressure (2.38(4) Å). The O3-Ca-(OH)2-Ca-O3 link can therefore be seen as a strut that stiffens the structure against compression along the [001] direction. If we consider the Ca-containing channel (Figure 3.2) as a whole, it has a pronounced ellipticity, elongated along [001], which is maintained with increasing pressure (Table 3.4). Therefore, the relative stiffness of the *c*-axis relative to the *b*-axis is also consistent with the general principle postulated by Gatta (2008) for open-framework silicates, that open tetrahedral framework structures tend to accommodate the effect of pressure by *usually* increasing (or maintaining) the ellipticity of the channel (or ring) systems. The smaller anisotropy between the *a*- and *b*-axes can be attributed to the cooperative small rotations of the octahedron and the shearing of the tetrahedra (Figure 3.6), which contribute to the relative softening of the *a*-axis and stiffening of the *b*-axis.

*3.4.2 Changes in prehnite above 8.7 GPa*

At 9 GPa and above prehnite becomes more compressible than the extrapolated equation of state (Figure 3.3), as a result of the softening of the *b*-axis which is only partially compensated by a stiffening of the *c*-axis (Figure 3.4). A careful survey of reciprocal space with a CCD camera did not reveal any additional reflections, nor the disappearance of reflections, while careful unit-cell parameter determinations show that the unit-cell metric retains orthorhombic symmetry. Structure refinements in *Pncm* space group were of at least the same quality as at lower pressures (Table 3.2), so it can be concluded that at least the average structure of prehnite is retained at pressures in excess of 9 GPa.

A comparison of the structures refined to the data from 9.03(1) GPa and above with the lower-pressure data, show that the unit-cell parameter changes are accompanied by a significant change in the environment of the O3 atom. There is a decrease in the shear of the T2 tetrahedron (as measured by the angle variance), which is mostly due to the O3-T2-O2 angle recovering from 91(2)º to 98(2)º, the same value as at room pressure (Table 3.5). There is an expansion of the Ca-O3 distance from 2.17(6) Å back to 2.35(7) Å (Table 3.4), not that much shorter than its room-pressure value, and the T2-O3-T2 angle recovers from 142(4)º at 8.2 GPa to 154(4)º at 9.032(10) GPa, again similar to the value found at ambient pressure. This suggests that the driving force for the structural changes above 9 GPa is the reduction of the shear of the T2 tetrahedron, while the Si tetrahedron, the Al octahedron and the remainder of the Ca environment all remain essentially unchanged. One must caution, however, that it is entirely possible that further changes in the structure are obscured by the implicit averaging of our refinement model with *Pncm* symmetry, whereas the true symmetry at lower pressures is *P2cm*, due to the ordering of Al and Si on the T2 site.

## 3.5 Conclusions

This study is the first undertaken to determine the behavior of prehnite at high pressure. The bulk modulus of prehnite, 109.29(18) GPa, is 20% stiffer than previously estimated (83.5 GPa; Holland & Powell, 1998). In comparing the prehnite bulk modulus to moduli of other structures,

it resembles the bulk moduli of various pyroxenes (e.g. pigeonite: 102(2) GPa, Nestola *et al.*, 2004 and Ca-orthoenstatite: 110(1) GPa, Nestola *et al.*, 2006). In prehnite, the T2 tetrahedra are corner-sharing with each other, connected in a chain running parallel to the *b*-axis, similar to the tetrahedral chains of low pigeonite (as described in Putnis, 1992), with a degree of tilt to them. However, instead of connecting to octahedra, as in the pigeonite structure, they are connected to the rest of the prehnite structure via the Si1 tetrahedron.

Chemically similar calcium-aluminum silicates exhibit a wide range of bulk moduli. Minerals such as the sorosilicates lawsonite ($CaAl_2Si_2O_7(OH)_2{\cdot}H_2O$) and clinozoisite, ($Ca_2Al_3O(SiO_4)(Si_2O_7)(OH)$) have bulk moduli slightly higher than prehnite (lawsonite: 122.1(4) GPa, Boffa Ballaran & Angel, 2003; clinozoisite: 127(5) GPa, Comodi & Zanazzi, 1997). Within the feldspars, extrapolation of data *I-1* plagioclase to pure anorthite $CaAl_2Si_2O8$, gives a bulk modulus of 82.5 GPa (Angel, 2004b). The most recent data on *P-1* plagioclase for $An_{96}Ab_4$ has a bulk modulus of 83.8 (11) GPa (Johnson, 2007). The zeolite scolecite, $Ca_8Al_{16}Si_{24}O_{80}{\cdot}24H_2O$, has a much lower bulk modulus of 54.6(6) GPa (Gatta, 2005). Other minerals with frameworks comprised of both octahedra and tetrahedra, such as those in the titanite group, have bulk moduli typically slightly higher than that of prehnite. The titanites of $CaTiSiO_5$, $CaSi_2O_5$ have bulk moduli of 123(2) GPa and 178.2(7) GPa, respectively (Angel *et al.*, 1999). Malayaite, also in the titanite family, $CaSnSiO_5$, has a bulk modulus of 121.6(7) GPa (Rath *et al.*, 2003). Vesuvianite, structurally similar to prehnite by having a combination of tetrahedra and octahedra and Ca-cavities parallel to the [001], has a bulk modulus of 126(2) GPa (Tribaudino & Prencipe, 2001).

The structure of prehnite is often classified as a layer-silicate. The bulk moduli of micas are lower than that of prehnite, by about half (data quoted in Holland & Powell, 1998), with moduli of about 50 GPa. Micas, made up of sheets of octahedra and tetrahedra, are connected loosely with either van der Waals forces or a cation. It is the presence of these weak bonds that contribute to the softness of micas through the high compressibility of the c-axis. Prehnite is termed a "sheet silicate" because the octahedra and tetrahedra form separate layers parallel to (001) (Figure 3.1). However, this is misleading because were the analogy with micas to hold true, one would expect the *c*-axis of prehnite to be the softest direction in the structure. Instead, our experimental data show the *c*-axis to be the least compressible direction, as a result of the

interaction of the *combined* octahedral-tetrahedral framework with the extra-framework Ca atoms.

### 3.6 References


Akasaka, M., Hashimoto, H., Makino, K., Hino, R. (2003): $^{57}$Fe Mossbauer and X-ray Rietveld studies of ferrian prehnite from Kouragahana, Shimane Peninsula, Japan. *Journal of Mineralogical and Petrological Sciences*, 98, 31-40.

Angel, R.J. (2000): Equations of state. "High-Temperature and High-Pressure Crystal Chemistry", *in* R.M. Hazen, R.T. Downs, eds. *Reviews in Mineralogy & Geochemistry* 41, Mineralogical Society of America, Chantilly, Virginia, p. 35-60.

-. (2003): Automated profile analysis for single-crystal diffraction data. *Journal of Applied Crystallography*, 36, 295-300.

-. (2004a): Absorption corrections for diamond-anvil cells implemented in the software package Absorb 6.0. *Journal of Applied Crystallography*, 37, 486-492.

-. (2004b): Equations of state of plagioclase feldspars. *Contributions to Mineralogy & Petrology*, 146, 506-512.

Angel, R.J., Allan, D.R., Miletich, R., Finger, L.W. (1997): The use of quartz as an internal pressure standard in high-pressure crystallography *Journal of Applied Crystallography*, 30, 461-466.

Angel, R.J., Bujak, M., Zhao, J., Gatta, G.D., Jacobsen, S.D. (2007): Effective hydrostatic limits of pressure media for high-pressure crystallographic studies. *Journal of Applied Crystallography*, 40, 26-32.

Angel, R.J., Kunz, M., Miletich, R., Woodland, A.B., Koch, M., Knoche, R.L. (1999): Effect of isovalent Si,Ti substitution on the bulk moduli of $Ca(Ti_{1-x}Si_x)SiO_5$ titanites. *American Mineralogist*, 84, 282-287.

Artioli, G., Quartieri, S., Deriu, A. (1995): Spectroscopic data on coexisting prehnite-pumpellyite and epidote-pumpellyite. *Canadian Mineralogist*, 33, 67-75.

Aumento, F. (1968): The space group of prehnite. *Canadian Mineralogist*, 9, 485-492.

Balić-Žunić, T., Šćavničar, S., Molin, G. (1990): Crystal structure of prehnite from Komiža. *European Journal of Mineralogy*, 2, 731-734.

Benusa, M.D., Angel, R.J., Ross, N.L. (2005): Compression of albite, $NaAlSi_3O_8$. *American Mineralogist*, 90, 1115-1120.

Birch, F. (1978): Finite strain isotherm and velocities for single-crystal and polycrystalline NaCl at high pressures and 300 degrees K. *Journal of Geophysical Research*, 83, 1257-1268.

Blessing, R.H. (1987): Data reduction and error analysis for accurate single crystal diffraction intensities. *Crystallography Reviews*, 1, 3-58.

Boffa Ballaran, T. & Angel, R.J. (2003): Equation of state and high-pressure phase transitions in lawsonite. *European Journal of Mineralogy*, 15, 241-246.

Comodi, P. & Zanazzi, P.F. (1997): The pressure behavior clinozoisite and zoisite: an X-ray diffraction study. *American Mineralogist*, 82, 61-68.

Farrugia, L.J. (1999): WinGX suite for small-molecule single-crystal crystallography. *Journal of Applied Crystallography*, 32, 837-838.

Gatta, G.D. (2005): A comparative study of fibrous zeolites under pressure. *European Journal of Mineralogy*, 17, 411-421.

-. (2008): Does porous mean soft? On the elastic behaviour and structural evolution of zeolites under pressure. *Zeitschrift für Kristallographie*, 223, 160-170.
Holland, T.J.B. & Powell, R. (1998): An internally consistent thermodynamic data set for phases of petrologic interest. *Journal of Metamorphic Geology*, 16, 309-343.
Johnson, E.M. (2007): The elastic behavior of plagioclase feldspar at high pressure. *Dept of Geosciences*, MS. Virginia Tech, Blacksburg.
King Jr., H. & Finger, L.W. (1979): Diffracted beam crystal centering and its application of high-pressure crystallography. *Journal of Applied Crystallography*, 12, 374-378.
Lowenstein, W. (1954): The distribution of aluminum in the tetrahedra of silicates and aluminates. *American Mineralogist*, 39, 92-96.
Miletich, R., Allan, D.R., Kuhs, W.F. (2000): High-pressure single-crystal techniques. "High-Temperature and High-Pressure Crystal Chemistry", *in* R.M. Hazen, R.T. Downs, eds. 41, Mineralogical Society of America, Chantilly, Virginia, p. 445-519.
Nestola, F., Curetti, N., Benna, P., Ivaldi, G., Angel, R.J., Bruno, E. (2009): Compressibility and high-pressure behaviour of $Ab_{63}Or_{27}An_{10}$ anorthoclase. *The Canadian Mineralogist*, accepted.
Nestola, F., Gatta, G.D., Boffa Ballaran, T. (2006): The effect of Ca substitution on the elastic and structural behavior of orthoenstatite. *American Mineralogist*, 91, 809-815.
Nestola, F., Tribaudino, M., Boffa Ballaran, T. (2004): High pressure behavior, transformation and crystal structure of synthetic iron-free pigeonite. *American Mineralogist*, 89, 189-196.
Papike, J.J., and Zoltai, T. (1967): Ordering of tetrahedral aluminum in prehnite $Ca_2(AlFe^{+3})[Si_3AlO_{10}](OH)_2$. *American Mineralogist*, 52, 974-984.
Peng, S.-T., Chou, K.-D., Tang, Y.-C. (1959): The structure of prehnite. *Acta Chemistry Sinica*, 25, 56-63.
Preisinger, A. (1965): Prehnit- ein neuer Schichtsilikattyp. *Tschermaks Mineralogische und Petrograpische Mitteilungen*, 10, 491-504.
Putnis, A. (1992): *An introduction of mineral sciences*. 479 p. Cambridge University Press.
Ralph, R.L. & Finger, L.W. (1982): A computer program for refinement of crystal orientation matrix and lattice constants from diffractometer data with lattice symmetry constraints. *Journal of Applied Crystallography*, 15, 537-539.
Rath, S., Kunz, M., Miletich, R. (2003): Pressure-induced phase transition in malayaite, $CaSnOSiO_4$. *American Mineralogist*, 88, 293-300.
Robinson, K., Gibbs, G.V., Ribbe, P.H. (1971): Quadratic elongation: a quantitative measure of distortion in coordination polyhedra. *Science*, 172, 567-570.
Sheldrick, G.M. (2008): A short history of SHELX. *Acta Cryst.*, A64, 112-122.
Tribaudino, M. & Prencipe, M. (2001): The compressional behavior of P*4/n* vesuvianite. *The Canadian Mineralogist*, 39, 141-151.
Zhao, J. & Angel, R.J. (2009): Non-hydrostatic stresses in the diamond anvil pressure cell. *in prep*.

# Chapter 4: Infrared and Raman vibrational spectra of prehnite at ambient and high-pressure

## 4.1 Abstract

Ambient and high-pressure Raman and synchrotron infrared spectra (far-IR and mid-IR) were collected for the mineral prehnite from 1 bar and a maximum pressure of 20.4 GPa. Raman spectra measured at ambient conditions of four prehnite crystals with different compositions confirmed that there are no structural changes with different compositions, with the only change observed being the appearance of a peak in the octahedral motions region of the Mali sample (with an octahedral occupancy: Al 0.74, Fe 0.26). High-pressure results showed the majority of modes shifting in a smooth, linear fashion to higher frequencies as pressure was increased to 8 GPa. Above 8 GPa, changes in slopes were observed in a number of modes in both the Raman and IR, where the greatest change was observed in the OH-stretching region of the Raman spectra, 3400-3600 $cm^{-1}$, where the modes showed a shift to lower frequencies with increasing pressure. These shifts are thought to be a result of the tilting of polyhedra (octahedron and Si-tetrahedron) as compression occurs that changes the environment of the hydrogen, which is attached to the oxygen on the apex of the $(Al,Fe)O_6$ octahedron.

## 4.2 Introduction

In the previous chapters, the crystal structure, crystal chemistry, equation of state and structural changes of prehnite with pressure has been elucidated using X-ray diffraction and neutron diffraction. Vibrational spectroscopy provides a complementary method to diffraction techniques as it allows one to examine the interatomic vibrations of a material. Infrared spectroscopy, for example, provides an extremely sensitive probe to investigate the role of $OH^-$ in a structure (e.g. Aines & Rossman, 1984). In addition, the atomic vibrations control the bulk thermodynamic properties of a material (e.g. Kieffer & Navrotsky, 1985). Such studies have greater application to understanding the stability of hydrated metamorphic phases such as prehnite and their importance in transporting water into Earth's interior (e.g., Poli & Schmidt, 1995). Previous vibrational studies on talc and lawsonite (Daniel *et al.*, 2000; Holtz *et al.*, 1993; Scott &

Williams, 1999; Scott *et al.*, 2007), for example, have explored how hydrogen is retained within these metamorphic minerals, its pressure dependence and role in stabilizing these phases at high pressure. Although prehnite is a significant constituent of the higher levels of subduction zones and is an important metamorphic mineral more generally, very few spectroscopic studies of prehnite have been completed. The role of iron in the structure has been explored using XANES (Artioli *et al.*, 1995) and Mössbauer spectroscopy (Artioli *et al.*, 1995; Gangi Reddy *et al.*, 2005; Akasaka *et al.*, 2003) and the overtones of the hydroxyl ($OH^-$) modes in the near-infrared region (Gangi Reddy *et al.*, 2005). To date, however, there have been no vibrational studies of prehnite that characterize the vibrational modes and their distribution, nor have there been any studies that link the vibrational modes of prehnite with its thermodynamic properties.

In this chapter, the first complete vibrational study of prehnite including far-infrared, mid-infrared and Raman spectra measured between 100 and 4000 $cm^{-1}$ is presented. In addition, the pressure-dependence of the vibrational modes of prehnite to 16.04 GPa in the far-infrared, to 20.42 GPa in the mid-infrared, and to 10.3- 12.7 GPa in the Raman spectra is reported. The data allow us to explore the effect of pressure on the hydrogen environment in prehnite, as well as to probe the response of the structure to compression and, in particular, whether any high-pressure polymorphic phase transition occurs in prehnite, as is known to occur in other hydrous calcium aluminosilicate phases such as lawsonite and in the layered silicate muscovite (Daniel *et al.*, 2000; Faust & Knittle, 1994; Scott & Williams, 1999).

## 4.3 Experimental Methods

Prehnite samples from four different localities were used in this study, including Bealtan Quarry, Virginia, Mali, West Africa, Tyrol, Austria and Val Calanca, Switzerland. Electron microprobe analyses were performed on grain mounts with a Cameca SX50, using CaO, $SiO_2$, $Al_2O_3$, $Fe_2O_3$, and $MnO_3$ as standards. Microprobe analyses were completed on two samples using a wider range of elements (including Na, K, Mg, F, Ba, and Sr), however results revealed that these elements individually contributed to less than 0.05 weight percent and therefore were not used in the remaining analyses. Chemical compositions were calculated, assuming that all Fe and Mn were in the +3 valence state, and hydrogen was calculated by difference (Table 4.1).

Table 4.1: Details of prehnite microprobe compositions.

| Sample ID | tad0 | tad1 | tad4 | tad6 |
|---|---|---|---|---|
| source | Bealtan Quarry, Virginia<br>Virginia Tech Geos Museum | Tyrol, Austria<br>Nat Hist Museum<br>London | Mali<br>purchased | Val Calanca, Switzerland<br>from Dr. Diego Gatta |
| museum number | | bm 1916.641 | | |
| microprobe results<br>(error +/- 0.01) | Ca 1.96<br>(Al 0.80, Fe 0.20)<br>(Al Si 2.92 O 10)<br>(OH) 2 | Ca 2.06<br>(Al 0.93, Fe 0.07)<br>(Al Si 3.09 O 10)<br>(OH) 2 | Ca 1.92<br>(Al 0.74, Fe 0.26)<br>(Al Si 2.95 O 10)<br>(OH) 2 | *Ca 1.92<br>(Al 0.91, Fe 0.08, Mn 0.01)<br>(Al Si 3.14 O 10)<br>(OH) 2 |
| Formula weight | 414.33 | 412.90 | 419.07 | 415.44 |

*Note: All samples were measured at the Virginia Tech Microprobe Laboratory except tad6 (measured at JEOL JXA-8200 electron microprobe at the Dipartimento di Scienze della Terra- Milano)

Single crystals of each of the four samples were selected for Raman spectroscopic analysis on the basis of crystal quality and flatness of the cleavage plate. A Raman spectrum was collected on each sample at ambient conditions using a Dilor XY 0.64 meter Raman microprobe and accessory spectrometer with CCD multichannel detector using the 514 nm wavelength of the Ar+ laser. Two spectra were obtained: a low frequency spectrum from 150-1250 $cm^{-1}$ and a high frequency spectrum from 3000-4000 $cm^{-1}$. Spectra were corrected for background within the data collection software (LabSpec) and peaks were fit to the spectra assuming Gaussian peak profiles using the program Peakfit v4.12.

### *4.3.1 High-pressure Raman experiments*

A prehnite sample was provided by the Geosciences museum at Virginia Tech, from Bealtan Quarry, Virginia. A single crystal was cut from the sample and loaded into a diamond anvil cell designed for use in high-pressure spectroscopy measurements, with a T301 steel gasket along with a ruby sphere for pressure measurement (Mao *et al.*, 1986). The crystal was oriented with its dominant (001) cleavage face parallel to the diamond culets. A Raman spectrum was collected with a Dilor XY 0.64 meter Raman microprobe and accessory spectrometer with CCD multichannel detector using the 514 nm wavelength of the Ar+ laser. Two spectra were obtained at each pressure; a low frequency spectrum from 150-1250 $cm^{-1}$ and a high frequency spectrum from 3000-4000 $cm^{-1}$. Raman spectra were collected at 1 bar with no pressure-transmitting medium in the cell. A 4:1 methanol:ethanol mixture was subsequently loaded into the diamond

anvil cell as pressure-transmitting medium and Raman spectra were collected to 10.3 GPa. At every other pressure, the system was checked for calibration using a silicon standard. Data were background corrected in Origin 6.1 and the peaks were fit using Gaussian peak profiles.

A high-pressure Raman experiment on the prehnite sample from Mali was also completed on beamline U2A at NSLS, Brookhaven National Lab, New York NSLS. A single crystal was loaded into a Mao-Bell type diamond anvil cell equipped with low-fluorescent Type IIa diamonds, along with a steel gasket and two ruby spheres for pressure calibration (Mao *et al.*, 1986). The crystal was oriented with its dominant (001) cleavage face parallel to the diamond culets. A 4:1 methanol:ethanol fluid was loaded into the diamond anvil cell and Raman spectra were collected to 12.7 GPa. Although spectra were obtained between 80-1300 $cm^{-1}$ and 3000-3850 $cm^{-1}$, the peaks in the low-frequency spectra could not be analyzed due to the high level of background noise. The spectra were corrected for background and the peaks were fit using Gaussian profiles.

### *4.3.2 High-pressure infrared experiments*

High-pressure far-infared (FIR) and mid-infrared (MIR) spectra were collected on prehnite samples from Mali at beamline U2a of the National Synchrotron Light Source (NSLS), Brookhaven National Laboratory (Liu *et al.*, 2002). The prehnite powder was loaded into a Mao-Bell type diamond anvil cell, equipped with Type IIa diamonds, and a steel gasket. The powder was compressed between the diamonds to create a thin powder film. Infrared spectra were collected at 1 bar with no pressure-transmitting medium. High-pressure spectra were collected using KBr and petroleum jelly as pressure-transmitting media for the MIR and FIR regions, respectively. A ruby grain was loaded into the sample chamber as an internal pressure standard (Mao *et al.*, 1986). Infrared spectra were collected with a Bruker IFS 66v/S vacuum Fourier transform interferometer and a modified Bruker IRscope II microscope. Mid-infrared measurements were conducted using a KBr beamsplitter, a globar source and liquid $N_2$-cooled MCT detector. The FIR measurements used a custom-built vacuum IR microscope with a mylar beamsplitter and SiB/Si bolometer. MIR and FIR spectra were collected to 20.42 GPa and 16.04

GPa, respectively, at ~1 GPa increments. Six MIR and six FIR spectra were also collected on decompression.

Table 4.2: The irreducible representations of prehnite (a) *Pncm* (b) *P2cm*.

(a)

| | Ag ( R ) | B1g ( R ) | B2g ( R ) | B3g ( R ) | Au | B1u (IR) | B2u (IR) | B3u (IR) |
|---|---|---|---|---|---|---|---|---|
| M1 | 0 | 0 | 0 | 0 | 1 | 2 | 2 | 1 |
| T2 | 1 | 2 | 1 | 2 | 1 | 2 | 1 | 2 |
| T1 | 1 | 2 | 2 | 1 | 1 | 2 | 2 | 1 |
| Ca | 1 | 2 | 2 | 1 | 1 | 2 | 2 | 1 |
| H21 | 2 | 1 | 1 | 2 | 1 | 2 | 2 | 1 |
| O1 | 1 | 2 | 2 | 1 | 1 | 2 | 2 | 1 |
| O2 | 2 | 1 | 1 | 2 | 1 | 2 | 2 | 1 |
| O3 | 3 | 3 | 3 | 3 | 3 | 3 | 3 | 3 |
| O4 | 3 | 3 | 3 | 3 | 3 | 3 | 3 | 3 |
| Subtotal | 14 | 16 | 15 | 15 | 13 | 20 | 19 | 14 |
| Acoustics | | | | | | ** | ** | ** |
| Total optic modes | 123 | | | | | | | |

*Notes:* Ag, B1g, B2g, and B3g are Raman active. B1u, B2u, and B3u are IR active.

(b)

| | A1 | A2 | B1 | B2 |
|---|---|---|---|---|
| M1 | 2 | 1 | 1 | 2 |
| T22 | 1 | 1 | 2 | 2 |
| T21 | 1 | 1 | 2 | 2 |
| T1 | 3 | 3 | 3 | 3 |
| Ca | 3 | 3 | 3 | 3 |
| H61 | 2 | 1 | 1 | 2 |
| H62 | 2 | 1 | 1 | 2 |
| O5 | 3 | 3 | 3 | 3 |
| O61 | 2 | 1 | 1 | 2 |
| O62 | 2 | 1 | 1 | 2 |
| O71 | 3 | 3 | 3 | 3 |
| O72 | 3 | 3 | 3 | 3 |
| O81 | 3 | 3 | 3 | 3 |
| O82 | 3 | 3 | 3 | 3 |
| Subtotal | 33 | 28 | 30 | 35 |
| Acoustics | ** | | ** | ** |
| Total optic modes | 123 | | | |

*Notes* : All modes are Raman active, A1, B1 and B2 are IR active

## 4.4 Results

### *4.4.1 Raman and infrared spectra at 1 bar*

As described in Chapter 2, the prehnite crystal structure can be described in space groups *Pncm* or *P2cm* (Papike & Zoltai, 1967). *Pncm* is the average structure, containing a tetrahedral T2 site with disordered aluminum and silicon. In *P2cm*, the T2 site splits into two distinct sites- one containing Al, and the second Si. Other sites also split due to the lower symmetry, shifting from special positions in *Pncm* to general equivalent positions in *P2cm*. A factor group analysis was performed on the structure of prehnite using the correlation method of Fateley *et al.* (1972) in space groups *Pncm* and *P2cm*. Details of the calculations are given in Appendix A and summarized in Table 4.2. There are 42 atoms the primitive unit cell yielding a total of 126 vibrational modes, 3 of which are acoustic. Of the 123 optic modes in *Pncm*, 60 are predicted to be Raman active (14Ag+16B1g+15B2g+15B3g), 50 are predicted to be IR active (19B1u+18B2u+13B3u), and 13 are inactive (Au). In *P2cm*, 123 optic modes are predicted to be Raman active ($32A_1+28A_2+29B_1+34B_2$) and 95 are predicted to be IR active ($32A_1+29B_1+34B_2$).

The Raman spectra of the four prehnite samples collected under ambient conditions are shown in Figure 4.1 with refined peak positions presented in Table 4.3. A total of 31 to 35 peaks are observed, with all crystals showing the same basic overall pattern of peaks with minor peak shifts, band additions, or intensity differences. Figure 4.2 shows a typical Raman spectrum of a prehnite sample deconvoluted into Gaussian profiles. The spectra are characterized by continuous series of peaks from 100 to 600 $cm^{-1}$, followed by a gap between 640 $cm^{-1}$ and 900 $cm^{-1}$ where no strong peaks are present (Figure 4.1a) and another series of peaks from 850-1200 $cm^{-1}$. The remaining peaks that can be attributed to prehnite are observed between 3400 and 3500 $cm^{-1}$ (Figure 4.1b). The bands in this region consist of a strong peak near 3480 $cm^{-1}$ with a shoulder on each side.

The Raman modes can be grouped into four frequency ranges (modified after McKeown *et al.*, 1999a). Modes in the 3000-4000 $cm^{-1}$ represent OH stretching modes. At frequencies between 850-1200 $cm^{-1}$, T-O and T-O-T stretching and bending modes appear. Between 350 and 850

$cm^{-1}$, cation bending/stretching, as well as octahedral motions (M-O) are visible. Frequencies less than 350 $cm^{-1}$ represent lattice modes, involving multi-atom movement. These can overlap with octahedral bending/stretching and cation motions. Thus the peaks observed in the Raman spectra (Table 4.3) can be attributed to various stretching and bending atomic interactions. The three peaks found between 3440 and 3500 $cm^{-1}$ correspond to OH stretching vibrations. Of the 8 modes observed between 900-1150 $cm^{-1}$, the peaks at frequencies greater than 1000 $cm^{-1}$ may represent Si-O tetrahedral (Si1-O, T2-O) stretching and bending modes, while the peaks less than 1000 $cm^{-1}$ may be representative of Al-O (T2-O) tetrahedral stretching and bending modes.

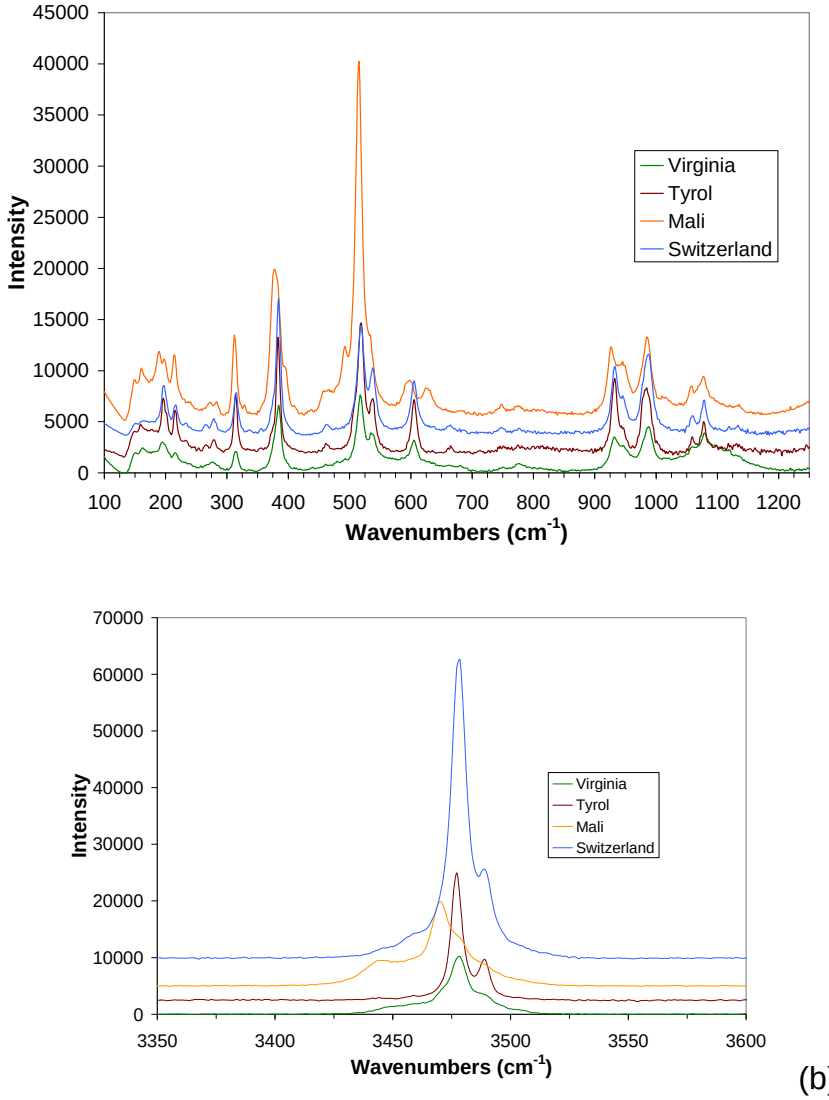


Figure 4.1: Raman spectra of prehnite single crystals from Bealtan Quarry, Virginia; Tyrol, Austria; Mali, West Africa; and Val Calanca, Switzerland taken at ambient conditions. (a) low frequency (b) OH-stretching frequency.

Table 4.3: Peak position, relative intensity, and peak widths of prehnite using Raman spectroscopy.

| Virginia | | | Tyrol | | | Mali | | | Switzerland | | |
|---|---|---|---|---|---|---|---|---|---|---|---|
| rel intensity | $\nu_o$ | FWHM | rel intensity | $\nu_o$ | FWHM | rel intensity | $\nu_o$ | FWHM | rel intensity | $\nu_o$ | FWHM |
| 20 | 148 | 9.2 | 12 | 147 | 10.1 | 6 | 148 | 7.5 | 6 | 150 | 8.7 |
| 22 | 160 | 14.8 | 15 | 160 | 14.7 | 13 | 163 | 21.9 | 10 | 164 | 19.2 |
| 27 | 179 | 31.7 | 16 | 181 | 31.9 | 17 | 188 | 15.6 | 9 | 185 | 21.6 |
| 30 | 198 | 15.6 | 33 | 198 | 10.5 | 13 | 200 | 11.4 | 37 | 198 | 11.5 |
| 21 | 215 | 12.8 | 28 | 216 | 11.3 | 16 | 214 | 10.3 | 23 | 216 | 10.8 |
| 12 | 233 | 23.2 | 8 | 233 | 13.7 | 4 | 231 | 24.4 | 7 | 232 | 18.0 |
| | | | 4 | 266 | 8.2 | | | | 7 | 265 | 8.8 |
| 12 | 275 | 19.9 | 9 | 279 | 8.4 | 3 | 275 | 18.6 | 11 | 279 | 9.6 |
| 28 | 314 | 9.7 | 42 | 314 | 7.9 | 24 | 313 | 8.1 | 34 | 315 | 9.2 |
| | | | | | | 2 | 324 | 11.7 | 2 | 336 | 6.0 |
| 3 | 361 | 8.9 | 2 | 356 | 7.3 | | | | 3 | 357 | 7.7 |
| 30 | 375 | 11.0 | 15 | 374 | 10.8 | | | | 25 | 375 | 10.8 |
| 91 | 384 | 10.5 | 75 | 383 | 6.5 | 47 | 379 | 17.8 | 100 | 384 | 7.1 |
| 12 | 397 | 9.5 | 19 | 388 | 11.9 | 10 | 397 | 9.3 | 20 | 389 | 16.4 |
| 8 | 461 | 14.7 | 5 | 462 | 8.3 | 8 | 466 | 25.8 | 7 | 463 | 9.3 |
| 10 | 478 | 11.6 | 2 | 489 | 27.3 | 20 | 493 | 16.7 | 3 | 481 | 21.0 |
| 17 | 495 | 20.3 | 23 | 506 | 9.8 | 24 | 507 | 9.1 | 13 | 505 | 18.6 |
| 35 | 511 | 10.9 | | | | | | | | | |
| 100 | 519 | 11.1 | 100 | 519 | 12.7 | 100 | 515 | 10.2 | 89 | 519 | 13.4 |
| 58 | 537 | 19.8 | 41 | 537 | 13.2 | 28 | 529 | 23.7 | 54 | 538 | 14.9 |
| 44 | 605 | 20.2 | 39 | 605 | 11.0 | 10 | 596 | 23.2 | 39 | 605 | 14.1 |
| | | | | | | 7 | 627 | 20.8 | 6 | 621 | 46.2 |
| | | | 3 | 665 | 5.9 | | | | 5 | 665 | 15.4 |
| 4 | 751 | 11.8 | 3 | 751 | 14.8 | 2 | 748 | 10.1 | 4 | 748 | 10.1 |
| 9 | 777 | 20.1 | 4 | 777 | 16.3 | 2 | 775 | 17.7 | 3 | 776 | 11.8 |
| 47 | 932 | 17.2 | 54 | 932 | 11.3 | 18 | 927 | 15.9 | 52 | 932 | 13.4 |
| 33 | 950 | 19.5 | 17 | 945 | 14.7 | 15 | 947 | 21.7 | 27 | 948 | 18.6 |
| 64 | 987 | 24.2 | 50 | 984 | 18.8 | 22 | 985 | 23.3 | 67 | 986 | 21.2 |
| 36 | 1059 | 31.3 | 9 | 1060 | 10.0 | 7 | 1058 | 20.1 | 14 | 1060 | 13.3 |
| 37 | 1080 | 15.1 | 22 | 1078 | 10.2 | 10 | 1077 | 15.7 | 26 | 1078 | 10.6 |
| 36 | 1099 | 25.2 | 4 | 1096 | 18.8 | 4 | 1096 | 19.4 | 4 | 1092 | 25.9 |
| 21 | 1118 | 15.0 | 3 | 1119 | 9.1 | 2 | 1118 | 20.3 | 4 | 1119 | 6.6 |
| 21 | 1136 | 23.0 | 5 | 1132 | 12.5 | 2 | 1135 | 10.9 | 5 | 1133 | 12.4 |
| 35 | 3469 | 40.6 | 8 | 3470 | 19.0 | 48 | 3444 | 19.8 | 21 | 3478 | 36.9 |
| 100 | 3478 | 8.2 | 100 | 3477 | 5.9 | 96 | 3470 | 7.6 | 100 | 3478 | 7.1 |
| 29 | 3487 | 20.0 | 32 | 3488 | 8.5 | 100 | 3474 | 31.7 | 20 | 3489 | 7.0 |

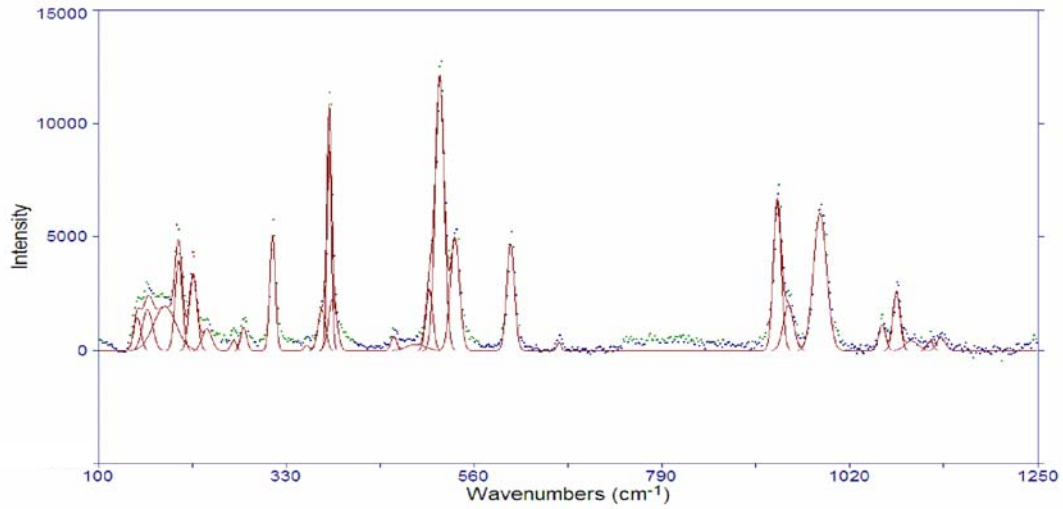


(a)

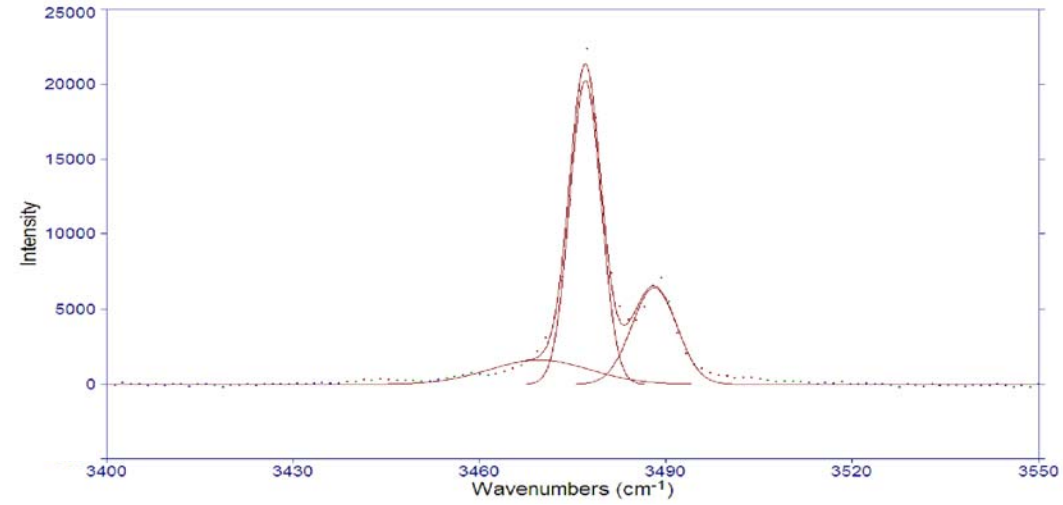


(b)

Figure 4.2: Ambient Raman spectra of prehnite (Tyrol, Austria) (a) Low frequency modes fitted with 30 peaks (b) High frequency modes fitted with 3 peaks. See Table 4.3 for peak positions and FWHM values.

The bands below 640 $cm^{-1}$ are a bit more difficult to assign. An Al-O octahedral (M1-O) stretching band is expected at 600 $cm^{-1}$, which could be attributed to a band at 596-605 $cm^{-1}$, sometimes with a nearby shoulder. Some differences are observed in the sample from Mali between 580 $cm^{-1}$ and 640 $cm^{-1}$ (Figure 4.1a). The sample from Mali shows a peak at 529 $cm^{-1}$ compared to 537 $cm^{-1}$ in the other samples, 596 $cm^{-1}$ compared to 605 $cm^{-1}$, and a new peak at 627 $cm^{-1}$ not observed in the other samples. Although the sample from Mali has a higher iron content than the other samples (Table 4.1) and the iron occupies the octahedral site in prehnite (Artioli *et al.*, 1995), one would expect a lower frequency band due to the substitution of Fe for Al in the octahedral region rather than a higher frequency band. Additionally, the extra band is not seen in the sample from Virginia, with only 0.06 apfu difference in Fe content.

There are 16 to 19 prominent peaks in the Raman spectra below 560 $cm^{-1}$ that are difficult to assign unambiguously. They likely are due to overlapping octahedral motions, vibrational modes involving the calcium atom in the channel of the structure, and long-range lattice motions. Assigning these modes requires a full lattice dynamical study which is outside the scope of this thesis.

The far-infrared and mid-infrared spectra on the sample from Mali are shown in Figures 4.3 and 4.4, respectively. The bands between ~800 $cm^{-1}$ and 1200 $cm^{-1}$ cannot be resolved, but correspond to internal vibrational modes of the tetrahedra- stretching and bending of the Si-O and Al-O. In the frequency range 300-600 $cm^{-1}$, there are many unresolved modes which are attributed to octahedral vibrations and Ca-atom motions. Modes below 300 $cm^{-1}$ are a complex combination of octahedral motions, Ca-atom motions, and lattice modes.

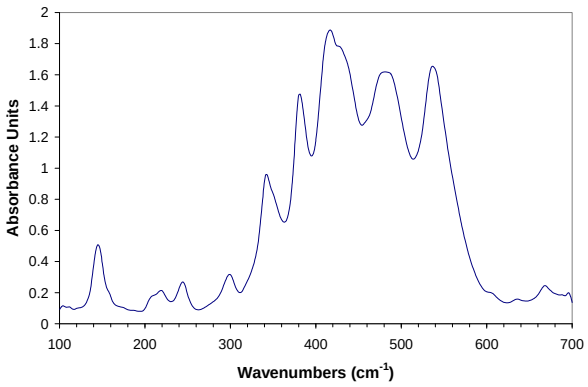


Figure 4.3: Far-IR spectrum of prehnite from Mali taken in ambient conditions.

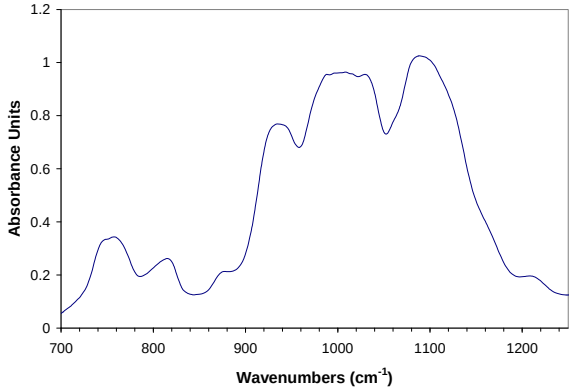


(a)

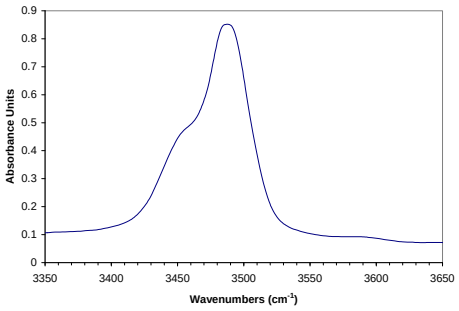


(b)

Figure 4.4: Mid-IR spectrum of prehnite from Mali taken at ambient conditions (a) low frequency (b) OH-stretching frequency.

A maximum of 35 Raman modes and a maximum of 25 infrared modes are observed, well below the number predicted by FGA for either space group *Pncm* or *P2cm*. However, one usually requires polarized infrared and Raman spectra from oriented single crystals to measure all the modes of a phase (e.g. Hofmeister *et al.*, 1999). It is likely that there are some peaks of prehnite too weak to be observed, others that have very similar energies and overlap with observed peaks, and others that may occur below 100 $cm^{-1}$, outside the range of the infrared and Raman experiments.

### *4.4.2 High-pressure Raman and infrared spectra*

Eleven Raman spectra measured from the single crystal of prehnite from Virginia were collected between 1 bar and 10.3 GPa. The range of high-pressure spectra is shown in Figure 4.5. Many of the peaks have shoulders, or display split positions with pressure, or broaden with pressure, thus only those peaks that could be unequivocally tracked as a function of pressure were analyzed. A total of 17 peaks were tracked: 14 peaks between 200 $cm^{-1}$ and 1200 $cm^{-1}$, and three peaks between 3400 $cm^{-1}$ to 3500 $cm^{-1}$ (Table 4.4). The peaks in the OH region display one sharp central peak, with a shoulder on either side. As a result, three peaks reproduce the spectrum well with the best constraint on the position of the strongest peak in this region. Upon compression to 7.8 GPa, the majority of the peaks between 200 $cm^{-1}$ and 1200 $cm^{-1}$ shift toward higher wavenumbers (Figure 4.7) with slopes, $\delta v/\delta P$ that range from 0.9 $cm^{-1}$/GPa to 7.1 $cm^{-1}$/GPa (Table 4.4). The peaks occurring between 200 $cm^{-1}$ and 520 $cm^{-1}$ show the smallest shifts with pressure while the peaks between 520 $cm^{-1}$ and 1200 $cm^{-1}$ show the largest shifts with pressure. There is one band, at $v_o$ = 366 $cm^{-1}$ at room pressure, that softens as pressure is increased up to 6 GPa, while above 6 GPa, the band changes slope to increase with pressure. Softening is usually a precursor to a structural phase transition. Above 8 GPa, the majority of the modes exhibit a significant change in slope with pressure. With the exception of two tetrahedral modes (Figure 4.6c), all the modes stiffen above 8 GPa (Figure 4.6a-d). These changes are consistent with prehnite undergoing a phase transition above 8 GPa, but without any major change in the structure. Within the OH region, the peaks shift to higher frequencies with increasing pressure up to 7.8 GPa. Above 7.8 GPa, the frequencies of the OH modes decrease as pressure increases with $\delta v/\delta P$ = -7.3 $cm^{-1}$/GPa for the strongest peak in this region (Figure 4.6d). All of these changes in

the Raman spectra are consistent with the changes observed in the EoS and they are reported in Chapter 3.

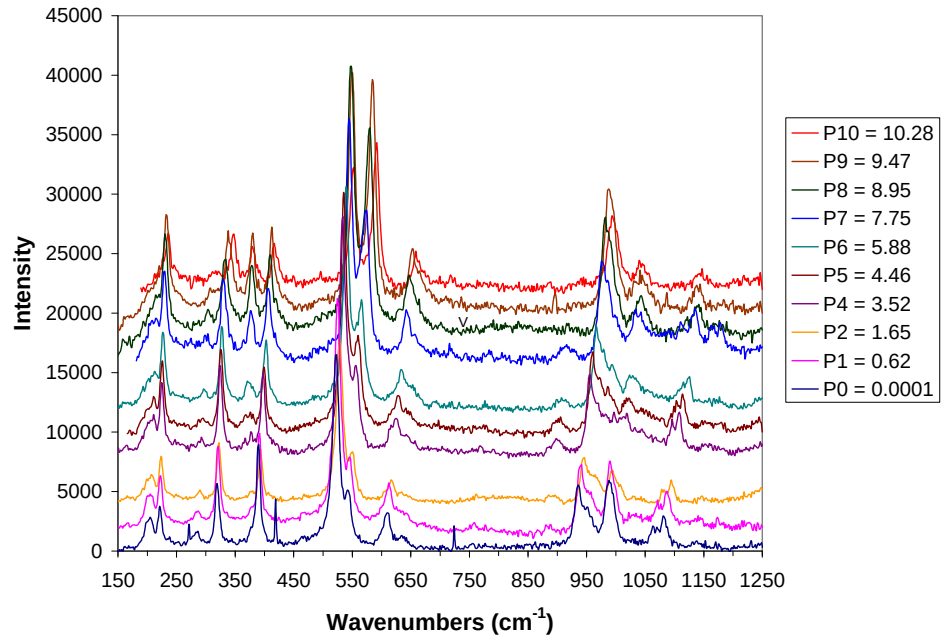


(a)

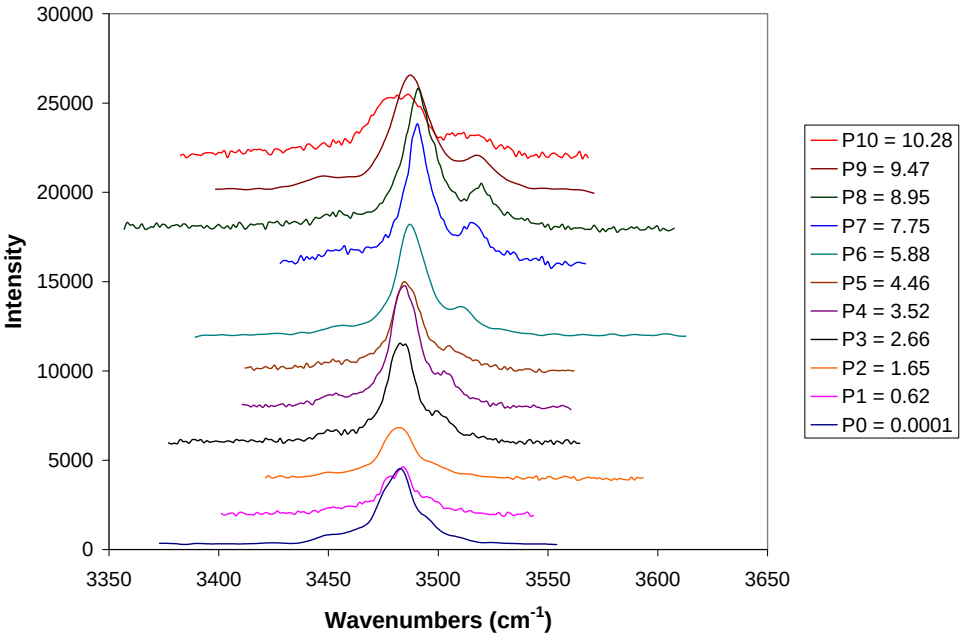


(b)

Figure 4.5: Raman spectra of prehnite as a function of increasing pressure (GPa) in the (a) low frequency region (b) OH-stretching frequency region.

Table 4.4: Peak positions and pressure dependence of Raman bands of prehnite from Virginia

| | $v_o$ ($cm^{-1}$) | FWHM | $\delta v/\delta P$* ($cm^{-1}$/GPa) | $\gamma_o$** |
|---|---|---|---|---|
| **Raman** | Prehnite- Single crystal from Virginia | | | |
| | 203 | 7.4 | 0.85 | 0.46 |
| | 222 | 9.8 | 0.93 | 0.46 |
| | 319 | 8.4 | 1.40 | 0.48 |
| | 380 | 9.7 | -0.68 | -0.20 |
| | 390 | 7.1 | 2.17 | 0.61 |
| | 522 | 14.5 | 2.82 | 0.59 |
| | 544 | 10.3 | 3.53 | 0.71 |
| | 609 | 15.9 | 4.34 | 0.78 |
| | 636 | 15.2 | 3.10 | 0.53 |
| | 935 | 15.1 | 5.17 | 0.60 |
| | 952 | 19.6 | 4.96 | 0.57 |
| | 989 | 19.3 | 7.10 | 0.78 |
| | 1071 | 27.5 | 6.02 | 0.61 |
| | 1082 | 11.9 | 6.88 | 0.69 |
| | 3481 | 16.3 | 1.26 | 0.04 |
| | | | *** -7.3 | |
| | 3499 | 22.5 | 2.67 | 0.08 |
| | | | *** -2.8 | |

* Slope changes direction below 9 GPa
** Mode Grüneisen parameter where KT = 109.29(18) (Chapter 3)
*** Slope change above 9 GPa

For comparison, the effect of pressure on the OH stretching modes of the prehnite sample from Mali was investigated. Eleven spectra were collected from 1 bar up to 12.68 GPa and, similar to the previous study, three peaks were observed in the OH spectrum, one sharp peak and a shoulder on either side of the main peak (Figure 4.7). The shoulders were only fit marginally well, due to peak broadening with pressure, and the shifting of peaks obscuring their positions. However, the main peak was easily tracked as a function of pressure and shows a similar trend as the sample from Virginia (Figure 4.8). For pressures up to 8.7 GPa, the peak shifts slightly to higher wavenumbers with $\delta v/\delta P = 0.9$ $cm^{-1}$/GPa, but, at pressures greater than 8.7 GPa, the OH peak shifts toward lower wavenumbers with $\delta v/\delta P = -1.3$ $cm^{-1}$/GPa. Although the shifts in the OH stretching modes of the sample from Mali are similar to the previous study, the shifts are not as pronounced. This may be due to the higher content of Fe in the sample that may have contributed to higher noise level and backgrounds in the Raman spectra that made the peaks difficult to resolve. The presence of Fe in the octahedral M1 site may have also affected the M-OH stretching vibration modes.

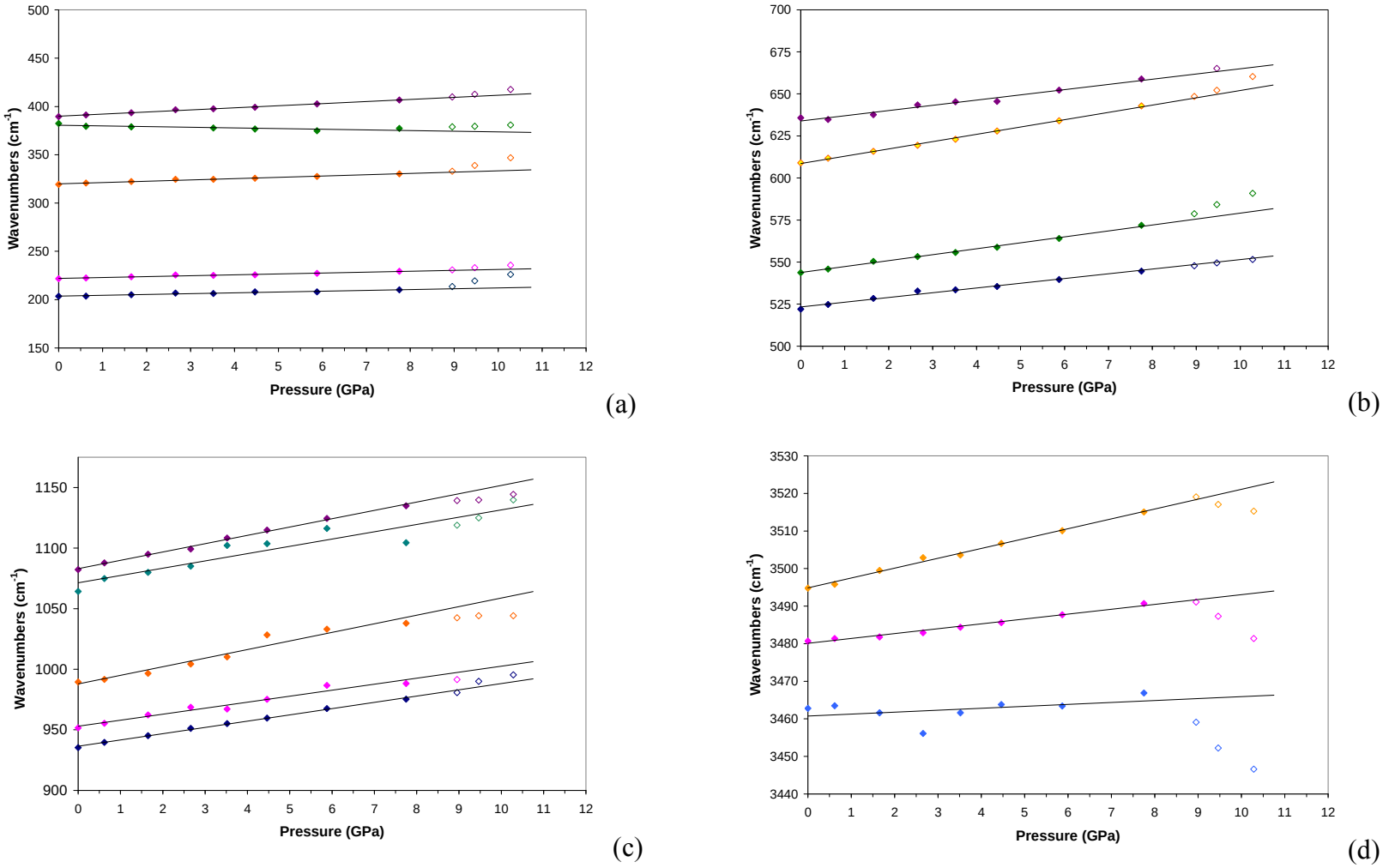


Figure 4.6: Peakshift as a function of pressure for the Raman spectra collected on a prehnite sample from Virginia. Solid lines represent pressure dependence of low-pressure modes. (a) 150-500 $cm^{-1}$ (b) 500-700 $cm^{-1}$ (c) 900-1200 $cm^{-1}$ (d) 3450-3530 $cm^{-1}$.

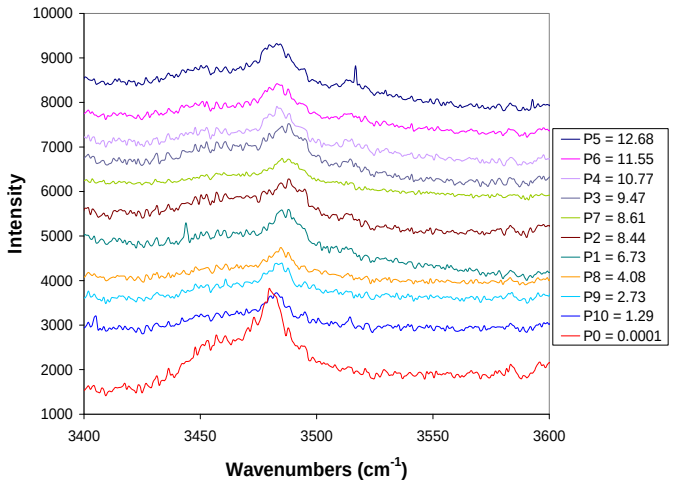


Figure 4.7: Raman spectra of prehnite from Mali as a function of increasing pressure (GPa) in the OH-stretching region.

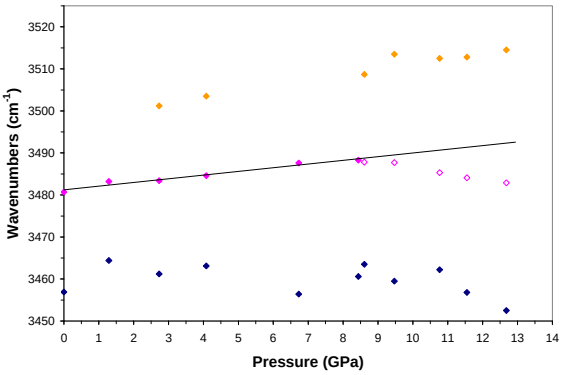


Figure 4.8: Peakshift as a function of pressure for the Raman spectra collected on a prehnite sample from Mali. Solid line represents pressure dependence of low-pressure mode.

Seventeen spectra in the far-infrared region were collected from 1 bar up to 16.04 GPa on the sample from Mali. Because of the strong peak overlaps, only a few peaks can be clearly followed as a function of pressure. The frequencies of the four bands that were fit are shown in Figure 4.9. There is considerable uncertainty in the peak positions because of the peak overlap. Nonetheless, some appear to show small changes in slope around 9 GPa (Figure 4.10a-b), which correspond to visible changes in the spectra (Figure 4.9). The peak at ~150 $cm^{-1}$ splits into two components at pressures above 9 GPa.

In order to explore the infrared modes of the Mali sample at higher pressures, spectra in the mid-infrared were collected from 1 bar up to 20.42 GPa. Twenty-four spectra were collected over this pressure range and spectra are shown in Figure 4.11. It is not possible to deconvolute the spectra in this frequency range into individual peaks unambiguously. Nonetheless, it can be observed that the envelope of peaks (900-1200$cm^{-1}$) shifts to higher frequencies with increasing pressure. Above ~14 GPa, the individual maxima are less well resolved, which probably indicates that the individual peaks are broadening due to non-hydrostatic stresses. In the OH-stretching region, a sharp, well-defined peak of high intensity at 3490 $cm^{-1}$ is observed along with a broad shoulder at slightly lower frequency, 3456 $cm^{-1}$. The peak at 3490 $cm^{-1}$ changes little over the pressure range studied. There is a suggestion that there is a slight shift to higher wavenumbers followed by a slightly downward trend above 10 GPa as observed in the high-pressure Raman spectra.

However, the trends are less definitive and these may be due to the different pressure media used in each study. In the high-pressure Raman studies, a 4:1 mixture of methanol:ethanol was used as the pressure-transmitting medium which has been shown to be hydrostatic to 10 GPa (Angel *et al.*, 2007). In the high-pressure MIR study, a powder sample of prehnite was dispersed in KBr which was used as the pressure–transmitting medium. Although KBr is transparent in the MIR spectrum, it is quasi-hydrostatic at best.

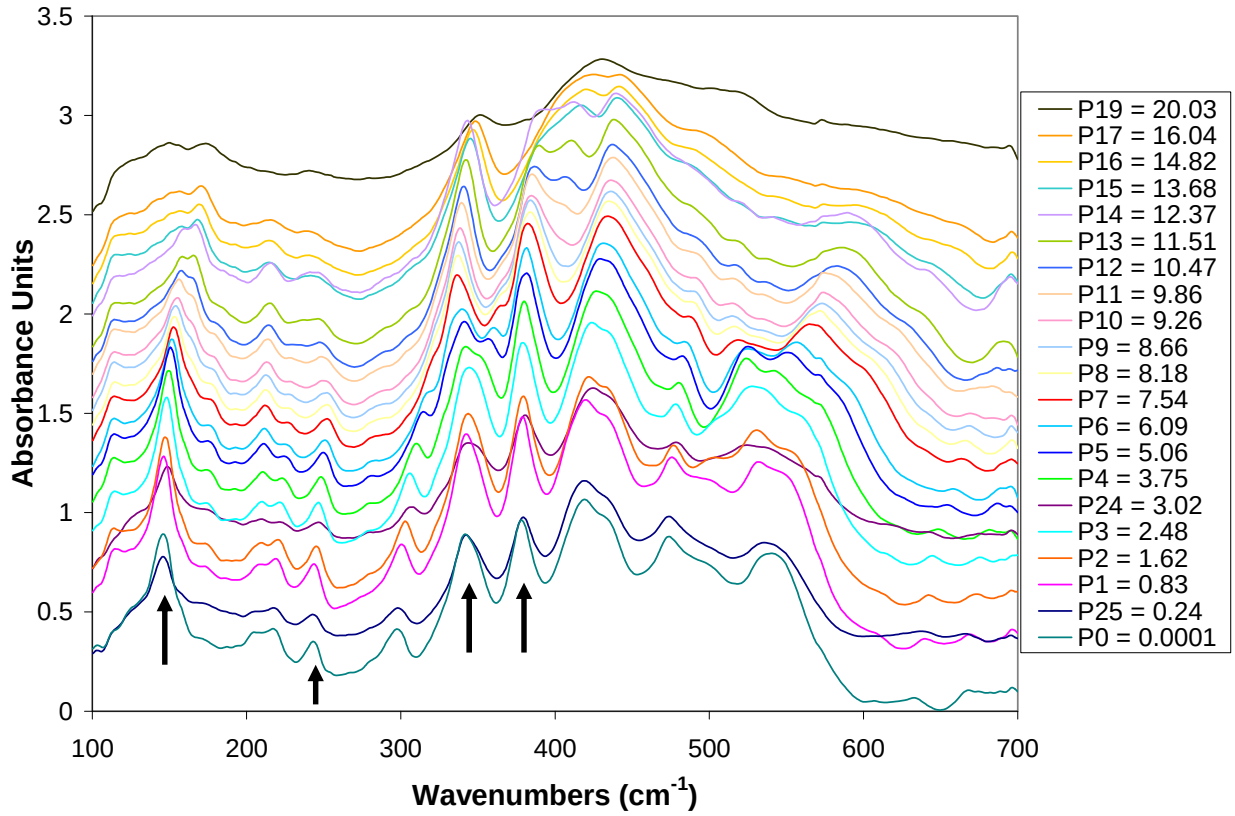


Figure 4.9: Far-infrared spectra of prehnite from Mali as a function of increasing pressure (GPa). The four peaks marked with arrows are the peaks tracked as a function of pressure. Note that above 16 GPa, the peaks became broad (as shown by P19, 20.03 GPa) and were not used in any analysis.

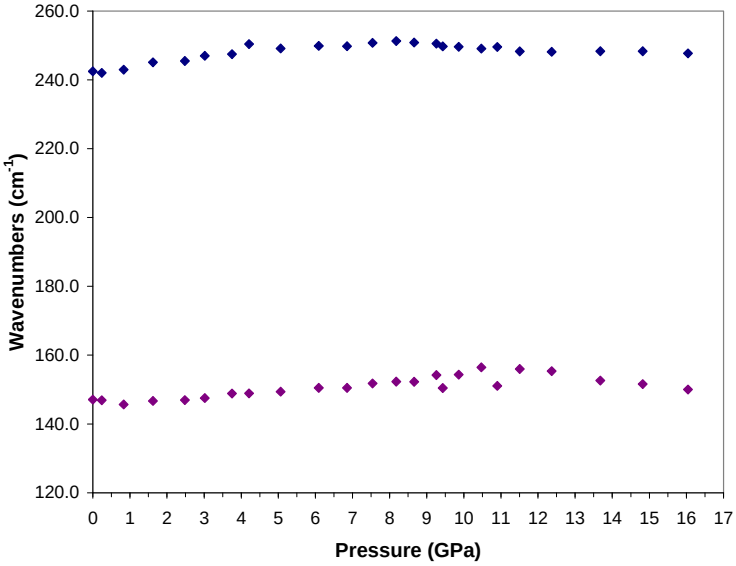


(a)

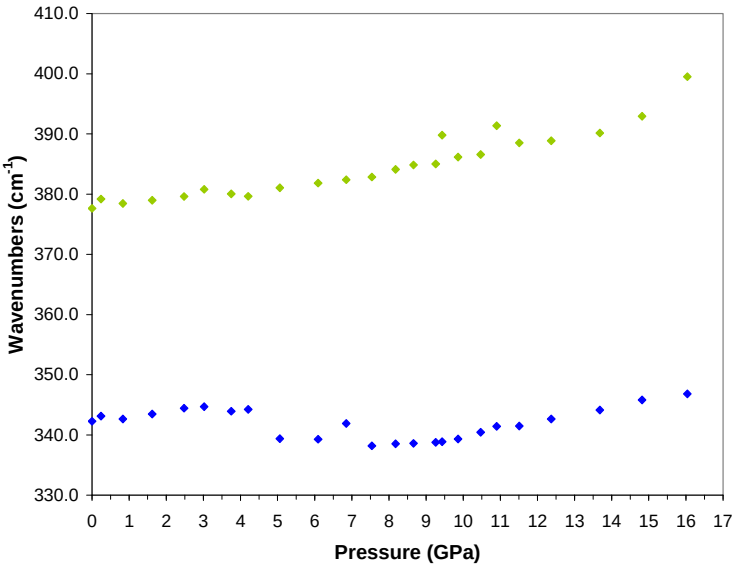


(b)

Figure 4.10: Pressure dependence of the far-IR peak positions of prehnite from Mali. (a) 120-260 $cm^{-1}$ (b) 330-410 $cm^{-1}$.

## 4.5 Discussion

### *4.5.1 High-pressure spectra*

This was the first study examining the vibrational modes of prehnite at high pressure with infrared and Raman spectroscopy. The high-pressure single-crystal X-ray diffraction study described in Chapter 3 indicated that prehnite does not undergo a symmetry change between 1 bar and 10 GPa and maintains at least the average symmetry *Pncm*. This result is consistent with

the high-pressure spectroscopy results. The majority of modes in both Raman and infrared showed a smooth, continuous increase with pressure (Figures 4.6, 4.10a-b). Within the Raman, peaks with $v_o$ of less than 530 $cm^{-1}$ generally have slopes less than 2.5, while peaks with $v_o$ between 500 $cm^{-1}$ and 700 $cm^{-1}$ have slopes greater than 2.5. This could be attributed to changes in the octahedral environment with pressure. A change in slope is also observed in the high-pressure Raman spectra, where slopes range from 0.9- 4.3 $cm^{-1}$/GPa at frequencies less than 700 $cm^{-1}$, and, above 700 $cm^{-1}$, slopes increase from 4.9 $cm^{-1}$/GPa to 7.1 $cm^{-1}$/GPa. This may be due to the increase in angular variance of the $(Al,Si)O_4$ tetrahedra with pressure observed in the high-pressure single-crystal X-ray diffraction study (Chapter 3).

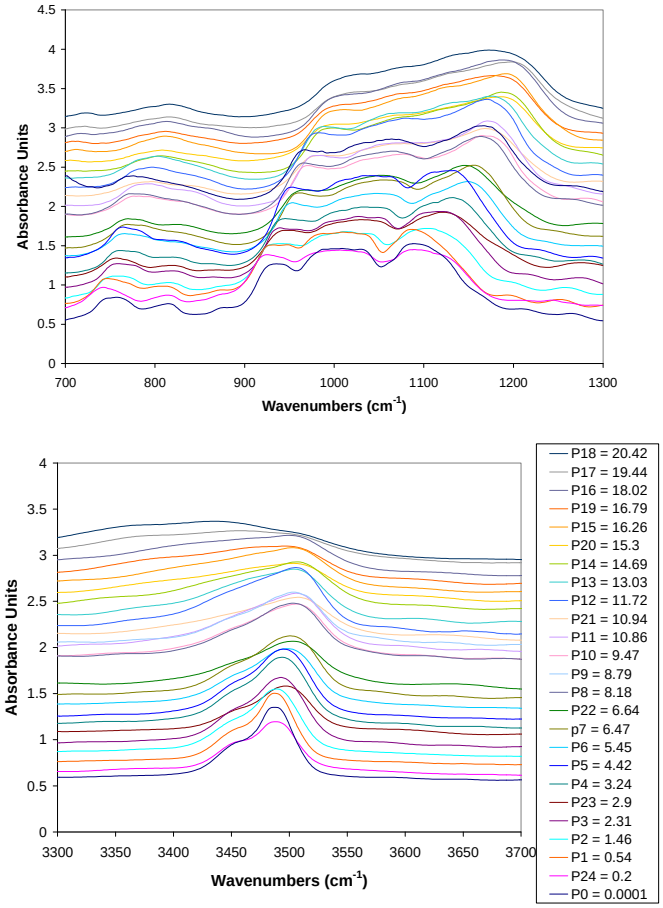


Figure 4.11: Mid-infrared spectra of prehnite from Mali as a function of increasing pressure (GPa), where the legend of pressures is the same for both plots. (a) 700-1300 $cm^{-1}$ (b) 3200-3700$cm^{-1}$.

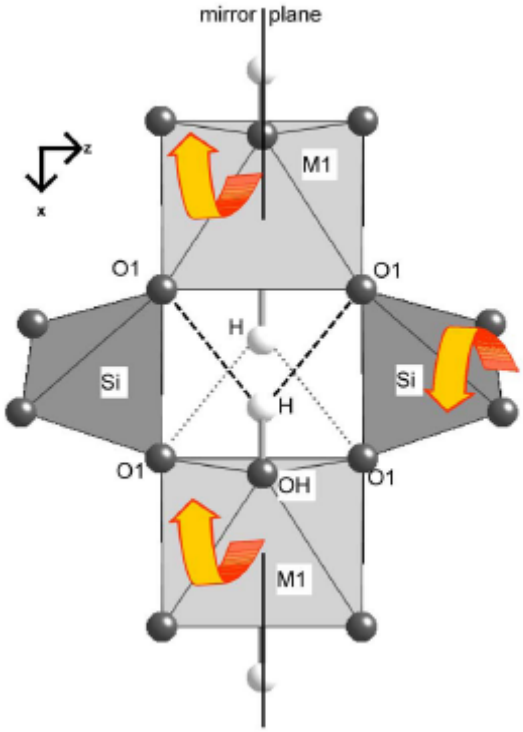


Figure 4.12: The hydrogen environment in prehnite as viewed from [010]. The small gray spheres represent oxygen sites, whereas the small white spheres represent hydrogen sites. The heavy dash shows the bifurcated environment of the H and the next nearest oxygen, O1. The light dash shows the bifurcated environment of the H and O1 on the lower apex of the octahedron. The arrows represent the tilting compression mechanism that may play a role in changing the hydrogen environment with pressure.

The corresponding mode Grüneisen parameters for these Raman peaks are given in Table 4.4. The Grüneisen parameters were calculated using the following definition, $\gamma_p = (K_T/\nu_{io})(\delta\nu/\delta P)$, where $K_T$ is the bulk modulus, $\nu_{io}$ is the frequency at 1 bar, and $\delta\nu/\delta P$ is the slope the peak tracked with pressure (Hofmeister *et al.*, 1999). The mode Grüneisen parameters of prehnite are very similar to those observed in Phase A, Phase B, and Superhydrous Phase B (Hofmeister *et al.*, 1999).

Above ~8 GPa most of the Raman bands exhibit a change in slope, most of them becoming stiffer with the exception of two modes that are attributed to internal vibrations of the $TO_4$ tetrahedra (Figure 4.6). In addition, there are significant changes in relative intensities of the Raman modes at lower frequencies, for example the pair of peaks at 550 $cm^{-1}$. Such changes indicate that the structure has undergone a phase transition that preserves the general structure

and topology. This is entirely consistent with the X-ray diffraction data collected above 9 GPa, which indicated that the average symmetry of prehnite is preserved.

Major changes are observed in the OH region of the Raman spectra, from 3400-3500 $cm^{-1}$, where a change in the frequency of the O-H peaks with pressure was observed. As described in Chapter 2, the H atom in prehnite is bonded to the apical oxygen of the $(Al,Fe,Mn)O_6$ octahedron, attached to the OH atom in agreement with bond valance calculations. The O-H vector points away from the adjacent calcium atoms. The hydrogen atom occupies a special position on a mirror plane in both Pncm and P2cm space groups. If the hydrogen atom participates in a hydrogen bond, the mirror symmetry requires that the hydrogen environment is bifurcated and involves two oxygen atoms on an adjacent octahedron (Figure 4.12). Between 1 bar and 8.7 GPa, the Raman peaks corresponding to the O-H absorption stiffen with pressure (Figure 4.6). The positive shift of the hydroxyl stretching vibration is similar to trends observed for metamorphic phases such as members of the humite family (e.g., Liu *et al.*, 2003; Hofmeister *et al.*, 1999), clinochlore (Kleppe *et al.*, 2003), talc (Holtz *et al.*, 1993; Scott *et al.*, 2007), and topaz (Bradbury & Williams, 2003). The positive shift may be due to the polarizability of the oxygen ion increasing under pressure, resulting in a stronger hydroxyl stretching bond, and thus higher vibrational frequency (e.g., Bradbury & Williams, 2003). In addition, cation-hydrogen repulsion may also play a role. Pressure may induce an increase in repulsion between the hydrogen and surrounding cations resulting in a shortening, and resultant strengthening, of the hydroxyl bond.

Above 8.7 GPa the O-H stretching vibration softens. This change in slope was observed in the high-pressure Raman spectra collected on the sample from Virginia and the sample from Mali which contain different amounts of iron (Table 4.1). This change in slope is not as well defined in the high-pressure infrared data collected on the sample from Mali (Figure 4.10). The Raman results suggest that the environment of the hydrogen, which is bonded to the apical oxygen of the octahedron, changes above 8.7 GPa. One possibility that is consistent with these observations is that the H is displaced off the mirror plane, so that the hydrogen bond to one of the O1 oxygen atoms becomes stronger (the other being destroyed) and this is turn slightly weakens the O-H bond.

## 4.6 Conclusions

The first comprehensive vibrational study of prehnite, including far-infrared, mid-infrared and Raman spectra collected between 100- 4000 $cm^{-1}$, has yielded some interesting results. The Raman spectra collected from samples with different compositions from four different localities are very similar, with the exception of the position of two minor peaks and the appearance of a new peak in the Fe-rich prehnite sample from Mali in the region between 580 $cm^{-1}$ and 640 $cm^{-1}$. Although uncertain at this point, these peaks may be due to differences in sample orientation and/or differences in the octahedral vibrations. However, the overall striking similarity between the spectra from different samples is consistent with the results from Chapter 2 that indicate prehnite samples from various localities, having different compositions, have the same crystal structure.

In examining the pressure effects of prehnite using infrared and Raman spectroscopy, the compression of the structure was evident in the general increase in frequencies of the modes with pressure to 8.5 GPa. The softening of one low-frequency mode presages the phase transition at ~9 GPa that was observed by measurements of the lattice parameters by single-crystal X-ray diffraction (Chapter 3). The nature of the phase transition can be in part constrained by the changes in the spectra in the 8-10 GPa pressure range. The greatest change in the spectra is the softening of the modes in the OH-stretching region, 3400-3600 $cm^{-1}$, which indicates a slight weakening of the O-H bond. If this is due to the movement of the H off the mirror plane, this would involve a strengthening of one hydrogen bond to an O1 oxygen, and the breaking of another. The change in bonding of the O1 oxygen atoms could then be the cause of the changes in slopes of the remaining Raman modes. Nonetheless, the fact that the spectra show only minor changes across the phase transition is consistent with the results presented in Chapter 3 in that the prehnite average structure, *Pncm*, is maintained as pressure is increased to 10 GPa.

## 4.7 References


Aines, R.D. & Rossman, G.R. (1984): Water in minerals? A peak in the infrared. *Journal of Geophysical Research*, 89 (B6), 4059-4071.

Akasaka, M., Hashimoto, H., Makino, K., Hino, R. (2003): $^{57}$Fe Mossbauer and X-ray Rietveld studies of ferrian prehnite from Kouragahana, Shimane Peninsula, Japan. *Journal of Mineralogical and Petrological Sciences*, 98, 31-40.

Angel, R.J., Bujak, M., Zhao, J., Gatta, G.D., Jacobsen, S.D. (2007): Effective hydrostatic limits of pressure media for high-pressure crystallographic studies. *Journal of Applied Crystallography*, 40, 26-32.

Artioli, G., Quartieri, S., Deriu, A. (1995): Spectroscopic data on coexisting prehnite-pumpellyite and epidote-pumpellyite. *Canadian Mineralogist*, 33, 67-75.

Bradbury, S.E. & Williams, Q. (2003): Contrasting behavior of two hydroxyl-bearing metamorphic minerals under pressure: Clinozoisite and topaz. *American Mineralogist*, 88, 1460-1470.

Daniel, I., Fiquet, G., Gillet, P., Schmidt, M.W., Hanfland, M. (2000): High-pressure behaviour of lawsonite: a phase transition at 8.6 GPa. *European Journal of Mineralogy*, 12, 721-733.

Fateley, W.G., Dollish, F.R., McDevitt, N.T., Bentley, F.F. (1972): *Infrared and Raman selection rules for molecular and lattice vibrations: the correlation method*. 222 p. Wiley-Interscience, New York.

Faust, J. & Knittle, E. (1994): The equation of state, amorphization, and high-pressure phase diagram of muscovite. *Journal of Geophysical Research*, 99 (B10), 19,785-719,792.

Gangi Reddy, N.C., Fayazyddin, S.M., Rama Subba Reddy, R., Siva Reddy, G., Lakshmi Reddy, S., Sambsiva Rao, P., Jagannatha Reddy, B. (2005): Characterisation of prehnite by EPMA, Mossbauer, optical absorption, and EPR spectroscopic methods. *Spectrochimica Acta Part A*, 62, 71-75.

Hofmeister, A.M., Cynn, H., Burnley, P.C., Hemley, R.J. (1999): Vibrational spectra of dense, hydrous magnesium silicates at high pressure: Importance of the hydrogen bond angle. *American Mineralogist*, 84, 454-464.

Holtz, M., Solin, S.A., Pinnavaia, T.J. (1993): Effect of pressure on the Raman vibrational modes of layered aluminosilicate compounds. *Physical Review B*, 48, 13,312-313,317.

Kieffer, S.W. & Navrotsky, A. (1985): Microscopic to Macroscopic: Atomic Environments to Mineral Thermodynamics. *in* P.H. Ribbe, Ed. *Reviews in Mineralogy and Geochemistry*, 14, p. 428. Mineralogical Society of America, Chantilly, VA.

Kleppe, A.K., Jephcoat, A.P., Welch, M.D. (2003): The effect of pressure upon hydrogen bonding in chlorite: A Raman spectroscopic study of clinochlore to 26.5 GPa. *American Mineralogist*, 88, 567-573.

Liu, Z., Hu, J., Yang, H., Mao, H.K., Hemley, R.J. (2002): High-pressure synchrotron x-ray diffraction and infrared microspectroscopy: applications to dense hydrous phases. *Journal of Physics: Condensed Matter*, 14, 10641-10646.

Liu, Z., Lager, G.A., Hemley, R.J., Ross, N.L. (2003): Synchrotron infrared spectroscopy of OH-chondrodite and OH-clinohumite at high pressure. *American Mineralogist*, 88, 1412-1415.

Mao, H.K., Xu, J., Bell, P.M. (1986): Calibration of the ruby pressure gauge to 800 kbar under quasi-hydrostatic conditions. *Journal of Geophysical Research*, 91 (B5), 4674-4676.

McKeown, D.A., Bell, M.I., Etz, E.S. (1999): Raman spectra and vibrational analysis of the trioctahedral mica phlogopite. *American Mineralogist*, 84, 970-976.

Papike, J.J., and Zoltai, T. (1967): Ordering of tetrahedral aluminum in prehnite $Ca_2(AlFe^{+3})[Si_3AlO_{10}](OH)_2$. *American Mineralogist*, 52, 974-984.

Poli, S. & Schmidt, M.W. (1995): $H_20$ transport and release in subduction zones: Experimental constraints on basaltic and andesitic systems. *Journal of Geophysical Research*, 100 (B11), 22,299-22,314.

Scott, H.P., Liu, Z., Hemley, R.J., Williams, Q. (2007): High-pressure infrared spectra of talc and lawsonite. *American Mineralogist*, 92, 1814-1820.

Scott, H.P. & Williams, Q. (1999): An infrared spectroscopic study of lawsonite to 20 GPa. *Physics and Chemistry of Minerals*, 26, 437-445.

# Chapter 5: Conclusions

## 5.1 Concluding remarks

The purpose of the thesis was to discuss the crystal chemistry, Equation of state and structure at high pressure, and vibrational spectroscopy- far-infrared, mid-infrared, and Raman of prehnite, an important metamorphic mineral.

These studies have shown that all of the prehnite crystals studied have an average structure of *Pncm* symmetry and evidence of Al/Si ordering. The presence of violations of the *n*- and *c*-glides are evidence of ordering, with *n*-glide violations being most numerous, suggesting a predominant ordering pattern of *P2cm*. Violations of the c-glide, suggesting *P2/n* ordering scheme, is present in minimal amounts, consistent with this ordering pattern occurring on anti-phase domain walls or in small domains. The lack of large numbers of *Pncm* violations in two of the samples suggests these domains are small.

The hydrogen atom was located in the prehnite structure to be on the apex of the octahedron, attached to the OH atom whereby the vector OH-H points away from the calcium channel, with coordinates (-0.4125(7), 0.2866(6), 0) (as determined by neutrons). The hydrogen atom sits on the mirror plane, regardless of whether the space group is *Pncm* or *P2cm*, and remains fully ordered under both symmetries. The presence of the mirror also demands that the hydrogen environment OH-H…O is bifurcated, involving two oxygen atoms on an adjacent octahedron, if it participates in hydrogen bonding.

As a result of prehnite being fully ordered, with Al/Si atoms and the hydrogen, there are no contributions to configurational entropy from the structure.

The high-pressure experiments described in chapter 3 of this thesis have shown that the bulk modulus of prehnite is 109.29(18) GPa. The structure compresses almost uniformly across the interconnected polyhedra with no one bond length or angle taking up the compression. In looking at the unit cell, it compresses anisotropically. The *a*-direction is most compressible, *b* is moderately compressible, while *c* is least compressible, with *a* being twice as compressible as *c*.

Structurally, this can be accounted for by minute changes in T-O-T and O-T-O angles, resulting from the distortion of tetrahedra in a shear deformation and compression of a spiral formed by Si1 and T2 polyhedra.

The experimentally determined bulk modulus (109.29(18) GPa) is much larger than previously estimated in thermodynamic databases (83.5 GPa; Holland & Powell, 1998). Since the volume of prehnite does not change as much with pressure as previously predicted, $\Delta V$ in thermodynamic calculations changes from the previous values. When traveling from the prehnite field on a P/T diagram to a higher temperature phase, the new $\Delta V$ becomes smaller, therefore making the entropy smaller, as per the Clapeyron equation, $(\delta P/\delta T) = (\Delta S/\Delta V)$ (Spear, 1993). When travelling from the prehnite field to a phase of higher pressure, the new $\Delta V$ becomes larger, and entropy will increase as a result. As a consequence, thermodynamic calculations using database values of prehnite need to be reevaluated for new entropies and enthalpies.

The prehnite bulk modulus, when compared to other mineral structures, shows some interesting similarities and differences. Although the prehnite structure is often classified as a layer-silicate, the bulk modulus is higher than that of micas, by about a factor of two (referring to micas mentioned in Holland & Powell, 1998). Micas are most compressible along the *c*-axis, perpendicular to their mixed octahedral-tetrahedral sheets, while prehnite is stiffest along that direction. In looking at other structures with frameworks of octahedra and tetrahedra, the bulk moduli are slightly higher, in the 120 GPa range (*e.g.* titanites and vesuvianite). One set of minerals that have bulk moduli similar to that of prehnite are the pyroxenes (~105 GPa). The prehnite structure acts more as an interconnected framework of octahedra, tetrahedra, and extra-framework cation rather than a sheet silicate. This is in agreement with a diagram modified after Hofmeister *et al.* (1999), where the OH-stretching region of Raman spectra produced slopes in agreement with Phase B as opposed to slopes matching those of micas (Figure 5.1). The OH-stretching frequency and bulk modulus of prehnite are in agreement that the structure of prehnite acts like an interconnected framework rather than a layer silicate- the group of minerals in which it is classified.

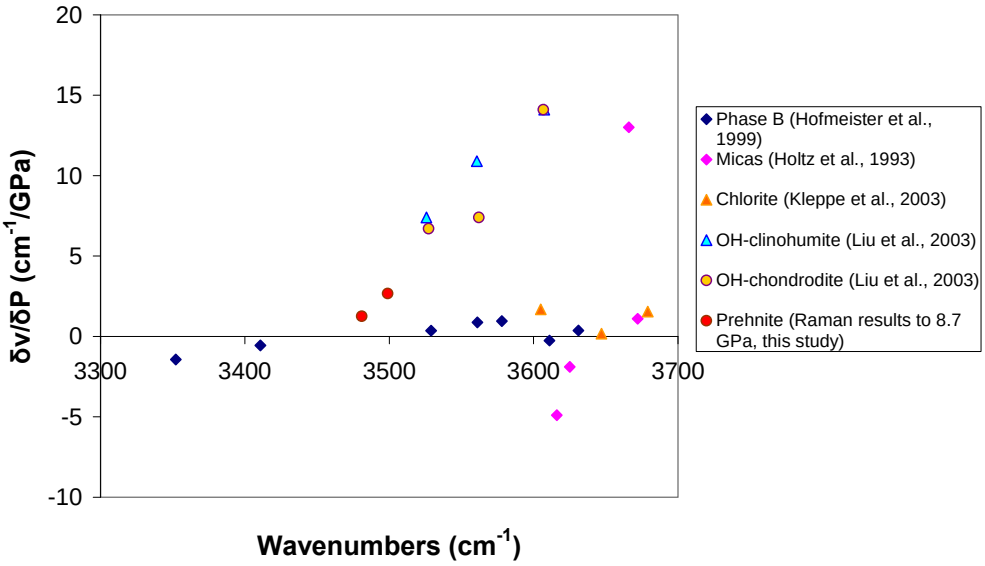


Figure 5.1: Pressure-dependence of OH vibrational modes determined from infrared and Raman spectroscopy.

At high pressures, the prehnite structure undergoes a phase transition occurring around 9 GPa. The transition is visible in X-ray data through a softening of the b-axis while the c-axis stiffens, but maintains (at least) the average structure, *Pncm*, through the transition. Spectroscopy data presented in chapter 4 are in agreement with the fact that a transition occurs around 9 GPa, as indicated by changes in the OH-stretching region, where the frequency of the peak, previously increasing with pressure prior to 9 GPa, changes direction around 9 GPa, and the frequency decreases with increasing pressure. Lower-frequency modes of the spectra also show changes in intensity and slope as a result of the transition. While the axis differences are attributed to a reduction in shear of the T2 tetrahedron, it is obvious that the hydrogen atom and its surrounding environment are affected in the transition. Although a transition at 9 GPa is not geologically relevant, knowing more about the transition provides information about structurally similar materials where knowing its compression behavior with pressure may give insight for industrial applications. To further clarify the transition and the changes in the hydrogen environment, a single-crystal neutron diffraction study would be required under hydrostatic conditions. This is not currently technically possible.

In conclusion, prehnite behaves consistently unlike layer silicates. It has a higher bulk modulus, making it fairly incompressible, and in looking at spectral slopes from the Raman results, the OH-region behaves much more like Phase B than any sort of mica. The hydrogen is not holding layers together as in a layer silicate but is a part of the interconnected polyhedra that make up the prehnite structure. The X-ray diffraction, neutron diffraction, and spectroscopic studies have allowed a more thorough study of prehnite behavior, as a function of composition and high-pressure, and the insights provided with prehnite present a more comprehensive understanding of structural behavior and hydrogen bonding in minerals.

### 5.2 References


Hofmeister, A.M., Cynn, H., Burnley, P.C., Hemley, R.J. (1999): Vibrational spectra of dense, hydrous magnesium silicates at high pressure: Importance of the hydrogen bond angle. *American Mineralogist*, 84, 454-464.

Holland, T.J.B. & Powell, R. (1998): An internally consistent thermodynamic data set for phases of petrologic interest. *Journal of Metamorphic Geology*, 16, 309-343.

Holtz, M., Solin, S.A., Pinnavaia, T.J. (1993): Effect of pressure on the Raman vibrational modes of layered aluminosilicate compounds. *Physical Review B*, 48, 13,312-313,317.

Kleppe, A.K., Jephcoat, A.P., Welch, M.D. (2003): The effect of pressure upon hydrogen bonding in chlorite: A Raman spectroscopic study of clinochlore to 26.5 GPa. *American Mineralogist*, 88, 567-573.

Liu, Z., Lager, G.A., Hemley, R.J., Ross, N.L. (2003): Synchrotron infrared spectroscopy of OH-chondrodite and OH-clinohumite at high pressure. *American Mineralogist*, 88, 1412-1415.

Spear, F.S. (1995): *Metamorphic Phase Equilibria and Pressure-Temperature-Time Paths*. 799 p. Mineralogical Society of America, Washington, D.C.

# Appendix A: Factor Group Analysis of Prehnite

**Space group: Pncm** #53 Z = 2 pt grp: mmm D2h

$Ca_2(Al,Fe)(AlSi_3O_{10})(OH)_2$

**M1A**

| # atoms | Wyckoff | site symm | Fateley |
|---|---|---|---|
| 2 | a | 2/m (C2h) | C2 (x) |

| tγ | fγ | C2h species | D2h Factor grp | Cζ | aζ = | aγ / aAu+aBu |
|---|---|---|---|---|---|---|
| 1 (Tz) | 2 | Au | Au | 1 | 1 | 1 + 0 |
| | | | B3u | 1 | 1 | 1 + 0 |
| 2 (Tx,Ty) | 4 | Bu | B1u | 1 | 2 | 2 / 0 + 1 |
| | | | B2u | 1 | 2 | 2 / 0 + 1 |

**Γ M1A =** Au + 2B1u + 2B2u + B3u

**T2A**

| # atoms | Wyckoff | site symm | Fateley |
|---|---|---|---|
| 4 | g | . 2 . (C2) | C2 (y) |

| tγ | fγ | C2 species | D2h Factor grp | Cζ | aζ = | aγ / aA+aB |
|---|---|---|---|---|---|---|
| 1 (Tz) | 4 | A | Ag | 1 | 1 | 1 + 0 |
| | | | B2g | 1 | 1 | 1 + 0 |
| | | | Au | 1 | 1 | 1 + 0 |
| | | | B2u | 1 | 1 | 1 + 0 |
| 2 (Tx,Ty) | 8 | B | B1g | 1 | 2 | 2 / 0 + 1 |
| | | | B3g | 1 | 2 | 2 / 0 + 1 |
| | | | B1u | 1 | 2 | 2 / 0 + 1 |
| | | | B3u | 1 | 2 | 2 / 0 + 1 |

**Γ T2A =** Ag + B2g + Au + B2u + 2 B1g + 2 B3g + 2 B1u + 2 B3u

**T1**

| # atoms | Wyckoff | site symm | Fateley |
|---|---|---|---|
| 4 | f | 2 . . (C2) | C2 (x) |

| tγ | fγ | C2 species | D2h Factor grp | Cζ | aζ = | aγ / aA+aB |
|---|---|---|---|---|---|---|
| 1 (Tz) | 4 | A | Ag | 1 | 1 | 1 + 0 |
| | | | B3g | 1 | 1 | 1 + 0 |
| | | | Au | 1 | 1 | 1 + 0 |
| | | | B3u | 1 | 1 | 1 + 0 |
| 2 (Tx,Ty) | 8 | B | B1g | 1 | 2 | 2 / 0 + 1 |
| | | | B2g | 1 | 2 | 2 / 0 + 1 |
| | | | B1u | 1 | 2 | 2 / 0 + 1 |
| | | | B2u | 1 | 2 | 2 / 0 + 1 |

**Γ T1 =** Ag + B3g + Au + B3u + 2 B1g + 2 B2g + 2 B1u + 2 B2u

**Ca**

| # atoms | Wyckoff | site symm | Fateley |
|---|---|---|---|
| 4 | e | 2 . . (C2) | C2 (x) |

| tγ | fγ | C2 species | D2h Factor grp | Cζ | aζ = | aγ / aA+aB |
|---|---|---|---|---|---|---|
| 1 (Tz) | 4 | A | Ag | 1 | 1 | 1 + 0 |
| | | | B3g | 1 | 1 | 1 + 0 |
| | | | Au | 1 | 1 | 1 + 0 |
| | | | B3u | 1 | 1 | 1 + 0 |
| 2 (Tx,Ty) | 8 | B | B1g | 1 | 2 | 2 / 0 + 1 |
| | | | B2g | 1 | 2 | 2 / 0 + 1 |
| | | | B1u | 1 | 2 | 2 / 0 + 1 |
| | | | B2u | 1 | 2 | 2 / 0 + 1 |

**Γ Ca =** Ag + B3g + Au + B3u + 2 B1g + 2 B2g + 2 B1u + 2 B2u

**O1**

| # atoms | Wyckoff | site symm | Fateley |
|---|---|---|---|
| 4 | e | 2 . . (C2) | C2 (x) |

**Γ O1 =** Ag + B3g + Au + B3u + 2 B1g + 2 B2g + 2 B1u + 2 B2u

**H21**

| # atoms | Wyckoff | site symm | Fateley |
|---|---|---|---|
| 4 | h | m . . (Cs) | σ (yz) |

| tγ | fγ | C2 species | D2h Factor grp | Cζ | aζ = | aγ / aA"+aA' |
|---|---|---|---|---|---|---|
| 1 (Tz) | 4 | A" | B1g | 1 | 1 | 1 + 0 |
| | | | B2g | 1 | 1 | 1 + 0 |
| | | | Au | 1 | 1 | 1 + 0 |
| | | | B3u | 1 | 1 | 1 + 0 |
| 2 (Tx,Ty) | 8 | A' | Ag | 1 | 2 | 2 / 0 + 1 |
| | | | B3g | 1 | 2 | 2 / 0 + 1 |
| | | | B1u | 1 | 2 | 2 / 0 + 1 |
| | | | B2u | 1 | 2 | 2 / 0 + 1 |

**Γ H21 =** B1g + B2g + Au + B3u + 2 Ag + 2 B3g + 2 B1u+ 2 B2u

**O2**

| # atoms | Wyckoff | site symm | Fateley |
|---|---|---|---|
| 4 | h | m . . (Cs) | σ (yz) |

**Γ O2 =** B1g + B2g + Au + B3u + 2 Ag + 2 B3g + 2 B1u+ 2 B2u

**O3**

| # atoms | Wyckoff | site symm | Fateley |
|---|---|---|---|
| 8 | i | 1 (C1) | / |

| tγ | fγ | C1 species | D2h Factor grp | Cζ | aζ = | aγ / aA |
|---|---|---|---|---|---|---|
| 3 (Tx, Ty,Tz) | 24 | A | Ag | 1 | 3 | 3 / 1 |
| | | | B1g | 1 | 3 | 3 / 1 |
| | | | B2g | 1 | 3 | 3 / 1 |
| | | | B3g | 1 | 3 | 3 / 1 |
| | | | Au | 1 | 3 | 3 / 1 |
| | | | B1u | 1 | 3 | 3 / 1 |
| | | | B2u | 1 | 3 | 3 / 1 |
| | | | B3u | 1 | 3 | 3 / 1 |

**Γ O3 =** 3 Ag + 3 B1g + 3 B2g + 3 B3g + 3 Au + 3 B1u + 3 B2u + 3 B3u

| **O4** | # atoms | Wyckoff | site symm | Fateley |
|---|---|---|---|---|
| | 8 | i | 1 (C1) | / |

**Γ O4 =** 3 Ag + 3 B1g + 3 B2g + 3 B3g + 3 Au + 3 B1u + 3 B2u + 3 B3u

Γprehnite= 14 Ag + 16 B1g + 15 B2g + 15 B3g + 13 Au + 20 B1u + 19 B2u + 14 B3u

- 3 acoustic modes (B1u, B2u, B3u)

**Γprehnite= 14 Ag (R) + 16 B1g (R)+ 15 B2g(R) + 15 B3g (R) +**
**+ 13 Au + 19 B1u (IR) + 18 B2u (IR) + 13 B3u (IR)**

total modes of vibration 123 **60 Raman, 50 IR modes**

**Space group: P2cm** Z = 2 pt grp: mm2
#28 C2v

$Ca_2(Al,Fe)(AlSi_3O_{10})(OH)_2$

**M1A**

| # atoms | Wyckoff | site symm | Fateley |
|---|---|---|---|
| 2 | c | m . . (Cs) | σ (yz) |

| tγ | fγ | Cs species | C2v Factor grp | Cζ | aζ = | aγ / aA'+aA" |
|---|---|---|---|---|---|---|
| 2 (Tx, Ty) | 4 | A' | A1 | 1 | 2 | 2 / 1 + 0 |
| | | | B2 | 1 | 2 | 2 / 1 + 0 |
| 1 (Tz) | 2 | A" | A2 | 1 | 1 | 1 / 0 + 1 |
| | | | B1 | 1 | 1 | 1 / 0 + 1 |

**Γ M1A =** 2 A1 + 2 B2 + A2 + B1

**H61**

| # atoms | Wyckoff | site symm | Fateley |
|---|---|---|---|
| 2 | c | m . . (Cs) | σ (yz) |

**Γ H61 =** 2 A1 + 2 B2 + A2 + B1

**H62**

| # atoms | Wyckoff | site symm | Fateley |
|---|---|---|---|
| 2 | c | m . . (Cs) | σ (yz) |

**Γ H62 =** 2 A1 + 2 B2 + A2 + B1

**O61**

| # atoms | Wyckoff | site symm | Fateley |
|---|---|---|---|
| 2 | c | m . . (Cs) | σ (yz) |

**Γ O61 =** 2 A1 + 2 B2 + A2 + B1

**O62**

| # atoms | Wyckoff | site symm | Fateley |
|---|---|---|---|
| 2 | c | m . . (Cs) | σ (yz) |

**Γ O62 =** 2 A1 + 2 B2 + A2 + B1

**T22**

| # atoms | Wyckoff | site symm | Fateley |
|---|---|---|---|
| 2 | b | . . 2 (C2) | / |

| tγ | fγ | C2 species | C2v Factor grp | Cζ | aζ = | aγ / aA+aB |
|---|---|---|---|---|---|---|
| 2 (Tx, Ty) | 4 | B | B1 | 1 | 2 | 2 / 1 + 0 |
| | | | B2 | 1 | 2 | 2 / 1 + 0 |
| 1 (Tz) | 2 | A | A1 | 1 | 1 | 1 / 0 + 1 |
| | | | A2 | 1 | 1 | 1 / 0 + 1 |

**Γ T22 =** 2 B1 + 2 B2 + A1 + A2

**T21**

| # atoms | Wyckoff | site symm | Fateley |
|---|---|---|---|
| 2 | a | . . 2 (C2) | / |

| tγ | fγ | C2 species | C2v Factor grp | Cζ | aζ = | aγ / aA+aB |
|---|---|---|---|---|---|---|
| 2 (Tx, Ty) | 4 | B | B1 | 1 | 2 | 2 / 1 + 0 |
| | | | B2 | 1 | 2 | 2 / 1 + 0 |
| 1 (Tz) | 2 | A | A1 | 1 | 1 | 1 / 0 + 1 |
| | | | A2 | 1 | 1 | 1 / 0 + 1 |

**Γ T21 =** 2 B1 + 2 B2 + A1 + A2

| **Ca** | # atoms | Wyckoff | site symm | Fateley |
|---|---|---|---|---|
| | 4 | d | i (C1) | / |

| tγ | fγ | C1 species | C2v Factor grp | Cζ | aζ = | aγ / aA+aB |
|---|---|---|---|---|---|---|
| 3 (Tx, Ty, Tz) | 12 | A → | A1 | 1 | 3 | 3 / 1 |
| | | | A2 | 1 | 3 | 3 / 1 |
| | | | B1 | 1 | 3 | 3 / 1 |
| | | | B2 | 1 | 3 | 3 / 1 |

**Γ Ca =** 3 A1 + 3 A2 + 3 B1 + 3 B2

| **O5** | # atoms | Wyckoff | site symm | Fateley |
|---|---|---|---|---|
| | 4 | d | i (C1) | / |

**Γ O5 =** 3 A1 + 3 A2 + 3 B1 + 3 B2

| **O71** | # atoms | Wyckoff | site symm | Fateley |
|---|---|---|---|---|
| | 4 | d | i (C1) | / |

**Γ O71 =** 3 A1 + 3 A2 + 3 B1 + 3 B2

| **O72** | # atoms | Wyckoff | site symm | Fateley |
|---|---|---|---|---|
| | 4 | d | i (C1) | / |

**Γ O72 =** 3 A1 + 3 A2 + 3 B1 + 3 B2

| **O81** | # atoms | Wyckoff | site symm | Fateley |
|---|---|---|---|---|
| | 4 | d | i (C1) | / |

**Γ O81 =** 3 A1 + 3 A2 + 3 B1 + 3 B2

| **O82** | # atoms | Wyckoff | site symm | Fateley |
|---|---|---|---|---|
| | 4 | d | i (C1) | / |

**Γ O82 =** 3 A1 + 3 A2 + 3 B1 + 3 B2

| **T1** | # atoms | Wyckoff | site symm | Fateley |
|---|---|---|---|---|
| | 4 | d | i (C1) | / |

**Γ T1 =** 3 A1 + 3 A2 + 3 B1 + 3 B2

Γprehnite= 33 A1 + 28 A2 + 30 B1 + 35 B2

- 3 acoustic modes (A1, B1, B2)

**Γprehnite= 32 A1 + 28 A2 + 29 B1 + 34 B2**

total modes of vibration= 123

all Raman active, A1, B1, B2 IR active